Morphology and Dynamics of Supported Metal Nanoparticles at the Solid-Liquid Interface – Model Systems for Sustainable Electrocatalysis

Nicolas Walter Herbert Bock

Vollständiger Abdruck der von der Fakultät für Chemie der Technischen Universität München zur Erlangung des akademischen Grades eines **Doktors der Naturwissenschaften** genehmigten Dissertation.

Vorsitzender	Prof. Dr. Ulrich Kaspar Heiz
Prüfer der Dissertation	1. Priv.-Doz. Dr. Friedrich Esch 2. Prof. Dr. Klaus Köhler

Die Dissertation wurde am 15.02.2021 an der Technischen Universität München eingereicht und durch die promotionsführende Einrichtung der Fakultät für Chemie am 27.04.2021 angenommen.

Abstract

Electrocatalysis promises to be a key technology for a sustainable global energy system. When it comes to supported nanoparticle catalysts, however, the catalyst-support interaction, especially under reaction conditions, remains poorly understood. This thesis explores at a fundamental level three aspects of catalyst control: Particle synthesis, functional support preparation, and reaction-induced sintering.

First, a novel, atomically precise metal cluster catalyst preparation in solution is presented, starting from 12-Pd^{II}-oxo-metalate precursors. Small size-controlled palladium(0) clusters are formed by reductive surface polarization on Au(111) support. The obtained particle morphology can be altered by the presence of hydrogen. Electrochemical scanning tunneling microscopy reveals one atomic layer high clusters, which show distinct swelling at the onset of the hydrogen evolution reaction.

Furthermore, this work introduces the on-surface preparation of semi-conductive carbon nitride films as novel electrocatalytic support with great potential for the stabilization and functionalization of catalytic metal particles. On Au(111) and highly ordered graphite, Triazido-*s*-heptazine is thermally polymerized under nitrogen release. The high surface interaction on Au(111) allows an extended 2D film growth with crystalline domains. Alternatively, photoactivation of the reactive azide by UV light at 110 K leads to an upright reaction intermediate that binds flat after subsequent heating. In addition to the vapor-deposition of the precursor, a liquid-based preparation is established that facilitates the applicability.

Lastly, gold nanoparticle dynamics on glassy carbon supports are studied under CO_2 reduction conditions. Previously observed catalyst aggregation reduces the catalytic activity. To improve the catalyst-support interaction, the support is modified by O_2 plasma-treatment and sulfur implantation. Both surface functionalizations are stable throughout the reductive reaction conditions. The oxidized surface shows a significantly reduced catalyst aggregation and hence an improved chemical turnover.

Zusammenfassung

Die Elektrokatalyse verspricht, eine Schlüsseltechnologie für ein nachhaltiges globales Energiesystem zu werden. Bei deponierten Nanopartikeln ist allerdings die Wechselwirkung zwischen Katalysator und Substrat, insbesondere unter Reaktionsbedingungen, nur unzureichend verstanden. Diese Arbeit untersucht drei fundamentale Aspekte von Katalysatoren: Herstellung von Metallkatalysatoren, Entwicklung funktionaler Trägermaterialien und Untersuchung reaktionsinduzierter Partikel-Reifung.

Eine neuartige Deposition von Metallclustern in Lösung aus 12-Pd^{II}-oxo-metallate Molekülen wird vorgestellt. Durch reduktive Oberflächenpolarisation bilden sich kleine Palladium(0)-Cluster auf einer Au(111) Oberfläche. Die erhaltene Partikelmorphologie kann durch die Anwesenheit von Wasserstoff während der Deposition verändert werden. Die elektrochemische Rastertunnelmikroskopie zeigt einlagige Cluster, die zu Beginn der Wasserstoffentwicklungsreaktion ein deutliches Schwellverhalten zeigen.

Darüber hinaus wird in dieser Arbeit eine neuartige geträgerte Präparation von halbleitenden Kohlenstoffnitridfilmen vorgestellt. Diese zeigen großes Potential sowohl hinsichtlich der Stabilisierung als auch der Funktionalisierung von Metallkatalysatoren. Auf Au(111) und hochgeordnetem Graphit wird triazido-*s*-heptazin unter Stickstofffreisetzung thermisch polymerisiert. Die hohe Oberflächenwechselwirkung auf Au(111) ermöglicht ein ausgedehntes 2D-Filmwachstum mit kristallinen Domänen. Eine alternative Aktivierung der reaktiven Azidgruppe mit UV-Licht bei 110 K zeigt ein aufrecht stehendes Reaktionsintermediat, das sich nach anschließendem Aufheizen komplanar zur Oberfläche anordnet. Neben dem Aufdampfen des Ausgangsstoffes ist eine Präparation aus Benzol möglich, die die Anwendbarkeit erleichtert.

Schließlich wird die Dynamik von Gold-Nanopartikeln auf Glaskohlenstoff unter CO_2-Reduktionsbedingungen untersucht. Die zuvor beobachtete Katalysatoraggregation reduziert die katalytische Aktivität. Um die Interaktion zwischen Katalysator und Substrat zu verbessern, wird der Glaskohlenstoff mit O_2-Plasmabehandlung und Schwefelimplantation modifiziert. Beide Oberflächenfunktionalisierungen sind unter den Bedingungen der reduktiven Reaktion stabil. Die oxidierte Oberfläche zeigt eine deutlich geringere Katalysatoraggregation und damit einen verbesserten chemischen Umsatz.

Contents

1. Introduction

1.1. Motivation

Anthropogenous impacts on the earth's ecosystem lead to climate change and mass extinction.[1,2] The exploitation of fossil fuel – both for the production of energy and chemical feedstock – causes the emission of greenhouse gases and has been identified as the main climate change accelerator, besides deforestation and intensive land cultivation. Concerning energy production, current efforts focus on switching to renewable electricity sources. However, one must be aware that the electricity sector accounts only for approximately 12% of the global energy demand (2.1 out of 17.6 Terawatt in 2010).[3] While still 66.3% of electrical energy are produced from fossil fuels,[4] the possible expansion of sustainable energy production by additional wind turbines, photovoltaic collectors etc. is well established from a scientific and technological point of view.

The major climate-changing impact is still related to the chemical feedstock production. 90% (150 million tons) of all greenhouse gas emissions in Europe can be traced back to the production of 26 chemical compounds.[5] The majority of them are used for fertilizers, polymers, and basic organic or inorganic substances, which are further processed for consumer products like personal care items, food preservatives, and furnishings.[6] Even in regions with low to moderate population and wealth growth such as Europe, the chemical production of these compounds is still growing and expected to reach greenhouse gas emissions of 200 million tons by 2050, if no retrofits take place.[5]

In order to replace the majority of fuel-based production processes of chemical feedstock, new technological approaches are needed. While photocatalysis promises a direct chemical conversion by sunlight, its efficiency strongly depends on the geographic location and seasonaly heavily varying day-night cycles. While this holds also for the renewable electricity production, electric power can be stored and transported. Although the conversion of chemicals by renewable electricity might indicate a reduced efficiency at first glance, due the additional energy transformation, electrocatalytic processes promises high faradaic efficiency and chemical selectivity, needed to compete with fossil fuel-based chemicals. In this way, the chemical feedstock production could even be used as a long-time energy buffer, in addition to established short-term storage systems, such as batteries and pumped-storage power plants. Electrocatalysts

are well-suited for such a purpose, as they require little ramp-up times compared to thermocatalytic processes, that need a time-consuming warm-up phase. In order to substitute energy-intensive high-pressure or thermochemical processes, which could as well be driven by renewable electric energy, although at higher energy consumption, chemical transformations induced directly by electric current are the most promising approach.

1.1.1. Electrosynthesis: New Approaches to Chemical Feedstock

Electrosynthesis allows well-established renewable energy sources, such as wind, hydro, and solar energy to directly power chemical transformations. Replacing thermocatalytic processes itself already results in reduced CO_2 emissions, but this impact could dramatically be improved if also the starting chemical materials would be produced in a sustainable way. This could be achieved by adapting a circular economy similar to the earth's hydrological cycle (see Figure 1.1). Atmospherically occurring N_2, CO_2, and H_2O provide a universal feedstock and could be upconverted to valuable chemical products by electrocatalysts, that use the electrical power to promote the chemical reaction. The resulting fossil fuel-free chemical portfolio is manifold and allows to derive chemical compounds of global importance, like hydrogen (current production 50 Mt/year), hydrogen peroxide (2.2 Mt/year), ethylene (115 Mt/year), propylene (73 Mt/year), methanol (40 Mt/year), and ammonia (175 Mt/year).[3]

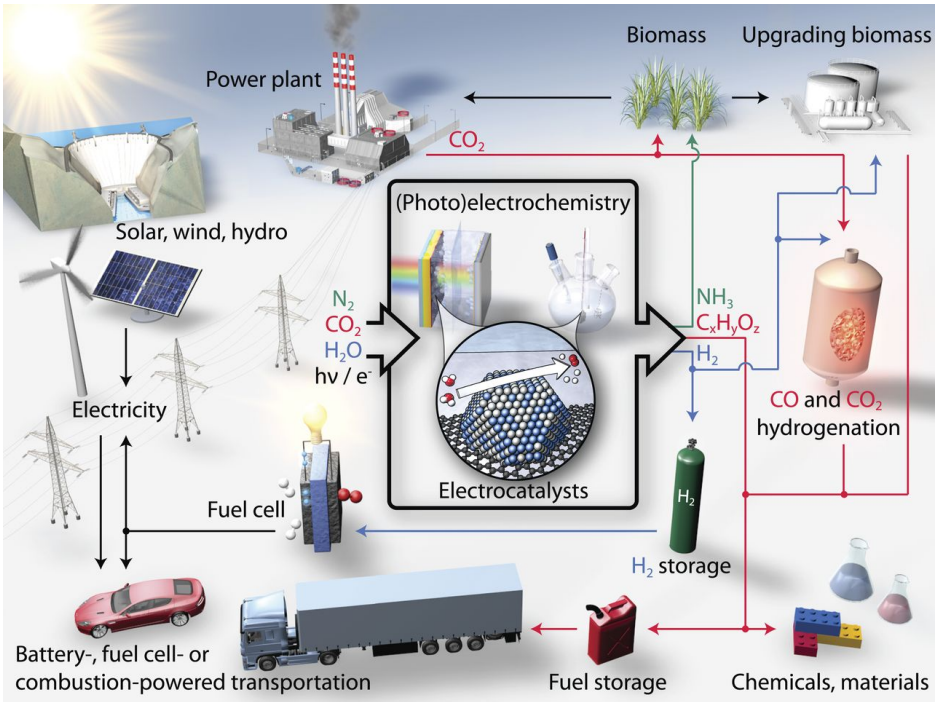

Figure 1.1. (Photo)electrocatalysis could play one major role in transforming the current energy sources to non-petrochemical. From Z. W. Seh et al., *Science* **2017**, *355*, 146. Reprinted with permission from AAAS.

The electrochemical reduction of H_2O results in the formation of H_2 (blue arrows in Figure 1.1), which is an important reducing agent and an excellent energy carrier. While the current private transportation sector mainly focuses on battery-driven vehicles, the energy demand for commercial transportation is better matched by high energy density chemical fuels. A hydrogen-based energy economy has been proposed already in 1930s.[7] The main process to produce hydrogen up to now has been the water-gas shift reaction by conversion of natural gas or gasified coal. These CO_2-intensive processes can and have to be replaced today for technological as well as economical reasons.

The price of proton-exchange membranes and alkaline electrolyzers has decreased in the last decades by approx. 3 – 5% per annum. As a result, the break-even price for hydrogen produced by wind energy is currently 3.23 Euro/kg in Germany and is projected to further decline (see Figure 1.2).

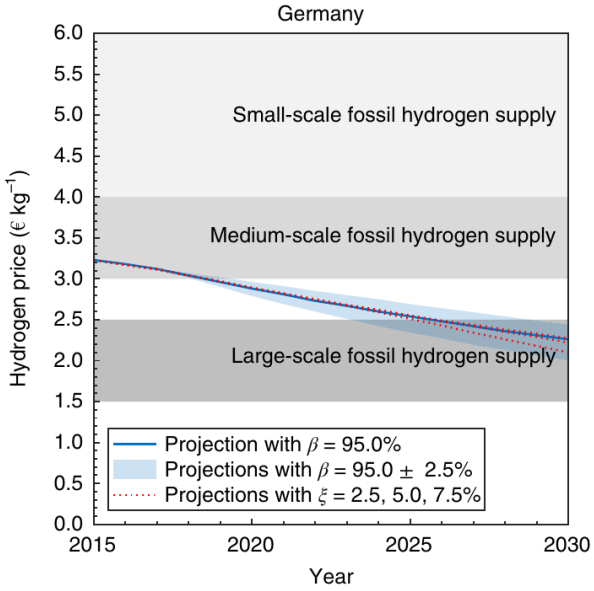

Figure 1.2. Projection of wind energy produced hydrogen break-even price of up to the year 2030 in Germany in comparison with small-, medium-, and large-scale fossil hydrogen supply. The price of wind energy produced hydrogen is expected to be cost-competitive with large-scale fossil hydrogen between 2023 and 2029. From G. Glenk, S. Reichelstein, *Nature Energy* **2019**, *4*, 216–222. Reprinted with permission from Springer Nature.

Currently, the price for such renewable hydrogen is competitive with that from small- and medium-scale fossil production and is expected to equal the price from large-scale fossil production within the next decade. This includes an additional annual cost reduction of 4% for wind turbines.[8] Theoretically, the electrochemical hy-

drogen generation could be driven at elevated temperatures to reduce the required electrical bias, but that is only worthwhile if thermal energy is freely available.[7] Therefore, it could be advantageous to produce hydrogen at geothermic sites or in combination with exothermic processes, which would result in earlier profitability.

1.1.2. Theoretical and Experimental Approaches in Electrocatalysis

The crucial compound for electrosynthesis is the electrocatalyst at play. The hydrogen evolution reaction (HER), for example, is highly facilitated by the use of noble metal catalysts which are expensive and hardly accessible in an ecofriendly way. It is therefore reasonable to replace or at least reduce the amount of noble metal used, while still maintaining the same chemical turnover. This requires dedicated catalyst development strategies, exemplified in Figure 1.3 that shows two possible approaches.

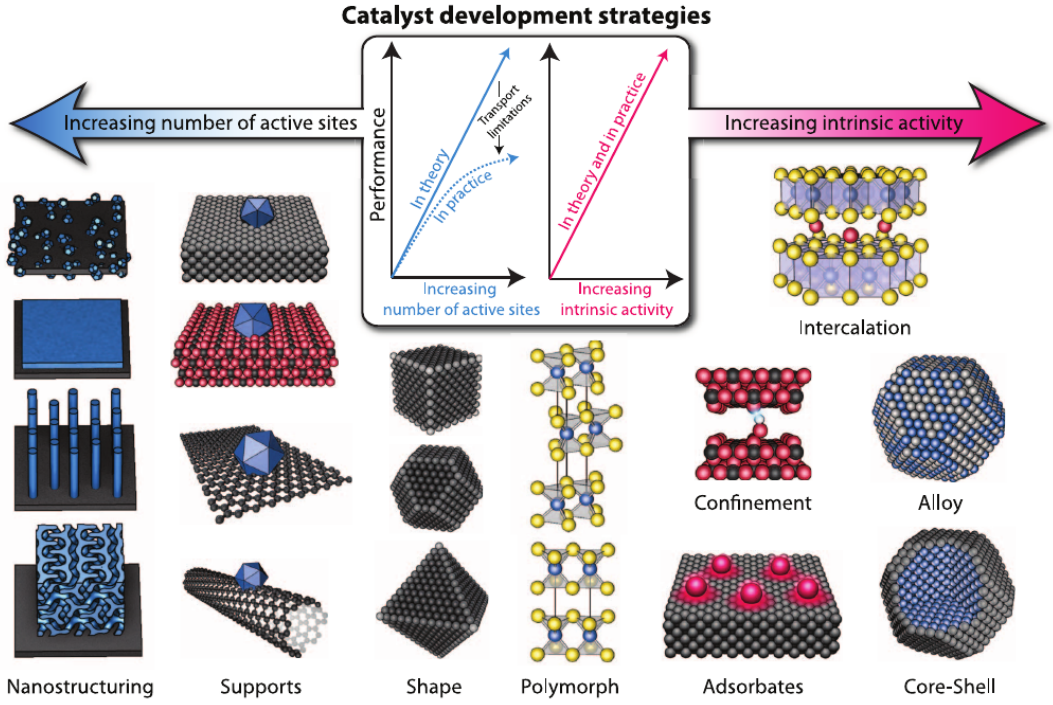

Figure 1.3. Strategies to improve catalysts: Either by increasing the intrinsic activity by changing the chemical state of the catalyst, or increasing the number of active sites by modifying steric properties. From Z. W. Seh et al., *Science* **2017**, *355*, 146. Reprinted with permission from AAAS.

Changing the number of active sites per mass loading always comes with a geometrical change of the catalyst and/or support structure. A high surface-to-volume

ratio is generally beneficial, but is constrained by transport limitations of reagent and products to and from the active site, similar to heterogeneous catalysis in general. Additionally, the electrical contact of the active site to the external power source is crucial in electrocatalysis. Ohmic voltage drops in the support can drastically reduce the chemical turnover at a given potential.[9]

Alternatively, the intrinsic activity of each site can be changed, by tuning the chemical state of the catalyst and thus the binding of reaction intermediates. For example, the hydrogen evolution reaction is largely determined by the free energy of hydrogen adsorption.[10] On the catalyst surface M this adsorption requires the Volmer step ($H^+ + e^- + M \longrightarrow HM$), which is facilitated if hydrogen can bind strongly to the catalyst. A weak binding, on the other hand, is beneficial during the hydrogen desorption, by either the Heyrovsky ($HM + H^+ + e^- \longrightarrow H_2 + M$) or the Tafel step ($2HM \longrightarrow H_2 + 2M$). The catalyst activity can therefore be characterized by a key descriptor, the hydrogen adsorption free energy. Figure 1.4 shows the hydrogen binding energies of different metal catalysts with their HER activity. This so called vulcano plot suggests maximal activity at $\Delta G_H \approx 0$.

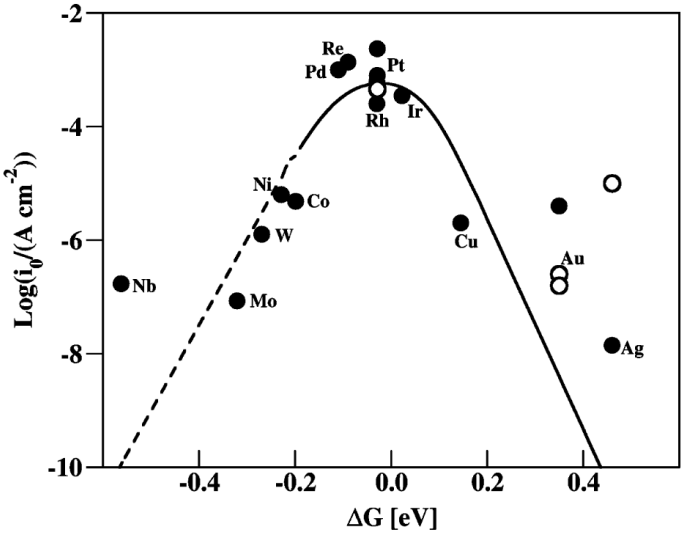

Figure 1.4. Estimated hydrogen adsorption free energy of different metals against their experimental HER performance at a given potential on basis of density theory function calculations. The highest activity was found for $\Delta G_H \approx 0$. Reprinted with permission from E. Skúlason et al., *The Journal of Physical Chemistry C* **2010**, *114*, 18182–18197. Copyright 2020 American Chemical Society.

1.1.3. Cluster Catalysis

A common approach to improve the amount of active sites while still using the same catalyst loading is the systematic reduction of particle size, down to the nanometer scale. While larger nanoparticles still show properties that can be scaled down from bulk size properties, electronic and geometrical shell closures come into play, once sizes of hundred atoms or less are reached. This is the non-scalable size regime of clusters, that show strongly size-dependent properties, unlike those of the bulk material. This can imply drastic variations of catalytic activity by the addition of just a single atom.[11] For example, Imaoka et al. [12] were able to show that Pt_{12} shows a two-fold higher oxygen reduction reaction (ORR) activity compared to Pt_{13}. The preparation of atomically well-defined supported particles is challenging and the cluster preparation, selection, and deposition protocols have been established in various ambients. Very versatile vacuum cluster generation techniques in use are based on laser-vaporization[13], magnetron sputter sources[14], collisional cooling in noble gases and a possible supersonic expansion. The subsequent mass selection is achieved by quadrupole mass spectrometry and the clusters are then softly landed on the support in ultra-high vacuum conditions. Experimental studies on clusters in ambient conditions are then achieved by a transfer from vacuum to ambient environments.[15,16] Alternatively, clusters can be formed directly in liquids. Common approaches known from nanoparticle synthesis, like ligand stabilization[17,18] or template synthesis[12,19] were able to obtain reduced particle sizes to reach atomic numbers smaller than 100. However, the ligand-assisted preparation allows only clusters with atomic numbers that have an inherent stability (e. g. Pt_{13}, Pt_{55}). Although with a dendrimer template also other atomic numbers are possible,[12] a systematic variation of cluster sizes remains challenging. A detailed review of colloidal cluster preparation is given in [18].

1.1.4. Study of Catalyst Morphology – Electrochemical Scanning Tunnel Microscope

Current challenges in the research on electrocatalysts are manifold. Besides the actual performance, the morphology and stability of catalysts under reaction conditions are very important. Nanoparticles with a large surface area are intrinsically metastable. In order to study fundamental processes, like aggregation or dissolution at the nanoscale, microscopy techniques are needed. As electrocatalysts are always electronically conductive, topography measurements can be performed by the scanning tunneling microscope (STM). On the basis of the pioneering work of Young, Ward,

and Scire [20] on a spatially resolved field gun, Binnig et al. [21] invented the STM. It was shown that tunneling electrons allow for STM imaging also at the solid-liquid interface.[22–24] Sonnenfeld and Schardt [25] were the first to add a salt to the liquid and to control the potential of the tip and surface with respect to an external reference electrode. This article was also the first pioneering *in-situ* study to show the successful deposition of silver metal in an electrochemical scanning tunneling microscope (ECSTM). In the following years, STM was mainly applied under vacuum conditions by the surface science community and atomically resolved electrochemistry remained rare. This changed with the pioneering work of Möller et al. [26], Baldauf and Kolb [27], and Tansel and Magnussen [28] showed the potential of combining surface science techniques in vacuum with the new arising field of surface electrochemistry. This allowed for a better understanding of surface morphology changes directly under catalytic conditions.

Besides the structural information, recent ECSTM experiments also provide insights into the catalytic performance. Pandelov and Stimming [29] used the STM tip as a microsensor, which can be placed above single catalytically active particles, thereby oxidizing or reducing to the tip diffusing products. Within the diffusion limitations, this can give insights in the relative catalytic performance of specific surface features. Another approach to study catalytic activities was introduced by Pfisterer et al. [30]. They were able to correlate a higher noise in the STM signal with active sites. Here the noise indicates reactive surface areas in the HER and ORR. This phenomenon is tentatively attributed to the adsorption and desorption of reaction species during the ongoing reaction. The reactivity differences of step edges and terraces corresponded well with integral investigations of stepped single crystal surfaces.[31]

1.2. Scope of the Work

In order to tackle the challenges at hand, this work's main goal was to establish a new model catalyst system to investigate fundamental cluster morphology dynamics during electrocatalysis with local microscopy and integral electrochemical techniques. Such a model system would enable the further study of catalyst dynamics by means of fast STM,[32] which allows imaging at video-rate scan frequencies even under reaction conditions and paving the way for a deeper understanding of the catalyst-support interaction, particle stability, and the catalytic processes at the atomic level. However, the preparation of well-defined clusters from solution remains challenging and a novel

preparation approach is therefore explored within this work. Besides the general requirement for an electrocatalyst to be conductive and long-term stable, the surface of the model system should be atomically flat for ECSTM imaging. As the catalyst-support interaction is mainly governed by morphology and the support's chemical binding sites, different surfaces and modifications were explored. It is the idea of this approach that the comprehensive mechanistic understanding of the involved reactions at the solid-liquid interface can be applied to the field of energy conversion and transferred to develop technical applications with high chemical turnover, selectivity, and durability.

1.3. Thesis Outline

The used experimental setups, materials, and the data treatment are described in section 2. The focus is here on describing improved and self-built setups and routines, while commercial and well-established systems are more briefly specified.

As all projects within this thesis have been performed in a collaborative manner, each result section is prefaced with a list of contributors and their roles in the project. Section 3 includes the submitted peer-reviewed journal publication about the novel solution-based cluster preparation technique, which enables the preparation of small palladium metal clusters. While this publication focuses on the deposition on gold surfaces, the use of electrochemically more stable carbon nitride supports might be advantageous for the use as catalyst support. A bottom-up synthesis of a 2D carbon nitride film is presented in Section 4. Lastly, in section 5 the dynamics of nanoparticles on pristine and modified carbon supports is investigated. While most of the experimental work for this thesis was performed at the Chair of Physical Chemistry at the Technical University of Munich (TUM), the experiments of section 5 were performed during a research stay at Stanford University with Christopher Hahn, Jaime Aviles Acosta, and Thomas Jaramillo.

2. Methodology and Experimental Setups

2.1. Integral Electrochemical Methods

The basis of most electrochemical experiments is a three electrode setup, which has been described extensively elsewhere.[33,34] The main components are a working (WE), counter (CE), and reference electrode (RE), which are all connected to a potentiostat. At a certain applied voltage between WE and CE, electrochemical processes take place at the WE, while the concomitant charge transfer is neutralized by an external current flow towards the CE, that is measured by the potentiostat. The RE allows for the correct measurement of the WE potential as it is connected via a high ohmic resistance to the potentiostat and experiences hence a minimal current flow. The potentiostat regulates the WE potential to a given cell voltage setpoint. The resulting cell current and cell voltage give insights into the electrochemical behavior of the studied material at the working electrode.

In the work at hand, three different types of RE were used:

1. Reversible hydrogen electrode (RHE): The pH-independent RHE consists of a platinum wire which is introduced into a glass reservoir filled with the electrolyte and a hydrogen bubble. The latter can be created by applying a negative potential to the platinum wire to evolve hydrogen. The RHE is prepared freshly prior to each experiment. The open circuit potential (OCP) does not depend from the RHE.

2. Platinum pseudo reference electrode: The OCP of platinum pseudo reference electrodes depends on the species in the respective electrolyte. As adsorption and reaction processes can occur also on platinum at certain potentials, the reference potential is not strictly linear. It is only used for extremely compact experimental setups.

3. Silver / silver chloride electrode: A double reservoir glass ceramic separated SI Analytics *ScienceLine* electrode is used as Ag/AgCl electrode. Similar to the RHE, the OCP does not depend on the Ag/AgCl electrode.

The ideal material for the CE is very conductive and (electro)chemically inert. For this work, platinum wire was used as a counter electrode as it fulfills the desired specifications and is easy to clean. Although platinum can dissolve and influence the electrochemistry on the working electrode, it remains a wide-spread CE material in moderate potential ranges. Ideally, a membrane like a glass frit should be used to separate CE- and WE-reservoir.[35]

2.1.1. Cyclic Voltammetry

Cyclic voltammetry (CV) is the electrochemical technique applied in a three electrode setup that investigates the interplay between potential-induced faradaic reactions, capacitive currents, and ion migration. Figure 2.1 exemplarily shows a typical sequence of a CV measurement, where the voltage is steadily increased, starting from reducing conditions. The applied potential is swept linearly in a sawtooth time dependence (I) and the current response is recorded (H). At a given electrochemical potential, a molecular redox-active species in the electrolyte will undergo a reaction at the electrode surface. This electron transfer causes an increase in current (point B). The redox species depletes near the electrode surface until the molecule concentration of the oxidized form outweighs the reduced form (point C) – see corresponding concentration profiles. The current response now decreases due to the mass transport limitation. The same process is reversed after the upper vertex potential (switching from so-called anodic to cathodic sweep), until the potential reaches its starting point again. Points A and G can show different current values as a result of a concentration hysteresis. In addition to the faradaic contribution, also capacitive currents occur due to restructuring of the electrochemical double layer.

CV can help in understanding electrochemical phenomena on the WE surface related to both, adsorption and reconstruction processes as well as redox reactions of dissolved species. Faradaic peaks in the CV correspond to a chemical redox reaction $\mathrm{Ox} + \mathrm{ne}^- \rightleftharpoons \mathrm{Red}$, which are described by the Faraday equation (2.1).[33]

$$N = \frac{Q}{n \cdot F} \tag{2.1}$$

In (2.1), N is the amount of transformed chemical species, Q is the charge, and F is the Faraday constant.

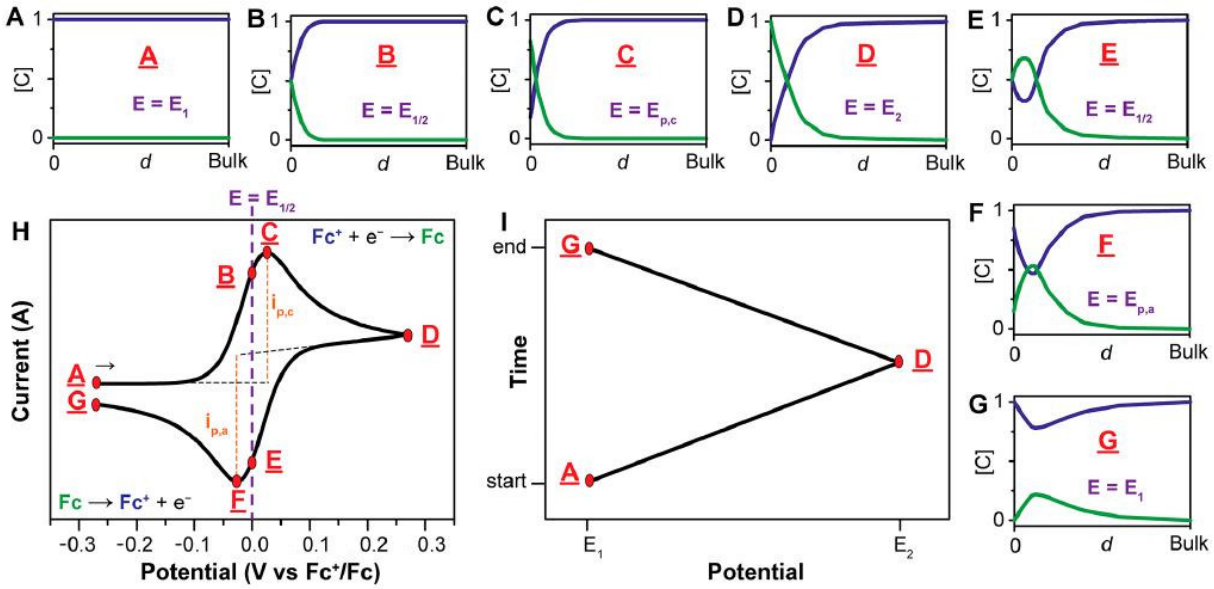

Figure 2.1. **(A – G)** Concentration profiles of the ■ reduced and ■ the oxidized species versus the distance into the bulk electrolyte (d=0: WE surface). The electrochemical system is excited with an applied voltage profile **(I)**. The resulting current response is plotted against the measured potential in **(H)**. Reprinted modified with permission from N. Elgrishi et al., *Journal of Chemical Education* **2018**, *95*, 197–206 under *ACS AuthorChoice* license.

The electrochemical redox potential is influenced by thermodynamics, as described by the Nernst equation (2.2).[33]

$$E = E^0 + \frac{R \cdot T}{n \cdot F} \cdot \ln \frac{c_{ox}}{c_{red}} \tag{2.2}$$

Here, E^0 is the standard redox potential, R the ideal gas constant, T the temperature, n the number of transferred electrons, F the Faraday constant c_{ox}, and c_{red} the concentration of molecular species in oxidized and reduced form.

Additionally, also kinetics influence the peak potential. A kinetic hindering of the electron transfer leads to an overpotential η, that needs to be applied in excess to drive the reaction at a given rate.[33]

$$\eta = E - E_{eq} \tag{2.3}$$

Here, E is the actual applied potential while E_{eq} is the potential observed experimentally at infinitesimal rates. The current response at a given rate is described by the Randles-Sevcik equation. For more details see [37].

Also the peak shape can give mechanistic insights. An asymmetrical peak with a very high slope in the onset can for example indicate a reaction of a previously adsorbed species[38] or a reaction at step edges of the surface.[29] The applicability of

CV is not only limited to faradaic phenomena; CV can also capture capacitive restructuring of the double layer and surface changes, like the lifting of the Au(111) reconstruction.[39]

2.1.2. Impedance Spectroscopy

The measurement of the impedance of an electrochemical system can offer a better understanding of the chemical composition of bulk and double layer, of adsorption processes, and of the diffusion of involved ionic species at a given WE potential.

Principles and Functionality

Impedance spectroscopy investigates the different time scales of charge carrier dynamics, namely that of electrons and ions. These contain information on conductivity and diffusion, but also structural information on the studied system. The perturbation of an electrochemical system by an applied sinusoidal voltage $\widehat{U}$ results in a current response $\widehat{I}$, which can be expressed as:

$$\widehat{U} = U_0 \cdot \mathrm{e}^{i(\omega \cdot t + \phi_U)} \tag{2.4}$$

$$\widehat{I} = I_0 \cdot \mathrm{e}^{i(\omega \cdot t + \phi_I)} \tag{2.5}$$

Here, U_0 and I_0 are the respective amplitudes, ω the angular frequency, and t the time. The phase shift ϕ results from the current response time, $\phi = \phi_I - \phi_U$.

The impedance $\widehat{Z}$ can thus be derived using the Ohm's law:

$$\widehat{Z} = \frac{\widehat{U}}{\widehat{I}} \tag{2.6}$$

By applying the Euler equation $\mathrm{e}^{ix} = \cos(x) + i\sin(x)$, one can represent the impedance with separated imaginary and real part:[40]

$$\widehat{Z} = Z_0 \cos(\phi) - iZ_0 \sin(\phi) = Z_{\mathrm{real}} - iZ_{\mathrm{img}} \tag{2.7}$$

A very practical way to visualize impedance spectroscopy is the Nyquist plot that displays the imaginary part versus the real part of the impedance, while each point represents a different applied frequency. The conductivity contributions of electrons and ions vary in their time-scale, hence electronic properties are found at high frequencies and ionic at low frequencies. In order to simulate and fit impedance spectroscopy data, electronic equivalent circuits are used to describe the electrochemical response. Fig-

ure 2.2a shows e. g. the ideal behavior of a Randles circuit element which consists of a solution resistance $-R_S-$, an electrolyte double layer $-RQ-$, and a Warburg element $-W-$. The latter describes the semi-infinite linear diffusion in front of the working electrode. The Warburg impedance is described by the following equation:[41]

$$Z_W = \frac{R \cdot T}{n^2 \cdot F^2 \cdot A \cdot \sqrt{2D}} \cdot \left(\frac{1}{c_o} + \frac{1}{c_r} \right) \cdot \omega^{-\frac{1}{2}} \cdot (1 - i) \tag{2.8}$$

where R is the ideal gas constant, T the temperature, n the transferred electrons, F the Faraday constant, A the surface area, D the diffusion coefficient, and c_o the concentration of oxidized and c_r of reduced species.

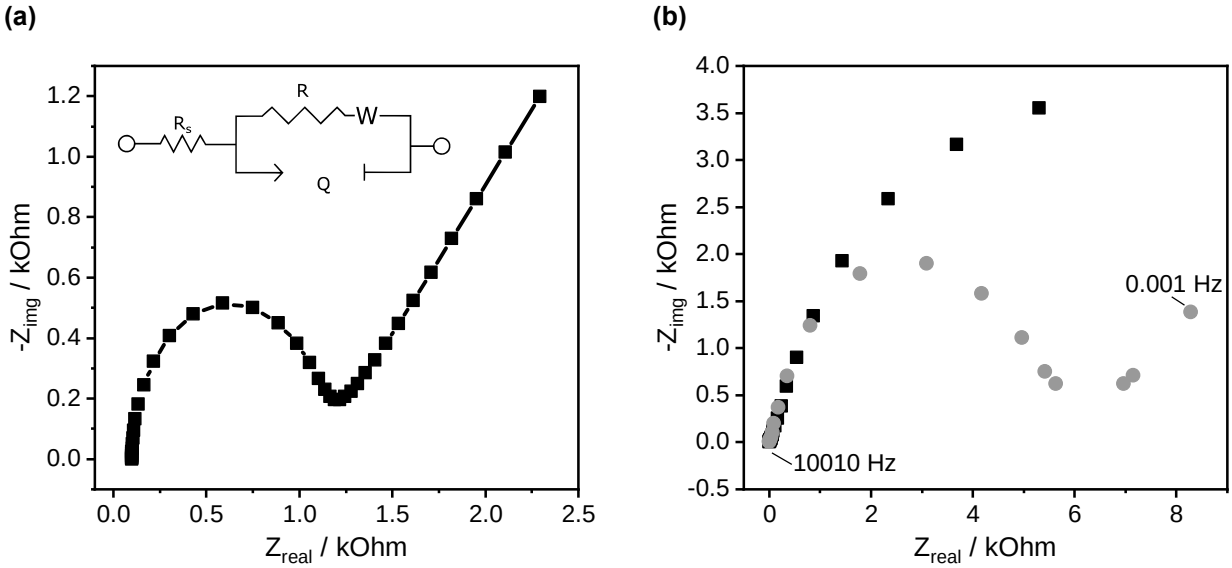

Figure 2.2. **(a)** Simulation of a Randles element (see inset for circuit diagram) shown in a Nyquist plot. The used parameters match the dummy cell described in Section 2.2.4. **(b)** Influence of the gas saturation (■ Ar; ■ O_2) of the electrolyte (1 M $HClO_4$) during impedance spectroscopy of Au(111). At low frequencies a significant difference is observed, suggesting a different ionic double layer composition.

2.1.3. Experimental Setup

The Rotating Disk Electrode (RDE) is commonly used to study electrocatalysis. This technique is also based on a three electrode setup (see chapter 2.1), but the working electrode is mounted on a rotating shaft. This rotation of the WE allows for the control of the mass transport from the bulk solution to the WE surface. A variation of the rotation speed allows hence to disentangle the kinetic behavior of a catalyst from mass transport limitations.

Figure 2.3a shows the RDE setup. The glass cell, applicable for acidic media as used in this thesis, allows for a temperature variation by a heating fluid passing through the double-wall construction. The *Teflon* cap prevents contamination from entering the cell and reduces gas exchange with the atmosphere. It has a lateral hole for the gas inlet to ensure a gas purged solution and two ground glass joints for adding RE and CE components. The gas bubbler ends with a frit to ensure the creation of small gas bubbles. This trick drastically reduces the amount of time needed to degas the solution. For the work at hand, usually ten minutes of gas purging were applied before the experiment. A Luggin capillary with 90° angle geometry was employed to connect the reference electrode. The counter electrode, protected by a frit, was attached to the opposite joint.

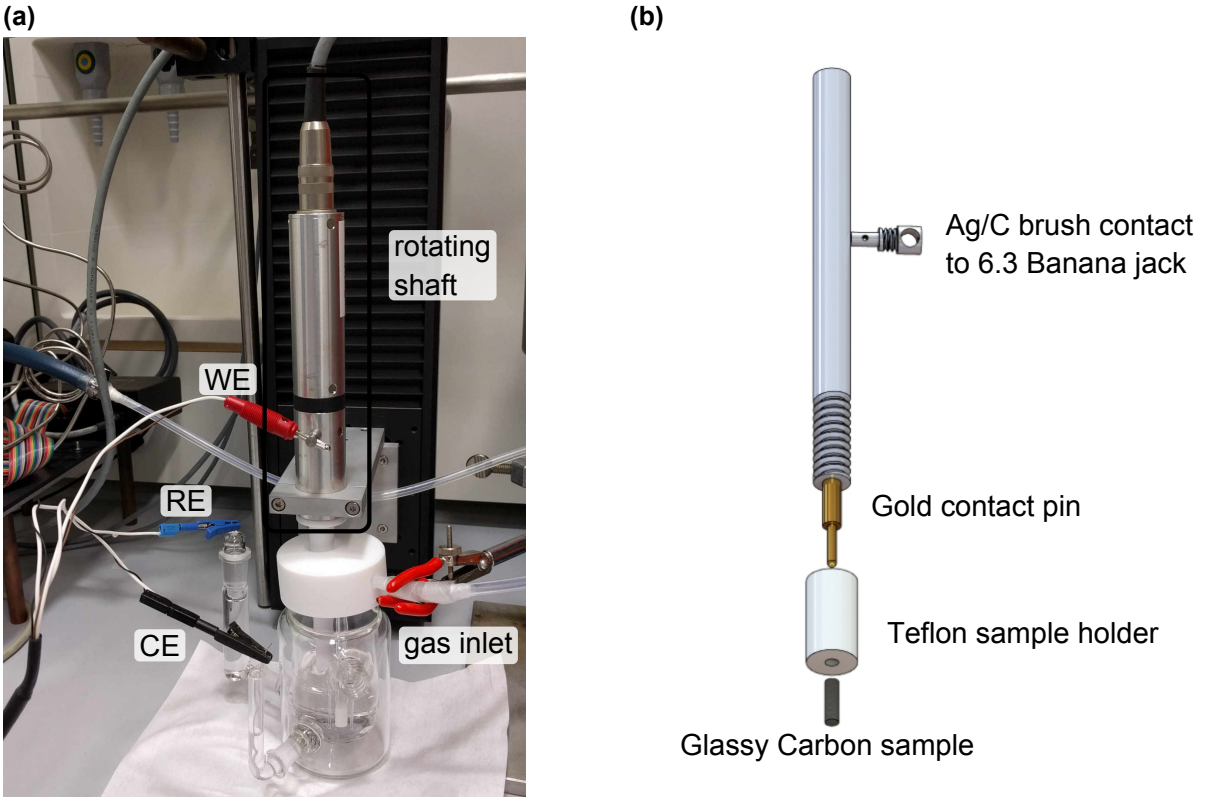

Figure 2.3. **(a)** Rotating disc electrode setup with electrochemical cell. The three electric connections lead to the *EC-4* potentiostat (not in the image). The gas inlet allows the cell to be purged via an automated gas switch. The RDE itself is mounted on a linear positioning system. **(b)** Exploded view of the inner parts of the RDE: The rotating shaft enables a sample mounting via threaded connection. The electrical connection is ensured by a spring-suspended gold-coated contact pin.

The *EC-4* potentiostat from Nordic Electrochemistry (not shown in Figure 2.3a) is connected via 2 mm (RE, CE) and 6.3 mm (WE) Banana connections. A four-wire technique to correct for ohmic drops in the cable is used for the counter and working electrodes.

The RDE itself was designed by Wiberg [42]. It is now mounted on a motor-driven linear positioning system (see appendix A.1 for hardware details). The rotation speed can be controlled with the Nordic Electrochemistry *EC-4 DAQ* software, which outputs a DC voltage to the motor control ESCON *36/2 DC*. Figure 2.3b shows the inner parts of the RDE. The crucial connection between the rotating shaft and the potentiostat is implemented by a carbon-silver brush contact pressed against the stainless steel rod. The critical electrical contact between the rotation shaft and the sample is realized by electrical tester pins Feinmetall *F100* with 100 cN spring force. Three different types of sample holders were used (see Figure 2.4): Single crystals have to be mounted with as little force applied as possible, therefore a clamp design (a) is used. More robust cylindrical samples like amorphous glassy carbon are simply pressed into a cylindrical *Teflon* holder (b). Flat samples like graphite can be mounted with a drawer-type sample holder (c). Here, the sample is pressed towards the electrolyte-exposed window by the gold contact pin. A groove is milled into the edge of the sample holder to avoid that gas bubbles are trapped at the interface. Since this slot breaks the point symmetry of the design, it will most likely interfere with the laminar flow parallel to the surface during rotation. For that reason, this sample holder should not be used for kinetic studies, where exact mass transport is crucial.

Design of Impedance Spectroscopy Cell

Reliable impedance spectroscopy measurements require a coplanar arrangement of the WE and CE with the RE placed in between. The area of the CE must exceed that of the WE to avoid any current limitation. Figure 2.5 shows the home-built impedance cell used in this work. The WE is lowered from above and touches the electrolyte level that is adjusted in height to obtain a symmetric setup with respect to the external RE (RHE or Ag/AgCl electrode). Argon gas flows continuously over the electrolyte surface to maintain inert gas saturation in the solution, as this has a huge influence on the measurement (see Figure 2.2b). Typically, impedance measurements take several hours and hence the evaporation of solvent is considerable. Therefore, the cell volume of 50 mL is relatively large.

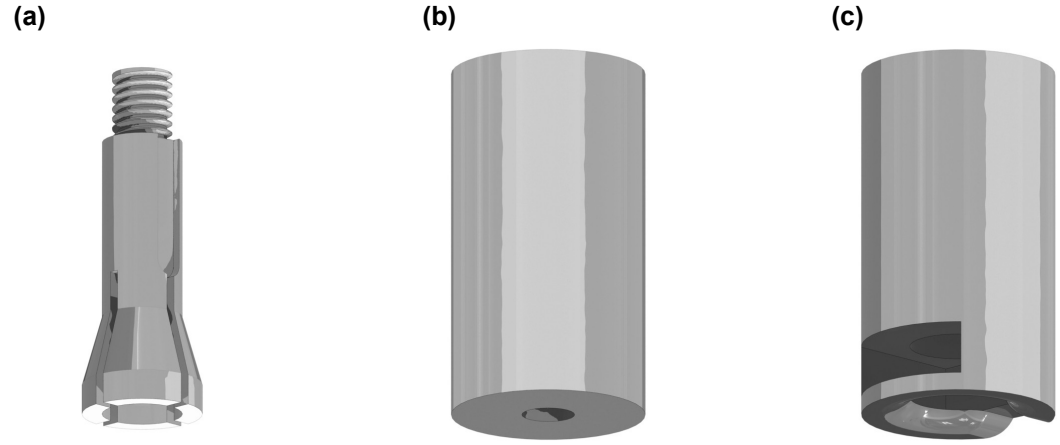

Figure 2.4. Sample holder designs for the RDE setup: **(a)** Clamp-like holder for sensitive single crystals. **(b)** Cylindrical samples like glassy carbon, which are pressed into the *Teflon* housing. **(c)** Drawer-like sample holder for flat samples like HOPG, which are inserted sideways and pressed down by the gold contact pin.

2.2. Electrochemical Scanning Tunneling Microscopy

The electrochemical scanning tunneling microscope (ECSTM) combines the imaging possibilities of a scanning tunneling microscope (STM) with the three electrode integral electrochemical setup. This enables not only the topography measurement under electrochemical potential control, but can as well be used for local reactivity measurements.

2.2.1. Principles of Scanning Tunneling Microscopy

The STM is a scanning probe method (SPM), where an extended surface is imaged by means of a sharp tip that is vertically approached to the surface and laterally scanned. STM exploits the tunnel effect through potential barriers of limited height and lateral extension in order to map the local electron density as a function of lateral position. The tunneling current I_{tun} between the surface and the tip is governed by the effective barrier height Φ, the applied tunnel bias V_{tun}, and the tip-surface distance d. For small biases around the Fermi level, it can be described in first approximation as:[43]

$$I_{\text{tun}} \propto V_{\text{tun}} \exp\left(-1.025 \cdot \sqrt{\Phi} \cdot d\right) \tag{2.9}$$

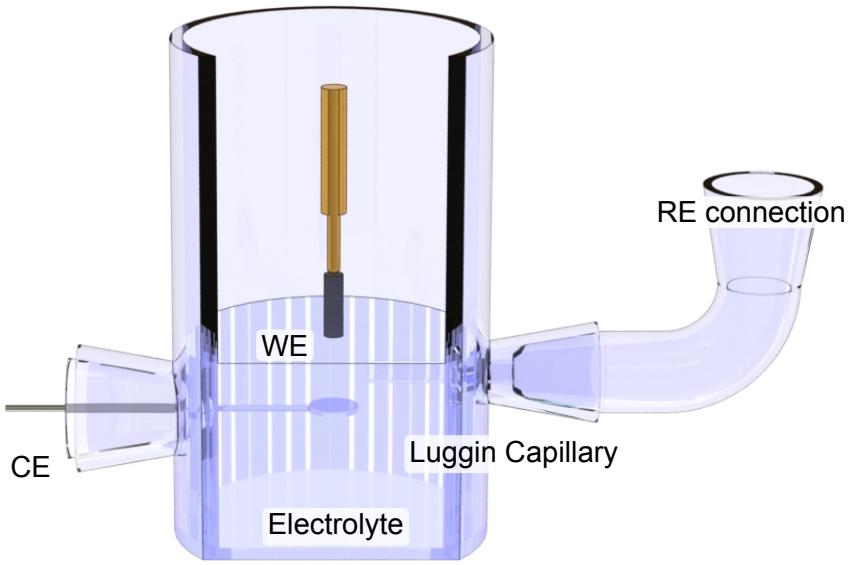

Figure 2.5. Model of the electrochemical cell tailored for impedance spectroscopy measurements. WE and CE are positioned in a coplanar way with the RE in the mirror plane. The electrolyte filling height is adjusted to match the NS14 connection for the RE.

For ultra-high vacuum STM (UHV-STM), equation (2.9) is valid for distances larger than a few angstrom, where the formation of chemical bonds is negligible. Under liquid conditions, the tunneling deviates from the exponential behavior even at higher distances and is therefore not adequately described by this simple model (see chapter 2.2.2).[44]

2.2.2. Tunneling in Liquids

In this work, the tunneling process occurred mostly in liquids at the solid-liquid interface. The tunneling process through an embedding medium, e. g. water or other solvents is different from that at the sample-vacuum interface, which is well known for UHV-STM.[45] The missing ordered structure of liquids and gases does not only change the dielectric medium between the tip and surface, but it also induces structural and electronic changes to the medium in the tunneling gap itself.

Polar and Redox-Inactive Liquids

Due to the solvation stabilization of electrons in a liquid environment, the effective barrier height Φ in ECSTM experiments is lowered drastically compared to ultra-high vacuum conditions. In Table 2.1, the barriers for different experiments are summarized.

Table 2.1. Barrier heights for different tips, surfaces, and conditions.

tip	substrate	conditions	Φ / eV	ref.
Pt-Ir	HOPG	in air	0.6	[46]
Pt-Ir	HOPG	H_2O	0.1	[46]
Pt-Ir	Au(111)	10 mM $NaClO_4/H_2O$	1.0	[47]
Au	Au(111)	H_2O	0.17	[48]
Au	Au(111)	1 mM $NaClO_4/H_2O$	0.62	[48]
Au	Au(111)	100 mM $NaClO_4/H_2O$	1.6	[48]
Au	Au(111)	500 mM $NaClO_4/H_2O$	0.04	[49]

Besides the lowered tunnel barrier, the non-exponential behavior of the tunnel current, at small tunnel gaps, known also for UHV-STM, begins already at larger gaps in a water ambient.[47,50] The linearization of I_{tun} for small distances d can be seen in Figure 2.6a. This effect can be attributed to the reduction of the applied tunnel bias V_{tun} for $d < 8\,\text{Å}$ (see open circles in Figure 2.6a). Under UHV conditions, this drop starts at $d < 2\,\text{Å}$. The reason for this earlier drop is a further reduced tunnel resistance at smaller distances.[48]

In order to account for the potential drop, the one-dimensional barrier model from equation (2.9) is rewritten with the conductivity term $G_{\text{tun}} = \frac{I_{\text{tun}}}{V_{\text{tun}}}$ to:

$$G_{\text{tun}} = G_{d=0} \cdot \exp\left(-1.025 \cdot \sqrt{\Phi} \cdot d\right) \tag{2.10}$$

where $G_{d=0}$ is the conductivity in the moment in which tip and sample touch. The actual barrier height Φ can be derived from the slope of the $\ln(G_{\text{tun}})$ versus d plot (see Figure 2.6b). The addition of ions to the water leads to an electrochemical double-layer (EDL) formation.[33] The Debye-length of the EDL is usually larger than the tunneling distance and should only have a minor effect on the tunneling process. However, it was found that the tunnel barrier is changing drastically when ions are added. Even though Figure 2.6b suggests a tunneling barrier trend concerning the concentration of ions, it was not possible to rationalize the origin of the different line slopes.[48]

Woo et al. [48] reported that a variation of the tunnel bias changes the tunnel gap in a semi-logarithmic manner when the tunnel current is kept constant (see Figure 2.7a).

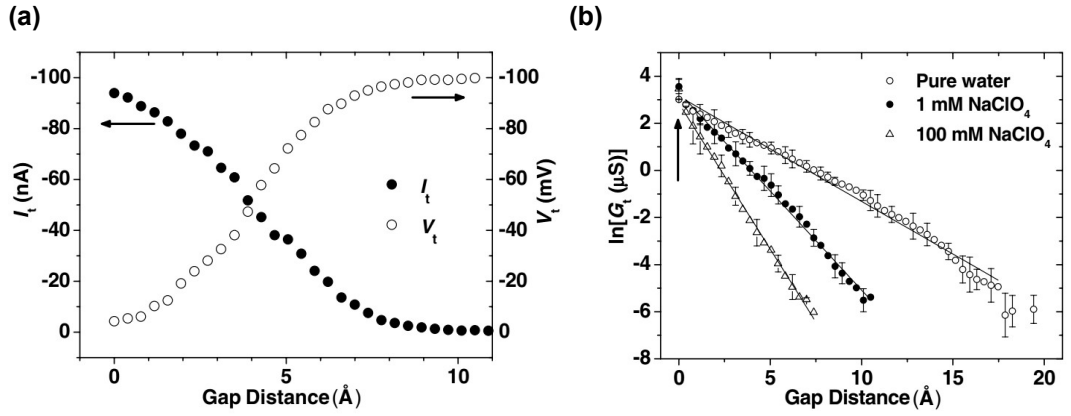

Figure 2.6. **(a)** The tunnel bias drops at lower distances (open circles). This results in a non-exponential behavior of the tunneling current (filled circles). Reprinted from D.-H. Woo et al., *Surface Science* **2007**, *601*, 1554–1559, with permission from Elsevier. **(b)** Averaged conductivity behavior against tunnel gap distance for different solutions. Although a concentration trend might be seen, the electrolyte composition does not scale in a predictable manner. Reprinted from D.-H. Woo et al., *Surface Science* **2007**, *601*, 1554–1559, with permission from Elsevier.

The inverse slope corresponds to the tunnel barrier height. It varies strongly for positive (negative) applied voltages: 0.56 eV (1.04 eV) in pure water, 0.66 eV (0.73 eV) in 1 mM $NaClO_4$ solution, and 0.60 eV (1.76 eV) in 100 mM $NaClO_4$ solution. Besides the polarity effect on the tunnel barrier, the authors report a strong dependence on the tip shape.[48]

Toney et al. [52] have shown with x-ray scattering experiments that a charged silver surface leads to the polarization of the first three molecular water layers. If the surface is negatively charged, the hydrogen atoms of the water molecule point towards the surface. In the case of a positive surface charge, the H_2O rotate until the negative end of the dipol points towards the surface. This molecular polarization was measured by Hugelmann and Schindler [51] with an ECSTM. Figure 2.7b, which shows the tunnel current against the tunnel gap, gives a deeper insight into the non-exponential behavior. Apart from the strong deviation at higher distances, where the interfering O_2-reduction takes place (Faraday regime), the current shows a prominent sinusoidal feature. The wavelength of this curve corresponds to layers of water in the tunnel gap. The variation in current corresponds to tunnel barrier changes between 0.8 and 2.3 eV.[51]

Several theoretical techniques have been applied to provide a better understanding of the tunnel mechanism: numerical simulations[53], molecule dynamic

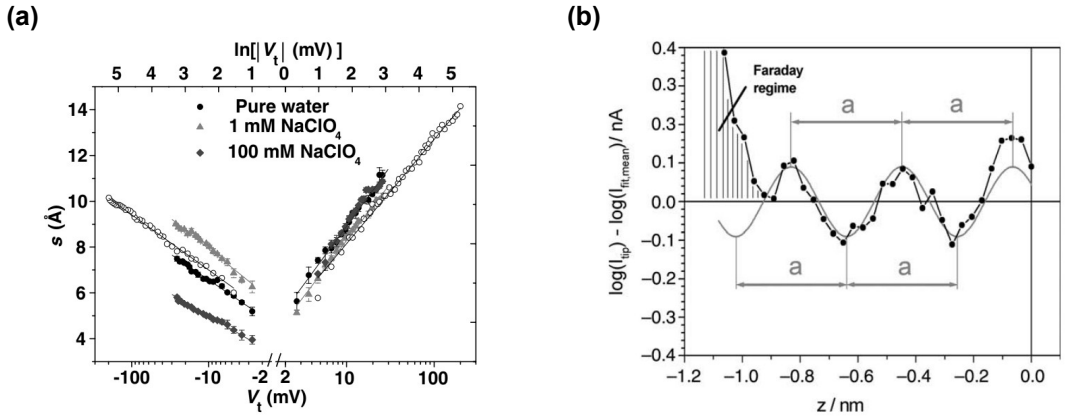

Figure 2.7. **(a)** Tunnel distance against the applied tunnel bias. The current was kept constant at 0.3 nA. Reprinted from D.-H. Woo et al., *Surface Science* **2007**, *601*, 1554–1559, with permission from Elsevier. **(b)** Oscillation of the tunnel current because of different water layers in the tunnel gap. Reprinted modified from M. Hugelmann, W. Schindler, *Surface Science* **2003**, *541*, L643–L648, with permission from Elsevier.

simulations[54], and density functional theory.[55] So far, a full explanation for the tunnel mechanism in liquids is lacking. The huge variation of tunnel barrier heights for different tips or tip-surface distances pose a challenge for the interpretation the observed chemical and morphological contrasts in ECSTM experiments.

Redox-Active Adsorbates

If a redox-active species is placed between tip and surface, the tunnel mechanism might change to a two step electron transfer (ET), as first described theoretically by Schmickler and Widrig [56]. Experimental findings in this field are best described by the Kuznetsov-Ulstrup model.[57,58] In addition to the regular tunnel current, a further current contribution is suggested.[58] Figure 2.8 shows the charge transfer from the support's Fermi level to the lowest unoccupied molecular orbital (LUMO) of the redox molecule, if fluctuations lower the LUMO until alignment with the Fermi edge. For the second ET, three scenarios are possible: (1) The resonant ET includes an immediate charge transfer without relaxation of the redox molecule or the environment. Since an additional channel for the overall electron transfer from the tip to the support is opened, this leads to the highest current enhancement of the three cases. (2) Some redox molecule can vibrationally relax before the ET. If the electronic coupling of the redox center with the support is weak, the ET rate is small and the second ET to the tip is independent of the first and again resembles a Franck-Condon transition. (3) A strong electronic coupling of the molecule leads to a high ET rate which results in an intermediate situation, partially resonant or vibrationally relaxed.[59]

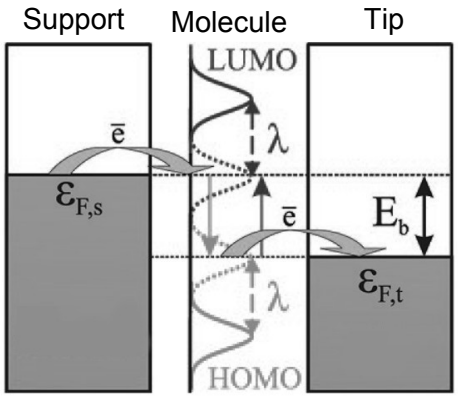

Figure 2.8. Electron transfer mediated by a redox-active molecule in the tunnel gap. Reprinted modified with permission from I. V. Pobelov, Z. Li, T. Wandlowski, *Journal of the American Chemical Society* **2008**, *130*, 16045–16054. Copyright 2008 American Chemical Society.

2.2.3. Tip Current Contributions

The current I_{tip} measured at the ECSTM tip consists of three contributions, as described by equation (2.11). The tunnel current I_{tun} depends on the tunnel bias U_{tun}, and the tip-surface distance d. The faradaic current I_{far} depends on the electrochemical tip potential U_{tip} and the tip area A exposed to the electrolyte. Finally, the capacitive current I_{capa} originates from a double layer restructuring, induced by changes to the tip or working electrode potential. Similar to the faradaic contribution, also the area of the tip influences the capacitive current.

$$I_{\mathrm{tip}}(U_{\mathrm{tun}}, U_{\mathrm{we}}, d, A) = I_{\mathrm{tun}}(U_{\mathrm{tun}}, d) + I_{\mathrm{far}}(U_{\mathrm{we}}, A) + I_{\mathrm{capa}}\left(\frac{\mathrm{d}U_{\mathrm{tip}}}{\mathrm{d}t}, \frac{\mathrm{d}U_{\mathrm{we}}}{\mathrm{d}t}, A\right) \tag{2.11}$$

If the ECSTM is used for topography measurements, only the tunnel current is of interest as a tip contribution. This current usually ranges from pA to uA, which can be superimposed by the faradaic and capacitive currents – usually in the range up to the mA scale. In this work, several strategies were employed to disentangle those three contributions and achieve a good signal-noise ratio:

- As both unwanted current contributions depend on the tip area, the most obvious strategy is to aim for a small tip surface exposed to the electrolyte. This can be achieved by coating the majority of the tip with a polymer (see chapter 2.4.2 for experimental implementation).
- The capacitive contribution is only measured at sudden and high potential changes. During an ECSTM experiment the tip and surface potential should therefore only be changed by approx. 10 mV increments.

- Usual tip materials are Platinum/Iridium alloys, which are known to be very good catalysts for the hydrogen and oxygen evolution reaction. The potential range in which the ECSTM tip is operated should be chosen accordingly to avoid reaction at the tip (see Figure 2.14b for the range determination).

- If the leakage current of the two unwanted contributions exceeds the usual, low pA range, the ECSTM measurement can be conducted at higher tunnel currents, which boosts the imaging capabilities.

2.2.4. Experimental Setup

The ECSTM setup with all attached measurement and control electronics is shown in Figure 2.9. The ECSTM itself is placed on three metal plates with different diameters inside of the aluminum cube and therefore with varying eigenfrequencies. As each metal plate will only vibrate at its own eigenfrequency, a damping of mechanical vibrations with different frequencies is ensured. A gas-tight aluminum cube reduces external electromagnetic fields and air turbulence. It permits working under inert gas atmospheres, including a saturation of the gas atmosphere with the electrolyte solvent to reduce drift phenomena. The chamber sits on a massive granite plate and is suspended inside a wooden box with bungy cords. This again helps to decouple external vibrations and acoustic noise from the setup. The vibration of the bungy suspension is damped by eddy brakes at each side of the granite plate. The eddy brakes are implemented via strong neodymium magnets on the granite plate, which induce a current in some mm distant copper metal plates fixed to the outer wooden box (see inset Figure 2.9).

The STM part of the setup is controlled by RHK *SPM100* electronics. The electrochemical control is implemented with a *Picostat* potentiostat from Molecular Imaging. Three DAQ boards (National Instruments *6341*, *myDAQ*, and Data Translation *3016*) establish the interfaces to the two computers (Fujitsu *Esprimo P710* and Dell *Precision 390*). The RHK software *XMPro v.2.0.1.6* is responsible for the STM measurement and the National Instruments *Labview v.2018* graphical programming environment is used for the communication with the DAQ boards.

The ECSTM itself used in this work was developed by Wilms et al. [60]. Figure 2.10 shows the two main parts: the STM base containing the sample and the STM head with the sharp metal tip. Both parts contain piezos, which allow the geometrical

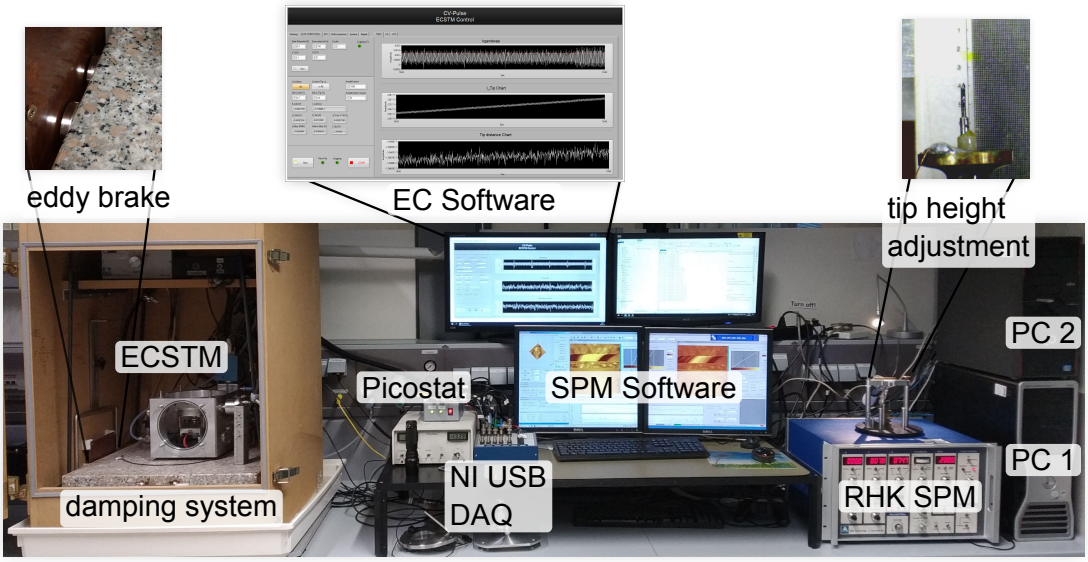

Figure 2.9. The ECSTM measurement setup: The insets show the eddy brake to damp mechanical vibrations of the bungy cords, the Labview EC Software, and the tip height adjustment tool.

movement of the tip with respect to the sample. The base piezos are responsible for the coarse approach of the tip to the surface. The head scanner piezo permits lateral movement and a height expansion of a few nanometers, which is needed for scanning over the surface. The head part is set on top of the base after mounting the sample and tip. The electrical connection is ensured with a *Lemo* multicontact connector.

Tip Approach

The tip approach of this beetle type STM towards the surface is done in two steps. (1) The black rotor with three inclined planes is lowered with the scanner piezo and tip until it rests on the three base piezos. (2) The rotor is then rotated by a slow expansion of the base piezos and a fast contraction. This leads to a little slip of the rotor planes on the spheric sapphires and the tip is further lowered. After each coarse base piezo step the scanner piezo is fully elongated and the tunneling current is monitored. When the current reaches the setpoint, the approach is completed.[60] The parameters and sawtooth voltage profiles are given in appendix A.2. The rotor three 120 degree planes, allow for a maximal movement of 0.3 mm.[62] The tip length has therefore to be adjusted before the approach (see inset in Figure 2.9), to avoid a tip crash during step (1). On the other hand, the tip has to stick out sufficiently, otherwise it will never reach the surface because of the limited approach range.

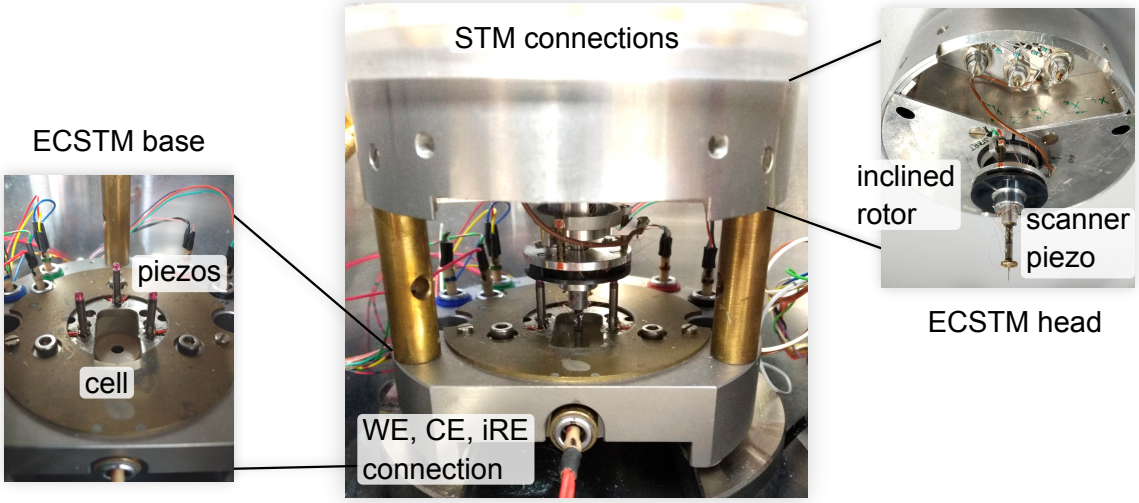

Figure 2.10. The ECSTM design by Wilms et al. [61] with base and head parts, which can be easily disassembled for sample and tip exchange. The cell contains the electrolyte and the sample. The head part with the tip mounted in the scanner piezo is lowered from above and the inclined rotor is placed on top of the three base piezos.

Four Electrode Setup

In addition to the well-known three electrode setup for electrochemical experiments (see section 2.1), the ECSTM tip is introduced as a fourth electrode.[63] There are two general ECSTM working principles: The tip voltage can be adjusted with regard to either the WE or the RE. The former working principle leads to a constant tunnel bias, whereas the latter ensures that the tip potential is fixed during an electrochemical experiment. Both approaches display their advantages in certain experimental situations. While referencing the tip voltage to the working electrode potential (constant tunnel bias) results in a more reliable imaging, it also bears the risk of unwanted faradaic reactions at the tip if harmful voltages are reached.

Figure 2.11a shows the electronic wiring of the setup schematically. The tip is grounded via the RHK *SPM 100* electronics and all other electronics are referenced with respect to this grounding. This is important to avoid ground loops, that would induce noise. The *SPM 100* generates the high voltages, that control the piezo motors for the tip movements. During the setup, the base and scanner piezos can be disconnected via two switches inside the wooden box to avoid an electrical discharge during the exchange of sample and tip. The measured STM current signal is transformed into a voltage signal by either of two current amplifiers. The internal amplifier board uses OPA128LM and OP07CP operational amplifiers and is located inside the ECSTM

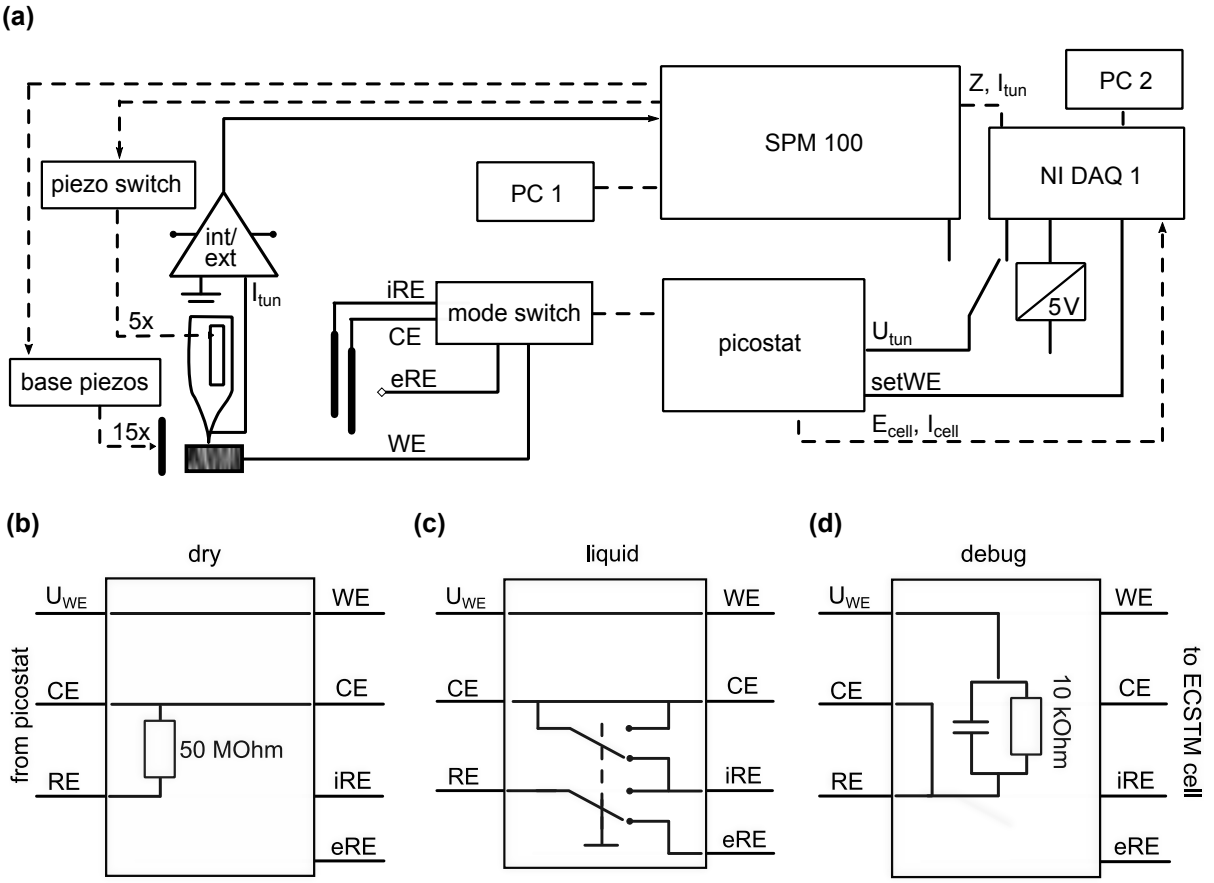

Figure 2.11. **(a)** ECSTM four electrode setup. Dashed lines indicate several connections. **(b – d)** Different ECSTM measurement modes and their respective wiring: **(b)** ambient STM operation in air, whereby the electrochemical feedback is deactivated through connection of CE and RE, **(c)** ECSTM operation with potential control either versus internal or external RE, and **(d)** disconnected electrochemical cell for testing with a RC circuit.

head. The external *Femto* DLPCA-200 current amplifier facilitates the switching of amplification and temporal response, due to its accessibility. This is extremely helpful for electrochemical measurements since the used ECSTM currents can easily reach up to several nA, while ambient STM measurements usually do not exceed the pA range. A jumper switch in the STM head and a flip switch at the backside of the *SPM 100* determines which amplifier is used. The tunnel current voltage is fed into the *SPM 100* electronics and is digitized by the PCI DAQ card *3016* in PC 1. While most of the measurement control is done with analog potentiometer controls, the data acquisition is performed via a RJ45 interface by the XMPro (*version 2.0.1.6*) software on PC 1.

The ECSTM has been exclusively used in the constant current mode, where the vertical tip position (i. e. piezo voltage) is regulated to match the current setpoint while

scanning. The feedback control responsible for the height regulation is based on a proportional and integral control, which acts like a low pass filter:[64]

$$u(t) = K_p \left[e^t + \frac{1}{T_N} \int_0^t e^t dt \right] \tag{2.12}$$

Hereby, K_p is the gain factor, T_N the time constant, and $e(t)$ the control deviation, which result in the output $u(t)$. Increasing the gain value K_p will influence both proportional and integral part, while the time constant only influences the integral part. The input current can be taken into account linearly or exponentially by the *SPM 100* electronics. A linear current input offers more robustness against sudden topographical height changes during measurement, while the exponential fits better to the experimental dependence of the tunneling current and distance described in equation (2.9) leading to a more accurate translation of the current signal into topography. Established initial values for approach and first measurements are $K_p = 3$ and $T_N = 2$ and a linear current input. The digitization range of the tunnel current voltage can be set to improve the height resolution of the topography, but should only be used when the surface is flat and no sudden obstacles are expected. The thermal drift of the system might change the tip-surface distance. The scanner piezo can only compensate a limited displacement and therefore the piezo offset (regulated on a separate piezo section) should be continuously adjusted to a central elongation position. In this way the scanner section of the piezo can adjust in both directions equally and does not require large control voltages. The tilt between the tip and the orthogonal surfaces axis will result in a tilted current signal. This could be compensated by the *SPM 100* electronics, but more advantageous is the rotation of scan direction until it aligns with the contour line of the surface. The scan area is controlled by the software, but is limited by the voltage range of the x- and y-part of the scanner piezo. The range can only be adjusted via the potentiometer controls at the *SPM 100*. The measurement area should not fall below 20% of the total voltage range, otherwise a loss in resolution could occur.

The electrochemical measurement is enabled through the *Picotstat* potentiostat from Molecular Imaging, which can reference the three potentials of WE, CE, and RE versus an additional fourth potential and therefore allows the introduction of the tip as a fourth electrode. The National Instrument data acquisition board *6341* builds up the interface between the National Instrument *Labview* software on PC 2 and the Picostat. The applied WE voltage, the measured cell potential, and current are directly connected to the Picostat. Depending on the referencing mode, which can

be determined by the software on PC 2, the relay either directly uses the bias voltage from the *SPM 100* or a calculated value U_{tun} (see equation (2.13)) to shift the picostat potentials up or down.

$$U_{\text{tun}} = U_{\text{we}} - U_{\text{tip}} \tag{2.13}$$

Hereby, U_{tip} is the potential of the tip with respect to the reference electrode. Figure 2.11b – d shows the four different modes the ECSTM can be operated. The picostat electronics demands a small current flow between the WE and CE in order to control the voltage. In dry conditions this is not feasible and the WE potential would float and influence the STM measurement. Therefore a 50 MOhm resistor is placed between CE and RE, which allows for the regulation of the potentiostat. Figure 2.11c depicts the wiring in electrochemical conditions. The WE can either be referenced versus an internal electrode, i. e. a platinum wire, or against an external reference electrode. In the second case, the internal Pt wire is shorted to the CE wire, which avoids the floating of the internal Pt wire. Figure 2.11d shows the debug mode, in which the electrochemical cell is disconnected and replaced by an −RC− element, similar to an electrochemical double-layer.

Drift compensation

The STM measurement, especially with immersed tip, can encounter strong drift of the tip horizontal and vertical in respect to the surface. This drift is a result of very small temperature differences, caused by the thermal expansion of certain setup parts, e. g. tip. For the study of surface dynamics of certain features or particles it is important to measure the same spot for a longer time. It is therefore very advantageous to be able to correct this movement and retain the same absolute measurement position. While the vertical drift can be easily adjusted during the measurement with the z offset, the lateral movement cannot be corrected while imaging by the RHK *SPM 100* electronics.

The drift correction is implemented with the existing x modification input of the *SPM 100* and an added y modification input. The electronic modifications at the log board of the *SPM 100* is shown in appendix A.3. Those two analog inputs to the *SPM 100* allow the x- and y-addition to the scanner piezo voltages and externally shift the STM imaging area. For the interface between the *SPM 100* and the PC 2 a National Instruments *USB myDAQ* analog-digital converter is used. A *Labview* program written by Schmid et al. [65] enables the control over the drift correction.

Sampleholder and Cell Design

The sampleholder for ECSTM should fulfill the mechanical stiffness needed for STM measurements, the chemical inertness for electrochemistry, and a simple sample transfer. The two sampleholders used in this work are shown in Figure 2.12a – b. The sampleholder design in Figure 2.12a was designed by Wilms et al. [60]. The key components are: ① The CE and internal quasi RE, which can be used as an additional CE in case of an external reference electrode. Both electrodes are metallic Pt wire. ② A polyetheretherketone (Peek) electrolyte vessel, which is shown in Figure 2.12c – d. Flat samples like HOPG or gold-coated glass can be mounted in the flat vessel type (Figure 2.12c). Single crystals like ④ or other cylindrical shapes fit well in the original design by Wilms et al. [60] (Figure 2.12d). ③ A *Kalrez* o–ring with 4 mm diameter and a high chemical inertness ensures a tight sealing. The components ④ – ⑦ ensure a good fitting of the sample. With the three screws in ⑦ the o-ring is squeezed and an electrolyte leakage is avoided. ⑧ The metal tub incorporates all parts and ensures the electrical connection with the built-in gold metal pins. The Lemo socket in the sampleholder nozzle allows the electrical connection to the Picostat. The main difference between the two sampleholder designs is the improved handling of contact pressure-sensitive single crystals. While in sampleholder 2.12a the sample has to be flipped and dropped into the peek vessel, the novel design 2.12b allows a careful placement of the sample on top of the sample tablet ⑨ and the peek vessel can be mounted while no sample flipping is needed.

2.3. Further Experimental Setups

2.3.1. Atomic Force Microscopy

Atomic force microscopy (AFM) is another scanning probe technique. Instead of a tunneling current, the intrinsic attraction and repulsion of materials is exploited to gain structural insights. For more details see reference [66]. A Park *XE-70* AFM operated in non-contact measurement mode was used in this work. It has a flexure-guided X, Y, and Z scanner, which allows the measurement of large samples up to 50x50 µm without background curvature. The approach is enabled by an optical microscope.

2.3.2. Scanning Electron Microscopy

A detailed description of the Scanning Electron Microscope (SEM) can be found in reference [67]. In this work a FEI *Magellan 400 XHR* SEM with FEG source was used. It was operated at 5 kV electron beam energy and a dwell time of 100 ns.

2.3.3. X-ray Photoelectron Spectroscopy

The x-ray photoelectron spectroscopy (XPS) is used to probe the core level of surfaces. The x-ray beam leads to an ejection of electrons with a certain kinetic energy. This energy allows chemical insights on the studied surfaces. A detailed description can be found in reference [68].

Three XPS setups were used in this work: (I) A Leybold-Heraeus *LHS 10* spectrometer with a non-monochromatized aluminium K-alpha source (1486.7 eV). The chamber background pressure was below 5×10^{-8} mbar. (II) The project described in chapter 4 was measured with a XPS setup located at the Chair E20 of the Physics Department and further described here [69]. A pass energy of 20 eV was used for all measurements. Due to the limited reproducibility of the sample mounting and x-ray intensity, no absolute intensity values are shown and compared between two different measurements. (III) For the chapter 5 a PHI *VersaProbe 1* was used to perform XPS. A Mg K-alpha (1254 eV) was used as a x-ray photon source. The samples were glued on the transferable sample holder with conductive silver epoxy glue.

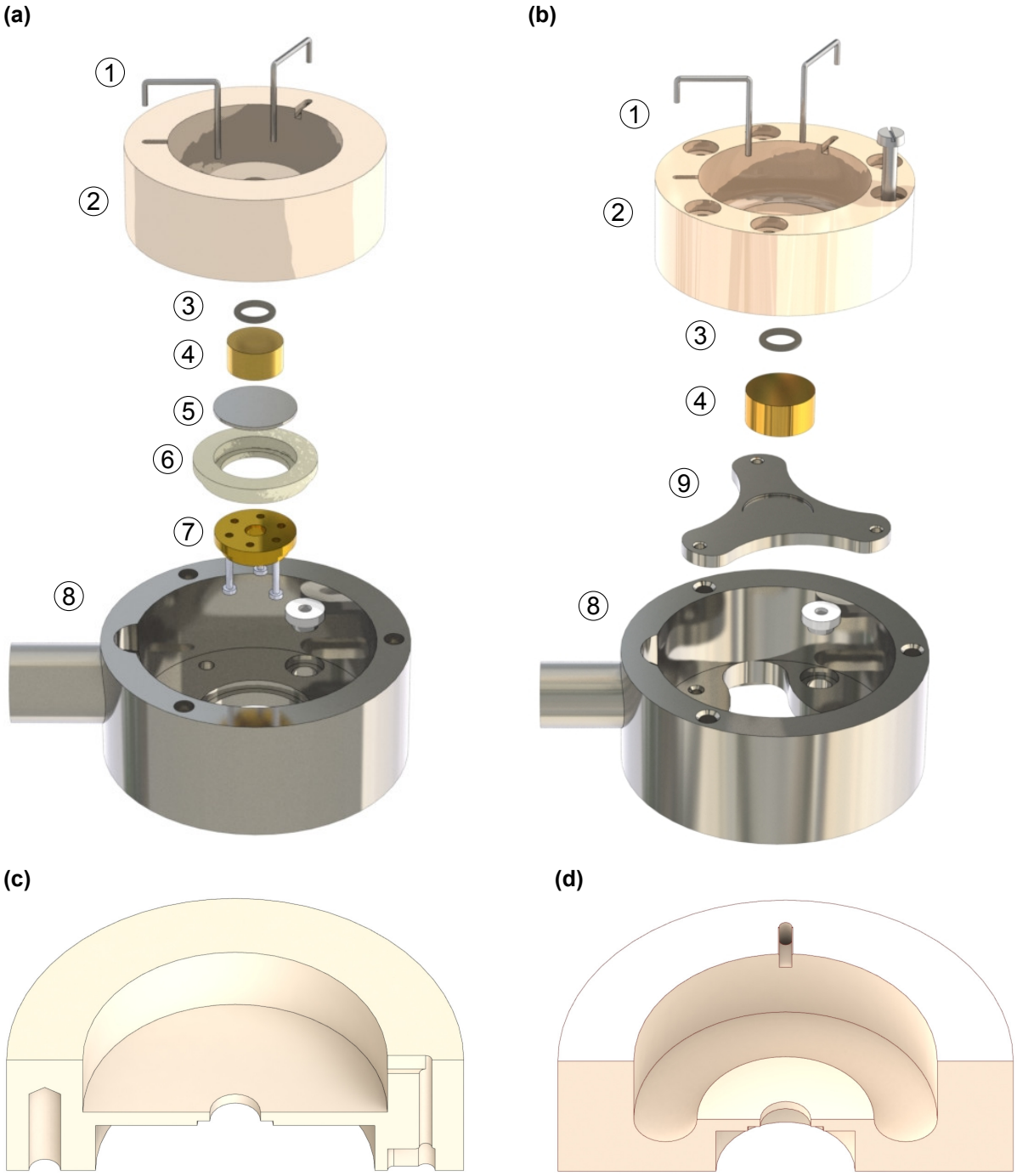

Figure 2.12. **(a)** The sampleholder design by Wilms et al. [60] in explosion view. **(b)** Improved sampleholder for sensitive single crystals, derived from (a) and designed in this thesis. The components in **(a – b)** are described in the text. **(c – d)** Cut views of the Peek sample holder for different samples. **(c)** is used for HOPG and gold films on glass samples, while **(d)** is utilized for gold single crystals.

2.4. Materials and Chemicals

The used chemicals and materials, including the suppliers used in this work are listed in Table 2.2.

Table 2.2. Materials and chemicals used in this work.

Surfaces	
Au(111) single crystal	Mateck Ø 8 x 4.3 or Ø 10 x 5.0 mm
Au(111) on glass	Arrandee
Au(111) on mica	Georg Albert University Heidelberg
HOPG	HOPG H grade: µmasch HOPG A grade: TipsNano, NTMDT
Glassy carbon	HTW Sigradur G
Electrochemistry	
Pt wire for CE/RE	Mateck (purity 99.9%)
Ag/AgCl reference electrode	SI Analytics, ScienceLine
Argon	Westfalen Argon 6.0
Hydrogen	Westfalen Hydrogen 6.0
Ultrapure water	Milli-Q Reference System, 18.2 $M\Omega\,cm^{-1}$, TOC < 5 ppb
STM	
Pt/Ir tip wire	Advent Research Materials Ltd, Pt/Ir 80:20, Ø 0.25 mm
Base scanner	Piceramic 45260
Head scanner	Piceramic 37389
Piezo glue	EPO-TEK H20E
Tip coating	Apiezon® *Wax W*, T_M: 403 K
STM o-ring	DuPont Kalrex Ø 3.99 x 0.99 mm

2.4.1. Surface Preparation

Au(111)

In this work, three different gold samples were used: Au on glass, Au on mica, and Au single crystals. While gold samples on glass and mica cannot be cleaned after usage, the Au single crystal can be electrochemically etched. The Au(111) single crystal surface preparation is based on the report from Kibler [70]. The gold crystal is etched at 3 V vs Pt in 3 M H_2SO_4 for 2–3 min, until a red gold oxide layer is formed. The oxide layer is then dissolved in 6 M HCl. The gold crystal is rinsed with ultrapure water (18.2 $M\Omega cm^{-1}$). Subsequently, the crystal is heated with a hydrogen flame until red heat and kept there for 2–4 min. The crystal is cooled down slowly under Argon gas atmosphere. Depending on the quality of the crystal and the annealing process a flat crystal with large ($\approx$ 100 nm) terraces will be obtained. The Au film samples are flame annealed in a similar manner, but due to the thin Au layer a delamination can easily occur. Therefore, the sample is heated very carefully, by slowly moving it through the flame and as soon as a red color occurs, the heating is stopped. The Au surface structure can be determined by measuring the potential of zero charge: Au(111)(1x1) results in 0.56 V vs RHE and Au(111)($\sqrt{3}$x22) gives 0.65 V vs RHE.[71]

Highly Oriented Pyrolytic Graphite

The highly oriented pyrolytic graphite (HOPG) is freshly cleaved with scotch tape prior to each experiment. In order to avoid carbon flakes on the surface, that could be picked up the STM tip, we used a clean Kimtech wipe to finger-press loose flakes on the surface.

Glassy Carbon

As glassy carbon (GC), 5x5 mm cylindrical *Sigradur G-Discs* samples from Hochtemperatur-Werkstoffe GmbH were used. They are delivered with one polished side (Ra < 50 nm) and are pressed into the Teflon sampleholders, as shown in Figure 2.4. The samples are repolished prior to each measurement on a polishing cloth using sequentially two solutions: suspended (1) Ø 0.1 and (2) 0.05 µm AlO_x particles. The movement on the polishing cloth should correspond to an eight, in order to remove equally the carbon material from all over the surface.

For the project described in chapter 5 a diamond based polishing suspension was used, as residues of AlO_x were seen in SEM to remain on the sample. An additional electrochemical polishing step can as well remove remaining residues. In the three electrode setup, the surface was therefore swept ten times between -0.5 and 0.5 V vs Ag/AgCl with 50 mV s^{-1} scan rate.

Gold Nanoparticle Preparation

The Au nanoparticles for the experiments in section 5 were prepared by physical vapor deposition from gold in a molybdenum crucible. A flux of 0.2 Å/s was adjusted with a quartz microbalance and then the shutter was opened for 10 s. The intrinsically poor wetting of gold on glassy carbon leads to spontaneous nanoparticle formation. The sampleholder contained several GC samples, which were rotated to ensure an even deposition.

2.4.2. STM Tip Preparation

The resolution of an STM is mainly determined by the shape and the chemical condition of the used tip. As a stable and inert tip material only Pt/Ir has been used in this thesis. The general approach for the preparation of a suitable STM tip is the mechanical rupture of a metal wire. Due to the metallic binding, which allows the non-elastic deformation, an opposed force acting on the wire leads to narrowing and finally full separation, resulting in two sharpened ends.

Within this thesis two ways of tip preparation have been used: (1) Cutting tips by the mechanical rupture of the Pt/Ir wire. (2) Electrochemical etching in alkaline solution until finally gravimetrical pull leads to rupture.

Mechanical Cutting

For the preparation of cut tips, the wire is fixed with a pointy-noise plier. Subsequently, a diagonal cutter is placed in an angle of 45 ° and the wire is ripped apart with limited pressure on the cutting device. The mechanically cut tips are mainly used for STM measurements under ambient conditions, as the coating of those asymmetric tips was not as successful as with etched tips. Figure 2.13a shows a STM tip created by mechanical cutting.

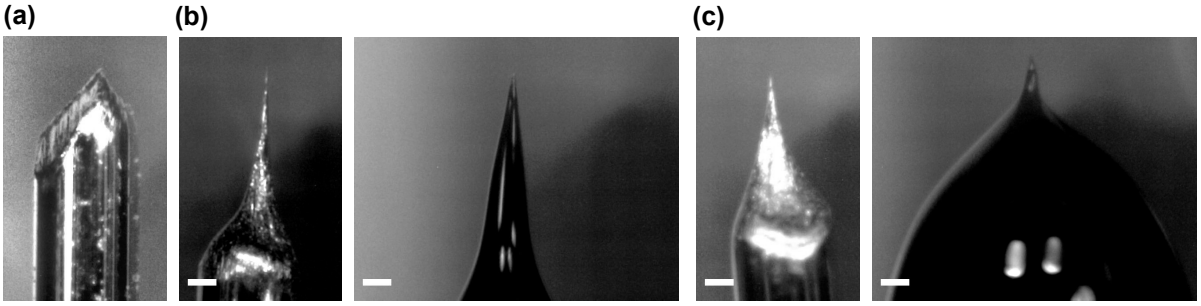

Figure 2.13. **(a)** Mechanically cut tip. **(b – c)** Two examples of etched tips before (left) and after coating (left). The two different immersion depths, **(b)** 1 mm and **(c)** 0.8 mm during the etching process influence the sharpness of the tip and the obtained shape of the coating. The white bars represent 0.2 mm.

Etching Procedure

The etching of the Pt/Ir wire is another approach to create STM tips. The end of the wire is protected with an adherent plastic tube and dipped into the etching solution (aqueous 1 M KOH + 2 M KCN), until unprotected metal wire is exposed to the electrolyte. By applying a positive square AC voltage between the tip and a conductive graphite beaker, the wire is etched.[72] A two step etching routine was used, as seen in the current response to the applied AC voltage in Figure 2.14a. In the first part, a 5 V square wave with a offset of -2 V was applied to quickly reduce the wire diameter. After a time of approx. 200 s the second etching part starts, now without voltage offset. This is indicated in Figure 2.14a by the second vertical line. The milder etching with a lower current ensures a less roughened tip surface. The etching immediately stops after the current drops below a given threshold (in Figure 2.14a after 855 s), which indicates a suddenly reduced surface area as result of the occurred wire cut. The protective plastic sleeve is removed from the dropped tip, which is ready for use after rinsing with water, acetone, and isopropanol.

Throughout this thesis, several different etching conditions have been tested to optimize the tip sharpness as well the ability to recover from crashes. Variation of tips shapes also influence strongly the coating result (see Figure 2.13). Tips with an immersion depth of 0.8 mm showed the best performance after coating. The high voltages during the etching procedure lead to gas evolution at the tip from the water splitting reaction. This bubble formation interferes the etching and results in asymmetric tip shapes. The spikes in the low-current phase in Figure 2.14a are attributed to this release of gas bubbles. The smaller the spikes are, the more symmetrical is the resulting tip.

Tip Coating

The tips are polymer-coated for the use in the ECSTM setup (as explained in chapter 2.2.3). The tip is therefore pushed through a melted wax film (Apiezon® *Wax W*, T_M = 403 K). Hereby, the majority of the metal tip gets coated, except for the sharp apex, that remains uncovered. Figure 2.13 shows the coating result of etched tips.

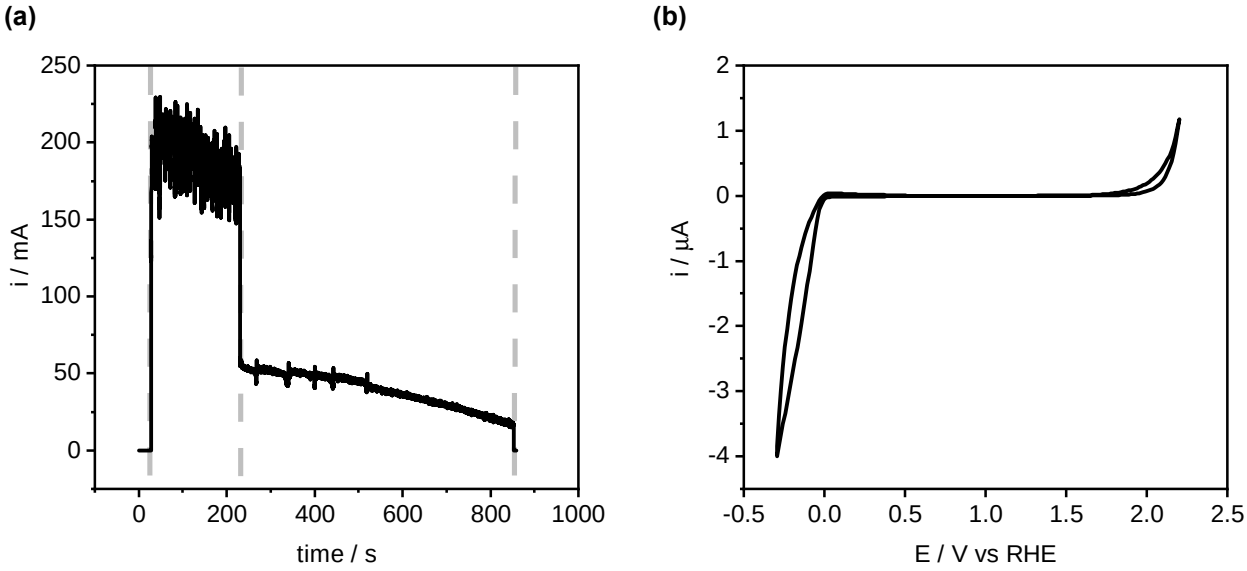

Figure 2.14. **(a)** Current response of tip etching routine. The vertical lines indicate the two phases which differ in the additional –2 V offset of the 5 V AC square voltage wave in the first phase. The second phase without the offset shows a lower current, which leads to a smoother tip surface. The spikes in the second phase are attributed to bubble formation at the wire. **(b)** Cyclic voltammogram of a Pt/Ir tip in 0.1 M $HClO_4$. The HER and OER reaction limit the potential range in which the tip can be operated.

Tip evaluation

In order to improve the tip preparation, the evaluation of ECSTM tips is important. While it is very difficult to predict the imagining capacities of a fresh tip, we still inspect the tip shape with an optical microscope before the coating procedure. The coating itself can be more easily assessed by electrochemical methods. After connecting the tip as WE in a three electrode setup we performed a CV exclusively in the non-faradaic regime from 0.4 to 1.5 V vs RHE to determine the capacitance of the tip without destroying it (see Figure 2.14b). Typical values of well coated tips are 9.5×10^{-10} C. The exposure of a tip to the potentials outside of this range, will reduce the quality of the tip and should therefore be avoided before and during imaging. A more simple and less destructive approach for the characterization of an adequate coating is the immer-

sion of the tip in the electrolyte at the non-faradaic potential regime, while measuring the tip current. While th capacitive current decays after some time, the targeted final leak current should be below 30 pA.

2.5. Data Evaluation and Reproducibility

2.5.1. Documentation

Every measurement performed throughout this work is listed with all relevant parameters and a unique identifier in Microsoft *Excel* spreadsheets, which are compiled and converted to reading friendly and long-time supported file formats (see section 2.5.2). Any further modifications of the ECSTM setup are documented in a scanned handwritten labjournal. Both data and documentation, are stored on the file server of the Chair of Physical Chemistry at the Technical University Munich.

2.5.2. Proespm Software

The data analysis was performed with a self-written Python 2.7 command-line program named proespm, published under GNU General Public License 3.[a] A copy of the current source code can be obtained at `www.github.com/n-bock/proespm`. This software automates the data processing steps, the compilation to readable output formats such as image and html files, and also includes external lab journal information. Furthermore, it also creates a data management structure on the file server for an easy access to the stored raw data.

The key component of the software package is the creation of the interactive and explorable html reports for each sample, containing all performed preparation and analysis techniques. Each measurement is linked to the information stored in the Microsoft *Excel* labjournal, identified by its file name, and also to the raw and processed data files for further analysis.

The current version supports the processing of Cyclic Voltammetry, Impedance Spectroscopy, Chronoamperometry, Raman Spectroscopy, X-ray Photoelectron Spectroscopy, Scanning Electron Microscopy, Atomic Force Microscopy, and (Electrochemical) Scanning Tunneling Microscopy data.

[a] `https://www.gnu.org/licenses/gpl-3.0.de.html`

3. Towards Size-Controlled Deposition of Pd Nanoparticles from Polyoxometalate Precursors

Contributor Roles

Nicolas Bock: Investigation, Visualization, Writing
Astrid De Clercq: Investigation, Visualization, Writing
Lukas Seidl: Investigation
Tim Kratky: Investigation
Tian Ma: Resources
Sebastian Günther: Resources
Ulrich Kortz: Resources
Ueli Heiz: Resources, Funding acquisition
Friedrich Esch: Conceptualization, Supervision, Funding acquisition

This section 3 contains a full reprint of the publication N. Bock et al., *ChemElectroChem* **2021**, *8*, 1280–1288 [73] published under *Creative Commons Attribution-NonCommercial-NoDerivs* license.[a]

[a]The license can be obtained from `https://creativecommons.org/licenses/by-nc-nd/4.0/`.

ChemElectroChem | Articles
doi.org/10.1002/celc.202100131
Chemistry Europe
European Chemical Societies Publishing

Towards Size-Controlled Deposition of Palladium Nanoparticles from Polyoxometalate Precursors: An Electrochemical Scanning Tunneling Microscopy Study

Nicolas Bock[+],[a] Astrid De Clercq[+],[a] Lukas Seidl,[b] Tim Kratky,[a] Tian Ma,[c] Sebastian Günther,[a] Ulrich Kortz,[c] Ueli Heiz,[a] and Friedrich Esch*[a]

We present a novel in situ electrochemical approach to deposit small size-controlled palladium(0) clusters from 12-Pd^{II}-oxometalate precursors. These clusters are formed through the reductive surface polarization of a Au(111) support. Electrochemical scanning tunneling microscopy (EC-STM) reveals that the electrochemical reduction occurs at much lower potentials than that for simple Pd salt solutions. The resulting particles are one atomic layer high and show a narrow size distribution. Precursor mass transport limitations and preconditioning of the solid-liquid interface at low potentials influence the obtained morphology. In particular, a concomitant reduction mechanism via formation of molecular hydrogen is discussed. The deposited clusters show the typical behavior of small metallic Pd islands in EC-STM: The apparent cluster height increases reversibly when lowering the potential close to the onset of hydrogen evolution, which is attributed to hydrogen adsorption.

1. Introduction

In the search for an efficient production of alternative green mobile energy carriers such as hydrogen and other synthetic solar fuels, a fundamental understanding of their catalytic synthesis at the solid-liquid interface is crucial. Platinum Group Metal (PGM) alloys remain the most active catalytic material in many of these applications and moreover they seem to be inevitable in neutral solutions, which could give benefits in terms of durability compared to the standard harsh acidic or alkaline conditions.[1] As their high cost inhibits widespread commercialization, an effective strategy has been to reduce metal loading by finely dispersing it in the form of nanoparticles.[2] The particles' size can be controlled down to atomic precision. For nanometer-sized metal clusters, this opens up the possibility to steer their morphological and electronic properties for a desired reactivity, exploiting quantum effects in the non-scalable size regime. Such atom-by-atom size dependences have been intensely studied at the solid-gas interface, demonstrating that single atom differences can indeed cause significant variations in catalyst performance.[3] While size-selected clusters can be prepared in vacuum systems by laser ablation or magnetron sputtering and subsequent mass selection, an extension of these studies to the solid-liquid interface has been hampered by the limitations of a sample transfer from vacuum into liquid under atmospheric conditions. Nevertheless, beneficial turnover rates per atom were reported for some specific sizes and reactions in liquid.[3–6]

An alternative strategy is the wet-chemical deposition of metal complexes with an exact number of noble metal atoms in a surrounding stabilizing ligand shell. Examples for such an approach are the impregnation of a support by platinum octanethiolate[7] or polyoxopalladates(II) (POPs) and the subsequent calcination and reduction towards the active metallic state.[8] POPs have also been investigated as molecular precursors for heterogeneous catalysts through incorporation into metal organic frameworks (MOFs).[9] POP-based heterogeneous catalysts with a well-defined size distribution show promising catalytic properties ranging from cross-coupling reactions[10,11] to hydrogenations.[8] The calcination step, however, leads to an unwanted increase in size and therefore the unique potential of these complexes as precursors for size-selected clusters remains largely unexplored.

Otherwise, direct wet-chemical synthesis of metal particles in the liquid phase[12] can be achieved by the dendrimer[13] or micelle-encapsulation[14] technique. Here, Imaoka et al. demonstrated that so-formed Pt_{12} clusters on a carbon support show a more than 2-fold increase in reactivity compared to Pt_{13} in the oxygen reduction reaction (ORR).[13] However, even if these wet-

[a] N. Bock,[+] Dr. A. De Clercq,[+] T. Kratky, Prof. Dr. S. Günther, Prof. Dr. U. Heiz, Dr. F. Esch
Catalysis Research Center and Chemistry Department
Technical University of Munich
Lichtenbergstr. 4, 85748 Garching, Germany
E-mail: friedrich.esch@tum.de
[b] Dr. L. Seidl
Department Mobility, Energy & Environment
Swiss Federal Laboratories for Materials Science and Technology
Überlandstrasse 129, 8600 Dübendorf, Switzerland
[c] Dr. T. Ma, Prof. Dr. U. Kortz
Department of Life Sciences and Chemistry
Jacobs University
Campus Ring 1, 28759 Bremen, Germany
[+] These authors contributed equally to this work

Supporting information for this article is available on the WWW under https://doi.org/10.1002/celc.202100131

chemical methods pave the way for a deposition beyond flat surfaces, e.g. onto powders and into porous supports, they encounter specific limitations related to the removal of the protective ligand shell and require a compromise between activation and agglomeration.[15]

In this work, we explore instead a different, electrochemical route, to dissociate and deposit POP precursors to form metallic Pd clusters. The family of discrete POPs shows distinct stoichiometries – POPs with n = 12 up to 84 could be prepared[16] and are sufficiently labile to be decomposed electrochemically, or alternatively by pH changes or contact with molecular hydrogen.[8,17,18,19,20,21] We decided to study in particular the POP with an "open-shell" structure, $[SrPd_{12}O_6(OH)_3(PhAsO_3)_6(OAc)_3]^{4-}$ (**$SrPd_{12}$**, structure see Figure S1), which we reduced directly at the solid-liquid interface, obtaining well-defined palladium(0) cluster sizes. Synthesis and structural details can be found in Yang et al.[17] This "open-shell" polyanion **$SrPd_{12}$** was selected due to its presence of acetate and phenylarsonate ligands, the former being sterically less demanding than the latter. This structural feature is expected to facilitate electron transfer in the reduction process, as compared to for example the highly symmetrical, closed-shell $CaPd_{12}$ nanocube or $BaPd_{15}$ nanostar with exclusively phenylarsonate ligands.[17]

Other POPs and Pd^{II}-containing heteropolytungstates have already been used to electrodeposit extended Pd films that showed high stability, fast hydrogen sorption/desorption kinetics, and high electrocatalytic activity in reactions such as hydrazine and alcohol oxidation.[18,19,20,21] However, the unique microstructure of these Pd films has neither been studied in detail at the nanoscale nor optimized. Other 3*d* transition metal-containing POMs, such as Mn^{II}-containing heteropolyanions, were successfully deposited and characterized at the nanoscale with intact ligand shell[22] and with stripped ligands,[23] but without reducing the oxygen framework prior to the catalytic application.

Here, we use a combination of electrochemical and microscopic techniques to determine the possible deposition mechanisms and their effect on the particle morphology. Electrochemical Scanning Tunneling Microscopy (EC-STM) has already proven to be a powerful method to investigate in situ, at the local scale and under potential control the deposition of small Pd particles from simple salt solutions and their properties.[24–29] As supports, both reconstructed Au(111)–$(22\times\sqrt{3})$ and unreconstructed Au(111)–(1×1) surfaces were used, as well as Highly Oriented Pyrolytic Graphite (HOPG). Pd on Au supports is known to be active in the hydrogen evolution reaction (HER). Since the boundary between Au and Pd represents the most active centers, a controlled fine Pd dispersion that maximizes the boundaries is of particular interest.[29]

In addition to deposition experiments at constant potential, cyclic voltammetry (CV) studies have been performed. Previous CV studies of a variety of POPs showed a dominance of the pronounced redox behavior of the oxidized palladium(II) metal centers that get reduced concomitantly with the irreversible POP decomposition.[30] A similar behavior was expected as well for the POP used in this work, $[SrPd_{12}O_6(OH)_3(PhAsO_3)_6(OAc)_3]^{4-}$ (**$SrPd_{12}$**). By steadily lowering the substrate electrode potential, the electrochemical reduction of the Pd^{II} metal centers to Pd^0 and the concurrent deposition of metallic Pd on the working electrode surface is expected to occur, while the attached ligands are stripped off and remain in solution.

Moreover, we focus in this article on the morphology of the obtained particles under reactive conditions at the verge of hydrogen evolution. Beyond this electrocatalytic application, the size-controlled deposition of Pd particles might have a larger impact in particular for specific fine-chemical syntheses: As Pd is well known to facilitate C–C coupling reactions, a systematic investigation at the solid-liquid interface is expected to give insight into the catalyst dynamics and the strong solvent influence on the reaction yield.[31]

2. Results and Discussion

2.1. Electrochemical Reduction of $SrPd_{12}$

In order to investigate the deposition process in detail, a highly resolving local method is required – here, in situ EC-STM has been used. The Au(111) support is reconstructed after preparation in flame annealing. Under potential control, this reconstruction is stable up to 0.4 V vs RHE (reversible hydrogen electrode). In order to lift the reconstruction without formation of Au adatoms, a chemical treatment in Cl^- containing solution is applied. Cl^- traces have been removed before the deposition experiments. If not stated otherwise, these experiments were performed on unreconstructed surfaces. As electrolyte for the deposition, a neutral phosphate buffer was chosen, as both the **$SrPd_{12}$** and the created nanoparticles are more stable in neutral solutions. Phosphate ions are known to form just an amorphous adlayer in neutral pH,[28] at potentials above 0.5 V vs RHE. OH^- anions, as well present in the electrolyte, are known to adsorb at potentials above 0.4 V vs RHE (see Figure S2 in the Supporting Information).[28,32]

We started with an experiment on the unreconstructed surface in which the surface potential is subsequently lowered stepwise, starting from 0.6 V vs RHE, after adding **$SrPd_{12}$** to the phosphate buffer electrolyte. As shown in the EC-STM images acquired at different working electrode potentials in Figure 1, no deposition is observed in the potential region of 0.4 to 0.6 V vs RHE, even over a time span of 1 hour (Figure 1a). However, the **$SrPd_{12}$** gets indeed into the surface vicinity, as demonstrated by quartz microbalance measurements that indicate an increased double layer viscosity and loading upon POP addition (Figure S3). The metal deposition sets only in when lowering the potential below 0.2 V vs RHE. This potential is much lower than that of supported Pd oxide (Pd^{II}/Pd^0) that we determined to be around 0.7 V vs RHE in this electrolyte (see Figure 2) or to the underpotential deposition from Pd-salt precursors such as $Pd(NO_3)_2$,[33] $PdCl_2$,[34] and $PdSO_4$ from aqueous electrolytes.[35] Although the μM **$SrPd_{12}$** concentrations used in this work are relatively low as compared to other Pd electrodeposition studies,[26,33,36] we still see immediate deposition of small single-layer-high particles when the surface potential is set below

ChemElectroChem | Articles
doi.org/10.1002/celc.202100131
Chemistry Europe
European Chemical Societies Publishing

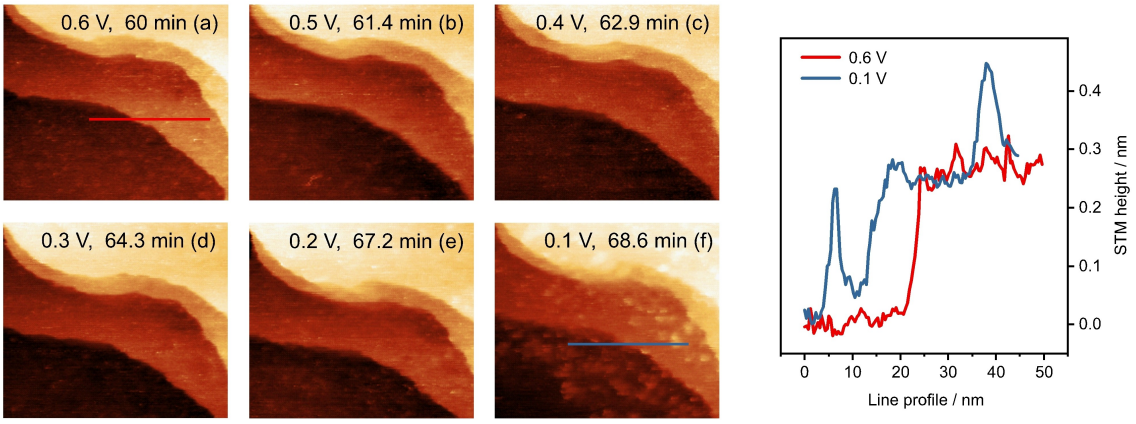

Figure 1. In situ EC-STM images (a-f) of the deposition of Pd clusters from the **SrPd$_{12}$** precursor solution by lowering the Au(111) working electrode surface potential in subsequent potentiostatic steps; particles evolve at potentials below 0.2 V vs RHE. The 50 nm horizontal profiles (right) corresponding to the lines in (a) and (f), which indicate the successful deposition of small single-layer-high Pd clusters. Imaging conditions: a–e) $U_b = -100$ mV; f) $U_b = -200$ mV, $I_t = 0.7$ nA at the indicated working electrode surface potentials. Image size: 90×80 nm^2. Concentration: 0.3 μM **SrPd$_{12}$** in phosphate buffer (total amount corresponding to 1.1 Pd-monolayers).

0.2 V vs RHE, which indicates that sufficient amounts of **SrPd$_{12}$** precursor are present near the surface.

As observed in the line profiles of Figure 1, the deposited particles have an apparent height that corresponds to that of a monoatomic step of the Au(111) surface, in line for two materials of similar lattice constants. This height should not be influenced by the presence of residual POP -ligands or Sr^{II} ions that are all expected to be released into solution during deposition. This is evidenced by XPS spectra of the working electrode after rinsing with water and transferring to UHV (see Figure S4) where As and Sr are absent. Detailed Au 4d$_{5/2}$ spectra (Figure S5) evidence the presence of a Pd 3d$_{1/2}$ shoulder. This shoulder indicates the presence of metallic Pd.

For comparison, arrows pinpoint the Pd 3d$_{1/2}$ energy position of Pd^{2+} and Pd^{4+} species, respectively. The deconvolution of the overlapping Au 4d$_{5/2}$ and Pd 3d core level peaks can be performed, but does not lead to precise peak intensity values. Instead, the Pd MVV Auger electron yield is used to quantify the amount of deposited Pd particles (see Figure S6) confirming that the particles resolved in EC-STM entirely consist of Pd.

The low POP reduction potential compared to that of single Pd ions could be caused by thermodynamic, as well as by kinetic effects. The ligand structure around the oxygen-bridged Pd core in **SrPd$_{12}$** will shift the standard electrode potential of the Pd^{II}/Pd^{0} couple. Furthermore, an overpotential could arise from reorganization energy contributions linked to the ligand removal upon reduction or limited electron transfer through the ligand shell.

We exclude that the **SrPd$_{12}$** deposition is related to local changes in the pH that cause their decomposition outside neutral conditions. It has been shown that only minimal pH gradients would appear near the working electrode in similarly buffered phosphate electrolytes, especially near the pK$_a$ point where our experiments were performed (resulting in pH differences < 1).[37]

In order to further understand the reduction mechanism, cyclic voltammetry (CV) has been performed. Figure 2(a) shows the reduction behavior of the **SrPd$_{12}$** precursor on an Au(111) surface. The deposition cycle (red) was started at a potential where little POP is oxidized but above the PdO$_x$ reduction. As no PdO$_x$ reduction feature is visible, the **SrPd$_{12}$** is not yet decomposed so far. At potentials below 0.3 V vs RHE, the electrochemical **SrPd$_{12}$** reduction appears in the form of a broad peak. This reduction step yields metallic Pd particles, which matches well with the H ad-, absorption, and evolution features on Pd observed thereafter.[38] The lower vertex potential overlaps with the onset of the hydrogen evolution reaction (HER), therefore we expect further **SrPd$_{12}$** precursors reduction in the solution, leading to less specific, additional Pd deposition. Such processes lead e.g. to the formation of Pd black when purging a **SrPd$_{12}$** solution with hydrogen gas (see Figure S7). Continuing with the anodic sweep of the CV, we observe hydrogen desorption from the Pd particles at 0.2 V vs RHE and oxidation of the metallic Pd particles at 0.9 V vs RHE. After exchanging the electrolyte to remove **SrPd$_{12}$** precursors in the solution, the CV measurement is repeated and indeed the PdO$_x$ is reduced at 0.7 V vs RHE.

Figure 2b describes the electrochemical behavior observed when cycling towards higher, oxidizing potentials, starting from near OCP conditions. Since the **SrPd$_{12}$** ions are negatively charged, they are attracted to the surface at anodic potentials and can undergo an oxidation process. Most likely, the ligands are oxidatively separated and bare PdO$_x$ is deposited. The known phosphate adlayer observed at these potentials seems not to hinder this electron transfer and hence a surface blocking effect as seen for sulfate[26] can be excluded. The presence of PdO$_x$ manifests again in a reduction peak, here around 0.75 V vs

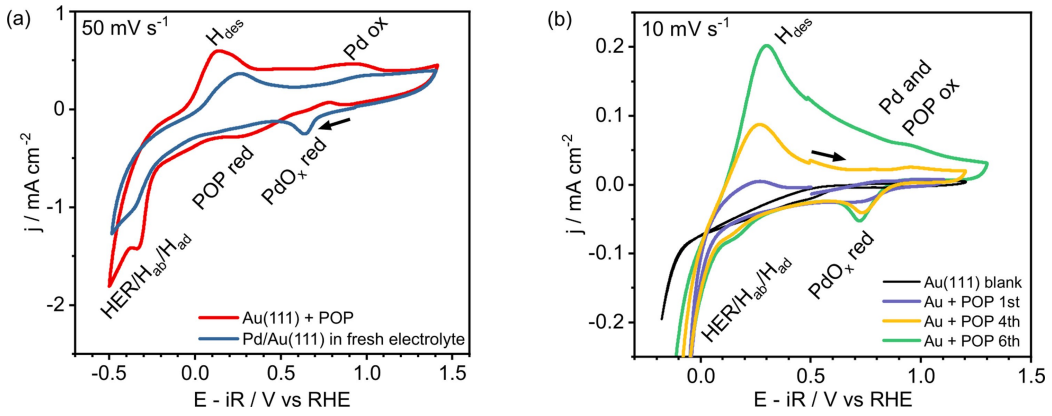

Figure 2. Cyclic voltammograms of Au(111) surfaces in a **$SrPd_{12}$**-POP solution. a) Reductive deposition process (red line) at high POP concentrations, starting from 0.9 V vs RHE directly in the cathodic direction, showing no PdO_x reduction features at 0.7 V vs RHE, but instead a broad peak at 0.2–0.3 V vs RHE, assigned to the electrochemical POP reduction. The cycle continues with entangled processes of H ad-, absorption, and evolution indicative of deposited Pd. This Pd gets oxidized in the anodic sweep at 1.0 V vs RHE. After rinsing and refilling with fresh electrolyte (blue line), a clear PdO_x reduction peak at 0.7 V vs RHE gets visible. b) Oxidative deposition process and following reduction of the PdO_x species on Au(111), starting from intermediate potential 0.5 V vs RHE, but cycling first towards higher anodic potential limits, where Pd species and deposited POPs get oxidized. The cathodic PdO_x reduction peak is now clearly visible from the first cycle on, indicative that Pd deposition has taken place at oxidizing potentials. Subsequent cycles demonstrate the ongoing deposition. Hereby, a pause of several seconds has been applied after every second cycle, in order to avoid the depletion of the **$SrPd_{12}$** precursor and to enhance the observed peaks. One CV of each pair is shown. The PdO_x reduction, H ad-, absorption, evolution, and desorption features increase with every pair of cycles and indicate the typical behavior of Pd on Au and at coverages that reach multilayer amounts. Applied concentrations: a) 10^{-3} M **$SrPd_{12}$**, pH 4 phosphate electrolyte, argon-purged; b) 10^{-5} M **$SrPd_{12}$** in pH 5.2 phosphate electrolyte, argon-purged.

RHE, that sets in already with the very first cycle, i.e. before applying the low voltages as used for the reductive deposition in Figure 2a. The PdO_x product of the oxidative deposition requires hence the same reduction potential as the supported PdO_x particles generated by reductive deposition of **$SrPd_{12}$**. The kinetic and thermodynamic barriers observed there seem no longer to apply.

The PdO_x reduction peak lowers in potential from 0.75 to 0.70 V vs RHE after stronger oxidation obtained by applying higher upper cycling potentials, a common observation for deposited Pd nanoparticles.[39] Furthermore, the CV spectra demonstrate how the hydrogen adsorption peak develops and shifts to ~0.2 V vs RHE with increasing cycle number. However, one has to take into account that also reductive deposition takes place at these potentials, which further increases the amount of deposited Pd in the successive cycles. The small shift of the hydrogen adsorption peak has been explained with a decrease of the lateral epitaxial Pd expansion with increasing layer thickness according to the d-band model.[40,41] We therefore deposited several ML of Pd in this experiment.

This oxidative approach promises another way to create atomically precise metal clusters, but would require a different support, since the Au(111) surface tends to roughen and form extended islands at higher potentials, which makes a distinction between Pd and Au particles hardly possible and hence prevents a detailed morphological analysis.

2.2. Resulting Particle Morphology and Dispersion

In the following, we continue with the reductive deposition, observing the initial stages of the electrochemical Pd deposition process and imaging the obtained particle morphology at high resolution by in situ EC-STM. As described before, the **$SrPd_{12}$** deposition requires a considerable low potentials, occurring only below 0.2 V vs RHE, where the reconstructed surface is stable. Hence no Au islands form that would act as nucleation sites for the deposition, when starting with a reconstructed surface. Even when starting with unreconstructed surfaces, the slow reconstruction kinetics keep the surface free from Au adatoms and holes, on the time scale of the deposition experiments.

As can be seen in Figure 3, a similar deposition of small particles takes place on both reconstructed and unreconstructed surface terraces, rather independent from the applied potential steps. Importantly, as shown in the inset of Figure 3a, one does not observe a preferential adsorption at step edges that would manifest in a step meandering, as observed for the small overpotential deposition of various Pd salts in different electrolytes by Köntje, et al..[33] Instead, the low potentials applied here result in a uniform and random distribution of small Pd particles on the flat Au(111) terraces, similar to the deposition from Pd salt solutions with moderate[42] to large overpotentials.[26,43]

While the nucleation on terraces is similar, the central question is whether the POP deposition gives access to a better size control. When characterizing area and height distributions in Figure 3c, care has been taken to apply only rather short potentiostatic treatments, to minimize concomitant coalescence

ChemElectroChem | Articles
doi.org/10.1002/celc.202100131
Chemistry Europe
European Chemical Societies Publishing

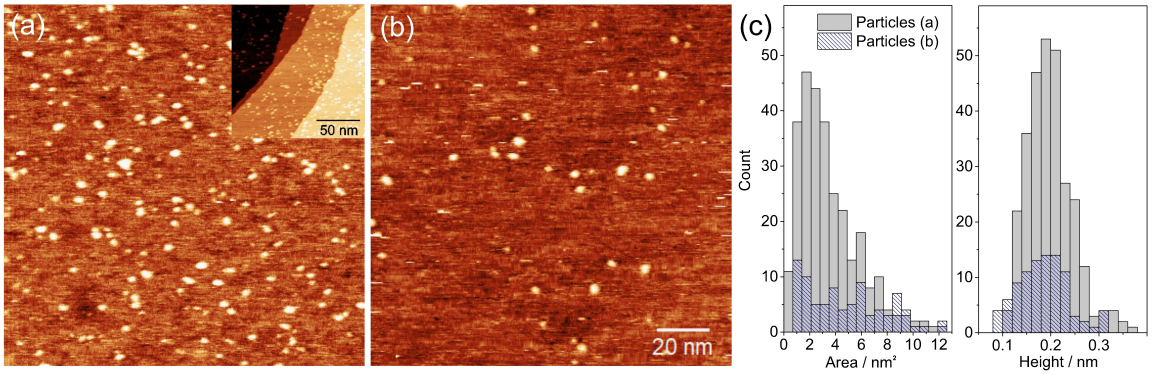

Figure 3. In situ EC-STM images of the deposition of Pd clusters from the **SrPd$_{12}$** precursor solution after two different preparation pathways: a) on unreconstructed Au(111) after 2 pulses of 500 ms at 0 V, inset: larger overview including steps with no preferential deposition; b) on reconstructed Au(111) after 3 treatments of 30 s at 0.2 V vs RHE. The faint parallel lines observed on certain parts of the surface indicate the presence of the herringbone reconstruction. c) Corresponding histograms of particle area and height. The clusters are almost exclusively one atomic layer high and show an area dispersion that starts with areas compatible to those observed for supported Pd_{12} clusters in UHV (apparent diameters of 2 nm, hence areas of 3 nm^2,[44]). The particle morphology is measured at 0.5 V vs RHE (a), resp. 0.4 V vs RHE (b) surface potential. Imaging conditions: a) $U_b = -150$ mV, $I_t = 2$ nA. b) $U_b = -28$ mV, $I_t = 0.35$ nA. Concentration: 0.1 μM **SrPd$_{12}$** in phosphate buffer (total amount corresponding to 0.5 Pd-monolayers).

and alloying with Au adatoms. Two recipes have been used: In Figure 3a, two short pulses of 500 ms at a low potential of 0.0 V vs RHE lead to a coverage of about 5%, as determined by the observed surface area, while in Figure 3b three longer treatments of 30 s at a less negative potential of 0.2 V vs RHE lead to a lower coverage of about 2%.

With both treatments, we observe similar distributions. In particular, both led almost exclusively to single-layer-high particles ($\geq$95%) with an apparent height of about 0.2 nm. This is in line with an expected epitaxial growth, as seen in most previous studies,[26,33] except for the very slow deposition in highly dilute electrolytes on the reconstructed surface by Uosaki et al., in which 3D particles up to three layers high have been found.[27] Note that different tip radii might slightly influence the observed area, but not the observed height distributions.

Remarkably, the prevalent observed particle areas at the small-size-onset are roughly 2.0 (a), resp. 1.5 nm^2 (b), corresponding to an average particle diameter of 1.4 to 1.6 nm. This apparent average diameter, enlarged by tip convolution effects, fits well the size observed for one single-layer-high Pd_{12} clusters supported on a boron nitride support by STM under vacuum conditions.[44] The two area histograms show distinct differences: the higher coverage histogram in (a), obtained by short potential pulses, is peaked at smaller cluster areas, while the histogram in (b), obtained by much longer potential treatments, is somewhat broader. Shorter deposition times seem therefore beneficial for the formation of small, size-controlled clusters, although the limited set of experiments makes it difficult to assign these to single, specific parameters. The histogram related to (b) shows furthermore indications for a peak sequence with about 2 nm^2 distance. This could be related to a preferential deposition close to already deposited Pd_{12} units, especially if the deposition is slow enough to overcome transport limitations. That the high coverage sample (a) does not show such a peak series, might be related to an enhanced ripening due to a higher particle coverage. For future deposition strategies, it might be helpful to deposit metal clusters from neutral[45] or positively charged POPs that do not get repelled from the surface upon reduction, instead of the strongly negatively charged one used here. This could be easily feasible as the potential of zero charge of Au(111) in phosphate electrolyte is around 0.6 V vs RHE.[46]

2.3. Hydrogen-Induced Deposition of $SrPd_{12}$

Due to the low potentials required, the electrochemical **SrPd$_{12}$** deposition takes place in a potential region where hydrogen adsorption starts to take place, especially once first traces of Pd have been deposited. This adsorption occurs already well before hydrogen evolution sets in (at potentials that depend strongly on the preparation conditions, about −0.1 V vs RHE on bare Au(111), 0.0 V vs RHE on Pd films, see Figure 2). In order to better understand how hydrogen formation and the presence of adsorbed hydrogen might modify the deposition, we performed several experiments described in the following.

We started with studying the **SrPd$_{12}$** deposition on an HOPG support, where the blank surface, contrary to Au(111), does not develop hydrogen at all in the investigated potential range, as seen in Figure S8. Upon POP addition and cycling, however, hydrogen adsorption and evolution can be seen as well. Hence Pd deposition must have taken place and occurred, at least initially, without the presence of adsorbed hydrogen. Later on, an intricate entanglement of deposition and hydrogen evolution is evidenced by the observed crossing of the CV currents at low potentials in the first two cycles. This points to a hydrogen-induced deposition of new active sites for hydrogen evolution during the voltage sweep. These consist of increasing amounts of deposited Pd^0 that shifts the hydrogen adsorption and evolution potentials towards more positive values in the second

and third cycle, until the shoulder at 0.2 V vs RHE appears as observed for Pd/Au(111). Due to the limited interaction between Pd cluster and the HOPG terraces, the cluster aggregate upon deposition, mostly at step edges, and the size distribution is lost.

From our hydrogen purging experiments we know on the other hand, as already mentioned, that the **$SrPd_{12}$** polyanions are unstable in the presence of hydrogen gas – an instant formation of black Pd aggregates is observed in solution (Figure S7). Such an effect has already been exploited for the wet-chemical synthesis of large Pd aggregates with sizes around 8 nm by reduction of heteropolytungstates containing 1 or 2 Pd^{II} ions.[47] We can therefore anticipate that this chemical reduction mechanism, in parallel to the electrochemical one, leads to the formation of particles with higher aggregation probability, lowering the size-control.

In order to get a closer insight via EC-STM measurements, we tried out different pretreatments of the solid-liquid interface at low potentials, where adsorbed hydrogen forms, at the verge of hydrogen evolution. These hydrogen species are not imaged by EC-STM, but have a strong impact on the Pd deposition when subsequently adding the POP, **$SrPd_{12}$**, at a surface potential of 0.3 V vs RHE or higher, where no deposition would occur in a pristine solution, even after a prolonged time of more than one hour (as demonstrated in Figure 1). The pretreatments consisted in (i) keeping the Au(111) surface at 0.1 V vs RHE for 90 min (result shown in Figure 4a) or (ii) at a lower potential of 0.0 V vs RHE for a shorter time of 10 min (result shown in Figure 4b) or (iii) after applying 6×500 ms potential steps at -0.1 V vs RHE and waiting for about 20 min (result shown in Figure S9). We then added **$SrPd_{12}$** and indeed, a spontaneous Pd particle deposition is observed that leads to completely different, large, flower-like aggregates shown in Figure 4.

This spontaneous deposition happens within a timeframe of less than five minutes, as these structures appear already in the very first acquired image and do not change thereafter in size or shape. The flower-like particles are randomly distributed, though a preferential attachment to step edges is observed. The apparent island shape in Figure 4a,b (left) depends strongly on the tip quality. Sometimes, one can still recognize voids and a strong height heterogeneity within the prevalently single-layer-high islands – this points to structures that form by a hit-and-stick aggregation followed by an only partial coalescence.

The process ends probably due to the consumption of a chemical species present at the solid-liquid interface and/or the electrolyte. This limiting species is not surface-near **$SrPd_{12}$**, even if only very small concentrations were used, corresponding to just 1.6 equivalent Pd monolayers that can be deposited at maximum: When lowering the surface potential again, the particle deposition as described earlier resumes. As shown in Figures 4a (right) and in Figure S9, further small Pd particles of an average equivalent diameter of 2.5 ± 0.9 nm are deposited from the same solution. Those small spherical particles are randomly dispersed and are not preferentially deposited near the flower-like structures or step edges. The small particles

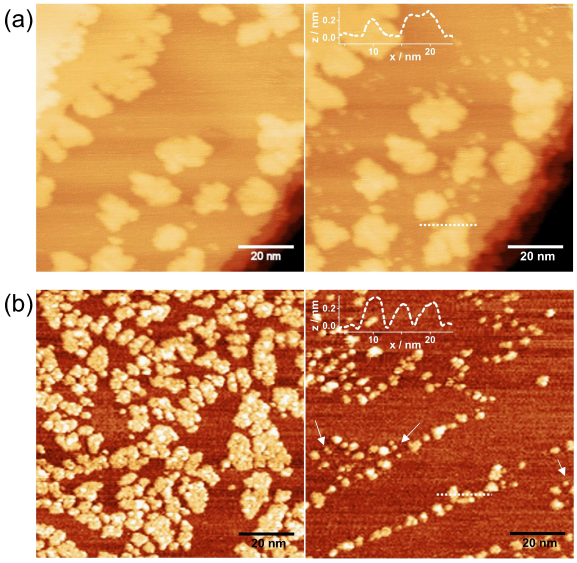

Figure 4. In situ EC-STM images indicating the formation of larger, flower-like Pd islands of one atomic layer height after different pretreatments of the solid-liquid interface at low potentials before addition of **$SrPd_{12}$**. Under these pretreatments, hydrogen species are formed. Experiment series (a): Aggregates appearing after keeping the surface for 90 min at 0.1 V vs RHE and sequentially adding **$SrPd_{12}$** precursor at a surface potential of 0.3 V vs RHE, i.e. at a potential where no deposition would occur in a pristine solution (left; compare with Figure 1); when lowering the potential again to 0.1 V vs RHE without changing the solution (right), small particles can again be deposited, in addition to the already present flower-like particles. Experiment series (b): Similar effects can be obtained by keeping the surface for only 10 min at a lower potential of 0.0 V vs RHE and adding the precursor again at 0.3 V vs RHE (left).; investigating a surface area kept directly under the tip (right) reveals the tip influence on local potential and transport: Less and much smaller aggregates are observed, down to sizes compatible with Pd_{12} (see arrows), decorating elbow sites. Imaging conditions: $I_t=0.2$ nA; $U_b=-100$ mV (a, left), $U_b=-300$ mV; (a, right) $U_b=-40$ mV (b). All images have been taken at 0.3 V vs RHE working electrode surface potential. Concentration: 0.4 μM **$SrPd_{12}$** in phosphate buffer (total amount corresponding to 1.6 Pd-monolayers).

therefore correspond well to the previously described electrochemical reduction mechanism.

The limiting species is hence hydrogen-related. Its formation seems to be confined to the solid-liquid interface that gets saturated upon the pretreatment – if the hydrogen species could evolve directly into solution, it would probably accumulate in quantities that react off the entire amount of solved **$SrPd_{12}$**. However, we cannot exclude that adsorbed hydrogen leaves the Au(111) surface after going back up in potential and that the chemical reduction occurs already in solution. In any case, the aggregation indicates that the POP reduction takes place in the vicinity of the nucleation centers, either directly by adsorbed hydrogen or from hydrogen in solution.

The influence of present hydrogen species on the Pd particle deposition was also stressed by previous investigations with EC-STM[43] and in situ TEM[48] that observed the formation of rough porous aggregates when applying potentials where hydrogen forms on the surface. They attributed the changes in

ChemElectroChem | Articles
doi.org/10.1002/celc.202100131
Chemistry Europe
European Chemical Societies Publishing

morphology to a competition for direct surface access between adsorbed hydrogen and the Pd precursor.

While usually the deposition was performed with a retracted tip, the experiment in Figure 4b explicitly addresses the influence of the tip during the deposition process. The left image displays the particle distribution when the tip was distant, the right one the distribution directly under the tip. One observes immediately that much less and smaller clusters have been deposited. The integrated area that is covered by Pd particles decreases by a factor of four. For Pd deposition on Au(111) from salt solutions, such a tip shielding effect was already hypothesized by Naohara, et al.[43] who suggested a precursor diffusion limitation to be responsible for a reduced deposition directly under the tip. Such transport limitation, by electrostatic and geometric shielding, will be even more important for large and four times negatively charged precursors such as the **SrPd$_{12}$**. In these experiments, the tip potential was constantly kept at 0.35 V vs RHE, also during the 10 min of 0 V vs RHE. This tip potential could also affect the local working potential of the surface under the tip, locally changing the effect of pretreatment and subsequent deposition.

Noticeably, at the low coverage of particles forming under the tip, we can observe a distinct preference for specific nucleation sites. As this deposition took place on a reconstructed Au(111) surface, we attribute the line order to the presence of elbow sites of the herringbone structure where nucleation is favored, as reported for UHV vapor deposited[49,50] or electrochemically deposited Pd particles on reconstructed Au(111).[27] The preference for defect sites and steps after hydrogen preconditioning underlines a considerable mobility of the particles forming in the deposition process, in line with the observed tendency to aggregate.

All the mechanistic considerations regarding chemical and electrochemical reductive deposition of **SrPd$_{12}$** up to now demonstrate the importance of a rational control of the surface potential before and during the deposition process for obtaining size-selected particles. In addition, an even better control could be gained at higher pH to further reduce the hydrogen production while remaining in the POP stability window.

2.4. Morphology Changes under Reaction Conditions

If the presence of adsorbed hydrogen changes the POP deposition dramatically, the question arises how stable the deposited particles are, once formed, under HER conditions. Since the XPS measurements suggested that the Pd particles are metallic, it is interesting to see whether they show the characteristic hydrogen adsorption signatures in STM. To that purpose we investigated the morphology in situ, in a fresh electrolyte, at low potentials. After the particle deposition (preparation as in Figure 3a), the reactor cell was thoroughly rinsed and refilled with pure phosphate buffer solution, in order to remove all non-reacted **SrPd$_{12}$**, while keeping the sample under potential control at 0.6 V vs RHE. The surface potential was then, in single potentiostatic steps, lowered to 0.0 V vs RHE and back to 0.6 V vs RHE for two consecutive cycles while being imaged by EC-STM (Figure 5).

A clear swelling of the Pd clusters is observed when lowering the electrochemical potential (Figures 5b, 5g). The shift in the height histogram in Figure 5d indicates an increase

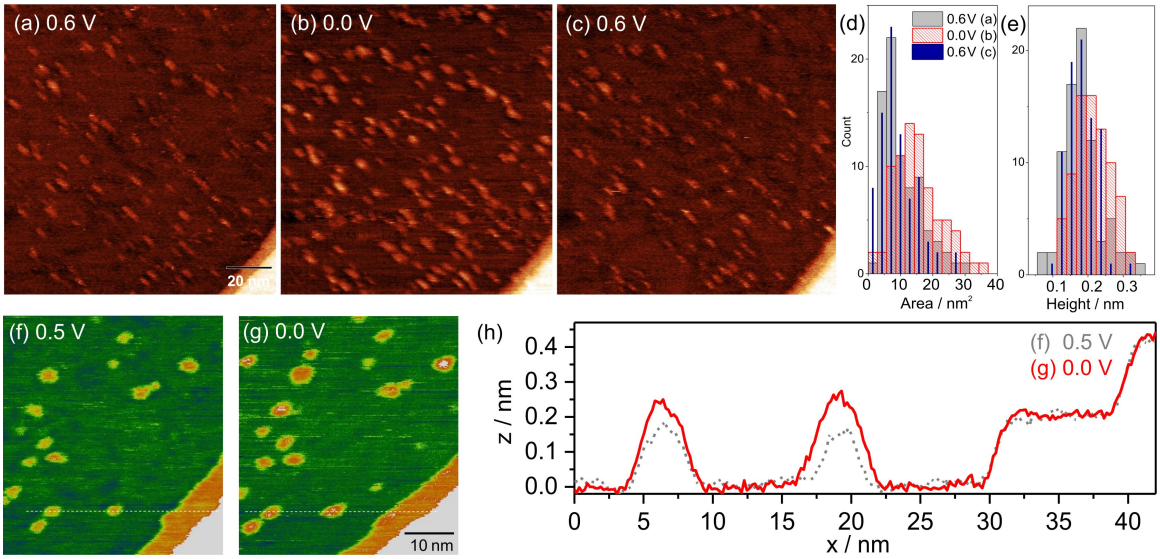

Figure 5. In situ EC-STM images indicating the influence of the surface potential on the apparent Pd particle morphology at the onset of hydrogen evolution: a-c) Images taken at indicated surface potentials; d, e) corresponding histograms of apparent particle area and height indicate a reversible increase of both at low potentials. f, g) Zoom images on potential-dependent particle morphology during a second potential cycle taken at indicated surface potentials. h) Corresponding line profile (dotted lines in f and g) indicates that only the Pd particle morphology changes while Au step edges remain unchanged. Imaging conditions: $I_t = 2$ nA, tip potential kept at 0.65 V vs RHE. Concentration: 0.1 μM **SrPd$_{12}$** in phosphate buffer (total amount corresponding to 0.5 Pd-monolayers).

by roughly 20%. This change in height concerns only the deposited Pd particles and not the Au support, as is clearly visible in the potential-dependent line profiles in Figure 5h. This points to the more active nature of the deposited Pd particles and rules out a tip-induced effect. Concomitantly, the apparent area increases by 70%, but, contrary to the straightforward height evaluation, this increase depends strongly on the threshold values used for the cluster area detection and might mostly be induced by a tip convolution effect linked to the height increase.

The swelling effect is reversible, as can be seen in Figure 5c. Since the corresponding histograms largely overlap with the initial ones, it is only a minute fraction of particles that undergoes ripening or irreversible changes. Such swelling of Pd particles has been observed before, on a Pt(111) support[51] and was attributed to hydrogen ad- and absorption into the Pd adlayer. Absorption, i.e. uptake into the bulk, can be excluded in our case, as the particles are just 1 ML in height and hydrogen absorption on Pd/Au(111) has been shown by Baldauf et al. to take only place starting from 2 ML.[52] The apparent height increase related to hydrogen adsorption might thus be explained by an electronic effect, i.e. an adsorbate-induced change in the electronic density of states.

Hydrogen-induced coalescence is only sporadically observed in these experiments, most particles do not ripen even at very close distance. We conclude that the particles, once formed, are stable under HER conditions, in contrast to the **$SrPd_{12}$** precursors that decompose under these conditions. In addition, the particles show indeed the same characteristic hydrogen adsorption signatures in the STM images at different surface potentials that are found for metallic Pd nanostructures deposited from salt solutions.

3. Conclusions

This study investigates by EC-STM a novel Pd cluster preparation technique on Au(111) where size-controlled particles are deposited by reduction of **$SrPd_{12}$** precursors. This reduction occurs at potentials below 0.2 V vs RHE and requires potentials lower by roughly 0.5 V, compared to the reduction of bare PdO_x particles in the same electrolyte, due to thermodynamic and kinetic effects related to the extended, complex **$SrPd_{12}$**-ligand shell. Besides the deposition by reductive decomposition, also an oxidative approach is investigated, in which deposition occurs via ligand removal prior to a subsequent Pd oxide reduction. Single-layer-high Pd clusters resulting from the reductive approach could be imaged in situ and show a very narrow size distribution, as long as low concentrations and short deposition times are applied.

Besides the electrochemical reduction, an alternative deposition route is observed, if hydrogen intermediates are present on the surface. This later route leads to large, flower-like Pd islands. Hydrogen-induced effects on the onset of the reduction in the electrochemical route can be excluded by deposition experiments on an HER-inert HOPG surface. Finally, the deposited small Pd clusters were studied at potentials around the onset of HER, where they behave similar to metallic Pd nanostructures that increase in apparent area and height due to hydrogen absorption.

This study paves therefore the way to deposit size-controlled Pd clusters for more systematic studies on size effects in cluster catalysis at the solid-liquid interface.

Experimental Section

All materials in contact with the electrolyte and sample like glassware and PEEK sample holder were cleaned with Caro's acid followed by rinsing at least three times with boiling ultrapure water. Unless stated otherwise a neutral 0.05 M phosphate buffer electrolyte was used, which was prepared from ultrapure water (18.2 MΩ), H_3PO_4 (Suprapur, Merck), and NaOH (monohydrate, 99.99%, Merck) with a pH of 6. The **$SrPd_{12}$** stock solution (0.2 g/L) is made in the same electrolyte and added during the experiment as indicated.

Cylindrically shaped Au(111) single crystals (Ø 8 or 10 mm, MaTecK) were used as substrates and cleaned prior to each experiment by oxidation in 3 M H_2SO_4 (Suprapur, Merck) until the formation of a reddish layer, which was removed with 6 M HCl. Subsequently, they were flame-annealed with a hydrogen flame at red heat for two minutes and slowly cooled down in high-purity argon atmosphere leading to the reconstructed Au(111)($22\times\sqrt{3}$) surface. As the reconstructions already lifts at the open circuit potential, it is important to control the potential prior to the insertion of the gold sample. The unreconstructed Au(111)(1×1) surface is prepared as the reconstructed surface, but followed by an additional 30 min immersion into a 0.05 M potassium chloride solution.

The HOPG sample ($7\times7\times0.6$ mm, NT-MDT) was freshly cleaved with scotch tape prior mounting in the sample holder.

The integral electrochemical methods were performed with an ECi200 potentiostat from Nordic Electrochemistry Aps. A platinum wire (MaTecK, 99.9%, Ø 0.8 mm) was used as counter electrode. As reference electrode freshly prepared reversible hydrogen electrode or Ag/AgCl (Science Line, SI Analytics) were used as reference electrode. For comparability, all potentials have been converted to values referenced to a reversible hydrogen electrode (RHE). The measurements were corrected for ohmic drop measured by the potentiostat after the measurement if stated in the figure.

All EC-STM experiments have been performed with an EC-STM, developed by Wilms, et al.[53] and equipped with an SPM100 electronics (RHK Technology Inc.) for imaging. The electrochemical potential control of the studied surface is enabled through a Picostat potentiostat (Molecular Imaging Inc.). In this work, all mentioned tip and surface potentials are referenced versus the reference electrode. To this purpose, platinum wires (MaTecK, 99.9%, Ø 0.8 mm) were used as both, counter, and pseudo reference electrode, but the potentials were converted to values referenced to a RHE. The Ir/Pt tips were prepared by mechanical cutting or electrochemical etching in KOH/KSCN solution. In order to reduce overlaying faradaic currents, the majority of the tip, except for the apex, was coated with Apiezon wax. The remaining tip area exposed to the electrolyte was controlled prior the experiment by the measurement of the tip leakage current, while being in the electrolyte and not in tunneling condition. Usually tips showed a leakage current below 30 pA. The samples were fixed in a PEEK sample holder and contacted from the backside. STM images were analyzed by the Gwyddion software[54] with a line-by-line linear background subtraction. The apparent height was referenced to the average background height of the terraces and the height

scale calibrated for Au(111) steps (0.24 nm). Line profiles were taken horizontally in the fast scanning direction in order to minimize the effect of drift.

Acknowledgements

The authors would like to thank Dr. Hany El-Sayed and Dr. habil Oliver Schneider for the discussion and valuable comments, which helped to improve this work and Dr. Gustav Wiberg for the support with the potentiostatic measurements. F.E. and N.B. acknowledge support by the German Research Council (DFG, through project ES 349/4-1 and TUM International Graduate School of Science and Engineering, IGSSE). A.D.C. thanks the financial support by the Alexander von Humboldt Foundation. U.K. thanks the German Research Council (DFG, KO-2288/26-1), Jacobs University, and CMST COST Action CM1203 (PoCheMoN) for support. T.M. acknowledges China Scholarship Council (CSC) for a doctoral fellowship. Open access funding enabled and organized by Projekt DEAL.

Conflict of Interest

The authors declare no conflict of interest.

Keywords: electrodeposition · electrochemical scanning tunneling microscopy · cluster · polyoxometalates · palladium

[1] T. Naito, T. Shinagawa, T. Nishimoto, K. Takanabe, *ChemSusChem* **2020**, *13*, 5921–5933.
[2] B. R. Cuenya, *Thin Solid Films* **2010**, *518*, 3127–3150.
[3] S. Kunz, K. Hartl, M. Nesselberger, F. F. Schweinberger, G. Kwon, M. Hanzlik, K. J. Mayrhofer, U. Heiz, M. Arenz, *Phys. Chem. Chem. Phys.* **2010**, *12*, 10288–10291.
[4] M. Nesselberger, M. Roefzaad, R. F. Hamou, P. U. Biedermann, F. F. Schweinberger, S. Kunz, K. Schloegl, G. K. Wiberg, S. Ashton, U. Heiz, K. J. Mayrhofer, M. Arenz, *Nat. Mater.* **2013**, *12*, 919–924.
[5] G. Kwon, G. A. Ferguson, C. J. Heard, E. C. Tyo, C. Yin, J. DeBartolo, S. Seifert, R. E. Winans, A. J. Kropf, J. Greeley, R. L. Johnston, L. A. Curtiss, M. J. Pellin, S. Vajda, *ACS Nano* **2013**, *7*, 5808–5817.
[6] A. von Weber, S. L. Anderson, *Acc. Chem. Res.* **2016**, *49*, 2632–2639.
[7] T. Imaoka, Y. Akanuma, N. Haruta, S. Tsuchiya, K. Ishihara, T. Okayasu, W. J. Chun, M. Takahashi, K. Yamamoto, *Nat. Commun.* **2017**, *8*, 688.
[8] W. W. Ayass, J. F. Minambres, P. Yang, T. Ma, Z. Lin, R. Meyer, H. Jaensch, A. J. Bons, U. Kortz, *Inorg. Chem.* **2019**, *58*, 5576–5582.
[9] S. Bhattacharya, W. W. Ayass, D. H. Taffa, A. Schneemann, A. L. Semrau, S. Wannapaiboon, P. J. Altmann, A. Pothig, T. Nisar, T. Balster, N. C. Burtch, V. Wagner, R. A. Fischer, M. Wark, U. Kortz, *J. Am. Chem. Soc.* **2019**, *141*, 3385–3389.
[10] S. Bhattacharya, W. W. Ayass, D. H. Taffa, T. Nisar, T. Balster, A. Hartwig, V. Wagner, M. Wark, U. Kortz, *Inorg. Chem.* **2020**, *59*, 10512–10521.
[11] V. Kogan, Z. Aizenshtat, R. Popovitz-Biro, R. Neumann, *Org. Lett.* **2002**, *4*, 3529–3532.
[12] P. Losch, W. X. Huang, E. D. Goodman, C. J. Wrasman, A. Holm, A. R. Riscoe, J. A. Schwalbe, M. Cargnello, *Nano Today* **2019**, *24*, 15–47.
[13] T. Imaoka, H. Kitazawa, W. J. Chun, S. Omura, K. Albrecht, K. Yamamoto, *J. Am. Chem. Soc.* **2013**, *135*, 13089–13095.
[14] L. R. Merte, F. Behafarid, D. J. Miller, D. Friebel, S. Cho, F. Mbuga, D. Sokaras, R. Alonso-Mori, T. C. Weng, D. Nordlund, A. Nilsson, B. Roldan Cuenya, *ACS Catal.* **2012**, *2*, 2371–2376.
[15] X. K. Wan, H. B. Wu, B. Y. Guan, D. Luan, X. W. D. Lou, *Adv. Mater.* **2020**, *32*, e1901349.
[16] P. Yang, U. Kortz, *Acc. Chem. Res.* **2018**, *51*, 1599–1608.
[17] P. Yang, Y. Xiang, Z. Lin, B. S. Bassil, J. Cao, L. Fan, Y. Fan, M. X. Li, P. Jimenez-Lozano, J. J. Carbo, J. M. Poblet, U. Kortz, *Angew. Chem. Int. Ed.* **2014**, *53*, 11974–11978; *Angew. Chem.* **2014**, *126*, 12168–12172.
[18] L. H. Bi, M. Reicke, U. Kortz, B. Keita, L. Nadjo, R. J. Clark, *Inorg. Chem.* **2004**, *43*, 3915–3920.
[19] E. V. Chubarova, M. H. Dickman, B. Keita, L. Nadjo, F. Miserque, M. Mifsud, I. W. Arends, U. Kortz, *Angew. Chem. Int. Ed.* **2008**, *47*, 9542–9546; *Angew. Chem.* **2008**, *120*, 9685–9689.
[20] N. V. Izarova, R. N. Biboum, B. Keita, M. Mifsud, I. W. Arends, G. B. Jameson, U. Kortz, *Dalton Trans.* **2009**, 9385–9387.
[21] M. Barsukova, N. V. Izarova, R. N. Biboum, B. Keita, L. Nadjo, V. Ramachandran, N. S. Dalal, N. S. Antonova, J. J. Carbo, J. M. Poblet, U. Kortz, *Chem. Eur. J.* **2010**, *16*, 9076–9085.
[22] J. Friedl, R. Al-Oweini, M. Herpich, B. Keita, U. Kortz, U. Stimming, *Electrochim. Acta* **2014**, *141*, 357–366.
[23] M. Ammam, B. Keita, L. Nadjo, I.-M. Mbomekalle, M. D. Ritorto, T. M. Anderson, W. A. Neiwert, C. L. Hill, J. Fransaer, *Electroanalysis* **2011**, *23*, 1427–1434.
[24] G. E. Engelmann, J. C. Ziegler, D. M. Kolb, *J. Electrochem. Soc.* **1998**, *145*, L33-L35.
[25] J. Meier, J. Schiotz, P. Liu, J. K. Norskov, U. Stimming, *Chem. Phys. Lett.* **2004**, *390*, 440–444.
[26] S. Pandelov, U. Stimming, *Electrochim. Acta* **2007**, *52*, 5548–5555.
[27] S. Takakusagi, K. Kitamura, K. Uosaki, *Electrochim. Acta* **2009**, *54*, 5137–5141.
[28] A. Cuesta, M. Kleinert, D. M. Kolb, *Phys. Chem. Chem. Phys.* **2000**, *2*, 5684–5690.
[29] J. H. K. Pfisterer, Y. Liang, O. Schneider, A. S. Bandarenka, *Nature* **2017**, *549*, 74–77.
[30] M. Barsukova-Stuckart, N. V. Izarova, R. A. Barrett, Z. Wang, J. van Tol, H. W. Kroto, N. S. Dalal, P. Jimenez-Lozano, J. J. Carbo, J. M. Poblet, M. S. von Gernler, T. Drewello, P. de Oliveira, B. Keita, U. Kortz, *Inorg. Chem.* **2012**, *51*, 13214–13228.
[31] J. Sherwood, J. H. Clark, I. J. S. Fairlamb, J. M. Slattery, *Green Chem.* **2019**, *21*, 2164–2213.
[32] A. C. Chen, J. Lipkowski, *J. Phys. Chem. B* **1999**, *103*, 682–691.
[33] C. Köntje, L. A. Kibler, D. M. Kolb, *Electrochim. Acta* **2009**, *54*, 3830–3834.
[34] L. A. Kibler, A. M. El-Aziz, D. M. Kolb, *J. Mol. Catal. A* **2003**, *199*, 57–63.
[35] J. Tang, M. Petri, L. A. Kibler, D. M. Kolb, *Electrochim. Acta* **2005**, *51*, 125–132.
[36] M. E. Björketun, G. S. Karlberg, J. Rossmeisl, I. Chorkendorff, H. Wolfschmidt, U. Stimming, J. K. Nørskov, *Phys. Rev. B* **2011**, *84*.
[37] K. Obata, L. Stegenburga, K. Takanabe, *J. Phys. Chem. C* **2019**, *123*, 21554–21563.
[38] W. B. Ju, T. Brulle, M. Favaro, L. Perini, C. Durante, O. Schneider, U. Stimming, *ChemElectroChem* **2015**, *2*, 547–558.
[39] V. C. Diculescu, A. M. Chiorcea-Paquim, O. Corduneanu, A. M. Oliveira-Brett, *J. Solid State Electrochem.* **2007**, *11*, 887–898.
[40] L. A. Kibler, *ChemPhysChem* **2006**, *7*, 985–991.
[41] B. Hammer, J. K. Norskov, *Surf. Sci.* **1995**, *343*, 211–220.
[42] H. Naohara, S. Ye, K. Uosaki, *J. Phys. Chem. B* **1998**, *102*, 4366–4373.
[43] H. Naohara, S. Ye, K. Uosaki, *Colloids Surf. A* **1999**, *154*, 201–208.
[44] B. Wang, B. Yoon, M. Konig, Y. Fukamori, F. Esch, U. Heiz, U. Landman, *Nano Lett.* **2012**, *12*, 5907–5912.
[45] S. Bhattacharya, U. Basu, M. Haouas, P. Su, M. F. Espenship, F. Wang, A. Sole-Daura, D. H. Taffa, M. Wark, J. M. Poblet, J. Laskin, E. Cadot, U. Kortz, *Angew. Chem. Int. Ed.* **2021**, *60*, 3632–3639.
[46] Z. Su, J. Leitch, J. Lipkowski, *Z. Phys. Chem.* **2012**, *226*, 995–1009.
[47] R. Villanneau, A. Roucoux, P. Beaunier, D. Brouri, A. Proust, *RSC Adv.* **2014**, *4*, 26491–26498.
[48] J. Yang, C. M. Andrei, Y. Chan, B. L. Mehdi, N. D. Browning, G. A. Botton, L. Soleymani, *Langmuir* **2019**, *35*, 862–869.
[49] C. Wu, F. Xu, M. R. Castell, S. C. Tsang, *Chem. Commun. (Camb.)* **2014**, *50*, 1198–1201.
[50] C. J. Baddeley, R. M. Ormerod, A. W. Stephenson, R. M. Lambert, *J. Phys. Chem.* **1995**, *99*, 5146–5151.
[51] J. A. Mwanda, A. Cuesta, *Electrochim. Acta* **2018**, *292*, 419–424.
[52] M. Baldauf, D. M. Kolb, *Electrochim. Acta* **1993**, *38*, 2145–2153.
[53] M. Wilms, M. Kruft, G. Bermes, K. Wandelt, *Rev. Sci. Instrum.* **1999**, *70*, 3641–3650.
[54] D. Nečas, P. Klapetek, *Open Phys.* **2012**, *10*, 181–188.

Manuscript received: January 28, 2021
Revised manuscript received: February 17, 2021
Accepted manuscript online: February 17, 2021

ChemElectroChem

Supporting Information

Towards Size-Controlled Deposition of Palladium Nanoparticles from Polyoxometalate Precursors: An Electrochemical Scanning Tunneling Microscopy Study

Nicolas Bock[+], Astrid De Clercq[+], Lukas Seidl, Tim Kratky, Tian Ma, Sebastian Günther, Ulrich Kortz, Ueli Heiz, and Friedrich Esch*

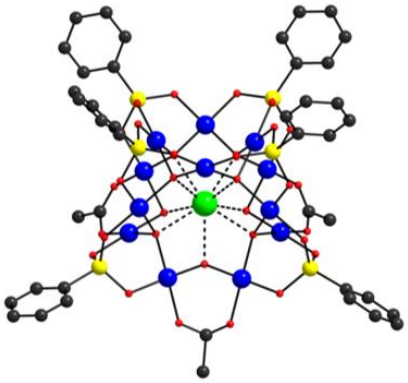

Figure S1: Molecular structure of $[SrPd_{12}O_6(OH)_3(PhAsO_3)_6(OAc)_3]^{4-}$.

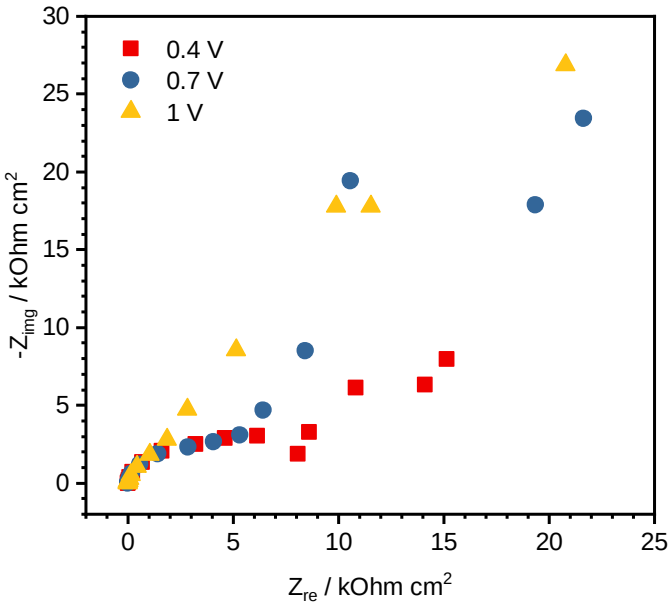

*Figure S2: Impedance spectroscopy of a Au(111) surface in phosphate buffer at different applied potentials (DC voltages indicated vs RHE). Measurement parameters: 10 mV amplitude and frequency range of 0.1 mHz to 10 kHz. The rising imaginary impedance at higher applied voltages, observed in the Nyquist-plot, indicates the increased capacitance due to phosphate surface adsorption that sets in at potentials above 0.4 V vs RHE. This might explain the high overpotential needed for **$SrPd_{12}$** reduction, as phosphate desorption is required to enable electron transfer between surface and **$SrPd_{12}$**.*

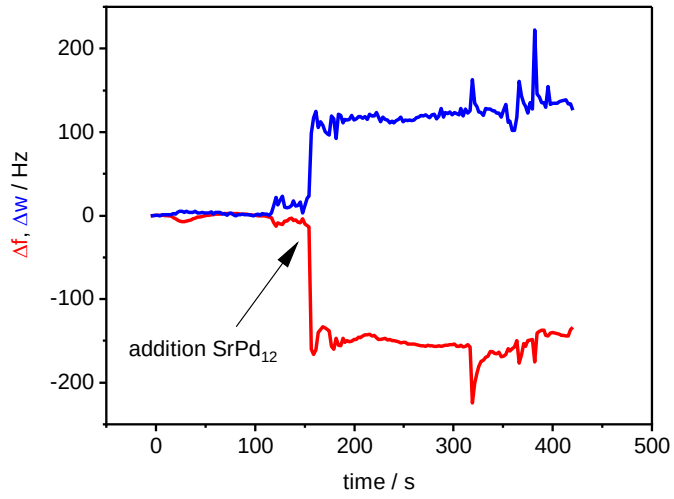

Figure S3: Three-electrode quartz crystal microbalance (EQCM) measurement of a polycrystalline Au sample on a quartz resonator in phosphate buffer at 0.4 V vs RHE indicating the effect of ***SrPd₁₂*** *addition to the argon-purged solution (after 150 s, 0.2 g/L* ***SrPd₁₂****). The EQCM measurements were carried out by measuring the quartz crystal admittance in the vicinity of the its resonance frequency using a network analyzer. From a fit of the real part of the admittance with a Lorentz function, the resonance frequency f (peak position) and the damping w (full peak width at half maximum) were extracted as a function of time. One observes that the damping (Δw=w(t)-w(t=0)) increases and the resonance frequency (Δf=f(t)-f(t=0)) lowers. As the absolute change in Δf exceeds slightly the damping change, one can conclude that both, viscosity of the electrolyte close to the surface and mass loading of the double layer increase. This points to a* ***SrPd₁₂*** *incorporation into the double layer, in agreement with the CV capacitance increase after the* ***SrPd₁₂*** *addition, shown in Figure S8.*

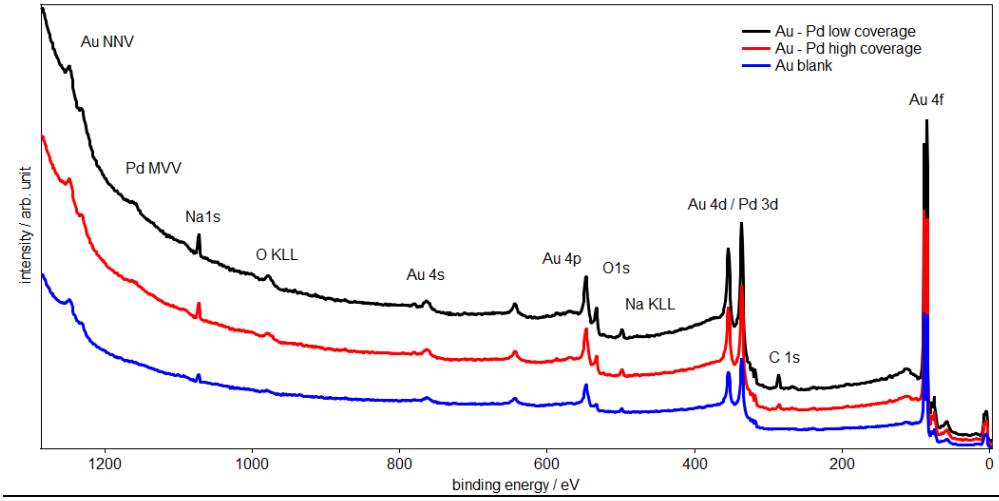

Figure S4: Stacked x-ray photoelectron spectroscopy overviews of a Pd-covered Au(111) working electrode after rinsing with ultrapure water and transfer to UHV conditions. The Pd particles have been deposited by applying a potential of 0.2 V vs RHE for 10 min (low coverage), resp. 30 min (high coverage) in a ***SrPd₁₂*** *(c=6 nmol/L) containing 0.5 M phosphate buffer electrolyte. In the resulting XPS spectra, only Au, Pd, and adventitious carbon are detected, indicating that the ligands are stripped off during deposition and not co-deposited. The assigned peaks proof the presence of Au and Pd as well*

as small impurities (adventitious C, Na and O) indicating that the ligands of $SrPd_{12}$ are stripped off during deposition and not co-deposited. XPS parameters: pass energy: 100 eV, x-ray energy: 1486.7 eV.

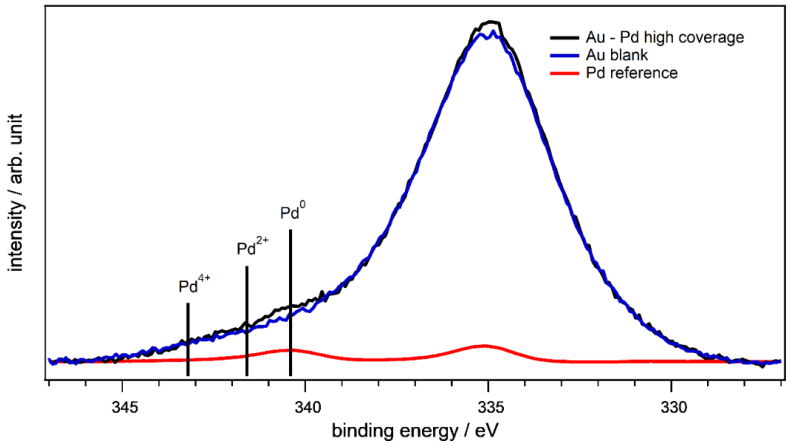

Figure S5: Detailed Au 4d5/2 spectra evidence the presence of a Pd 3d1/2 shoulder. This shoulder indicates the presence of metallic Pd. For comparison, arrows pinpoint the Pd 3d1/2 energy position of Pd^{2+} and Pd^{4+} species, respectively. The deconvolution of the overlapping Au 4d5/2 and Pd 3d core level peaks can be performed but does not deliver precise peak intensity values. Instead, the Pd MVV Auger electron yield can be used to quantify the amount of deposited Pd particles (see Figure S6).

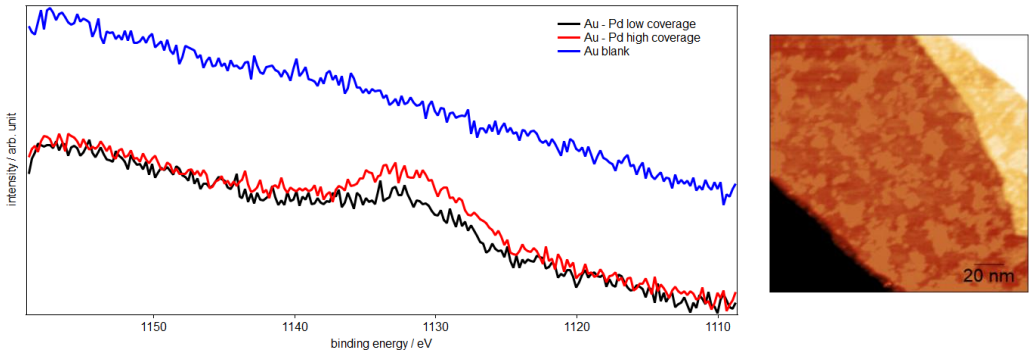

Figure S6: Detail of the Pd-specific MVV-Auger signal in the photoemission spectra of Figure S4. In a separate experiment, photoelectron spectra were taken from a reference Pd foil and the acquired Pd MVV Auger electron emission yield is about twice as intense with respect to the Pd 3d core level peak intensity. Dividing the signal intensities by the inelastic mean free paths (8.4 Å for Pd MVV and 20.2 Å for Pd 3d) leads to the expected relative peak intensities of a pure surface species. In this case, the Auger peak is about 5 times larger than Pd 3d peak intensity. The Pd MVV intensity measured on the Pd-loaded Au electrode can now be related to the measured Au 4f peak intensity. Taking the Pd 3d and Au 4f cross sections into account and using the inelastic mean free path of the ejected Au 4f electrons (16.5 Å) leads to a Pd surface coverage of 32±5 %. This number agrees well with the estimated surface area fraction of 40±20 % covered by Pd particles that is observed by STM (170x170 nm^2) after the deposition process prior to XPS characterization. The combination of XPS and STM data proves that the particles on top of the Au electrode consist of Pd.

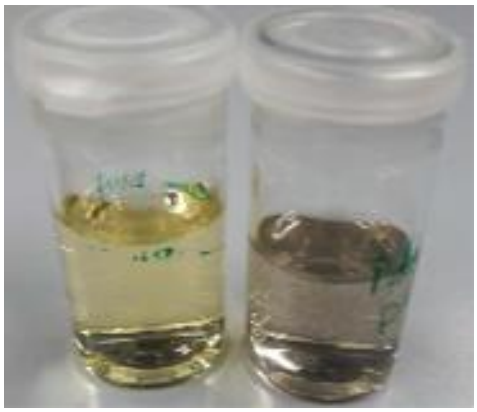

*Figure S7: 5 µM **SrPd$_{12}$** 0.5 M H_3PO_4/NaOH solution before (left) and after purging with H_2 gas (right): In less than 1 min, the solution turns black and flakes form, that can easily be recognized by eye.*

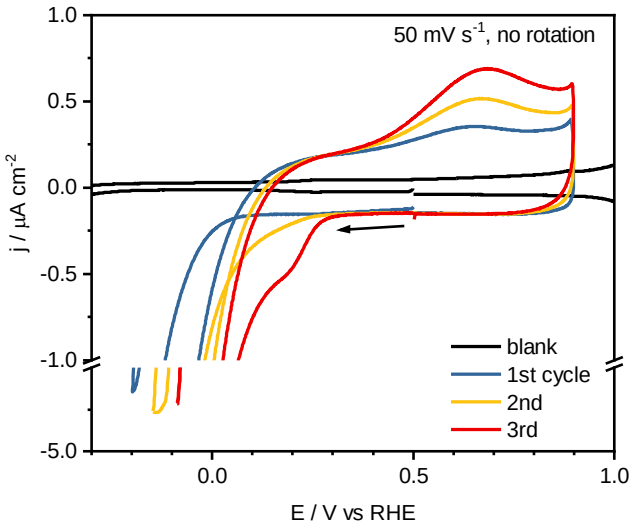

*Figure S8: Cyclic voltammogram of a highly ordered pyrolytic graphite surface (HOPG, ZYA) in 0.5 µM **SrPd$_{12}$** containing 0.05 M $HClO_4$ electrolyte. The strong increase of the double layer capacitance compared to the blank measurement indicates the presence of surface-near **SrPd$_{12}$** ions. The reduction behavior is seen to be strongly influenced by the Pd deposition due to cycling. From cycle to cycle, deposited Pd^0 continuously shifts the potential for hydrogen evolution towards more positive potentials. This explains the cross-over in the reduction current traces, as freshly deposited Pd further enhances the HER. The fact that the HER starts at potentials positive to 0 V RHE is caused by the absence of molecular H_2 in the electrolyte. In the third cycle, a distinct hydrogen adsorption peak at 0.2 V vs RHE is observed.*

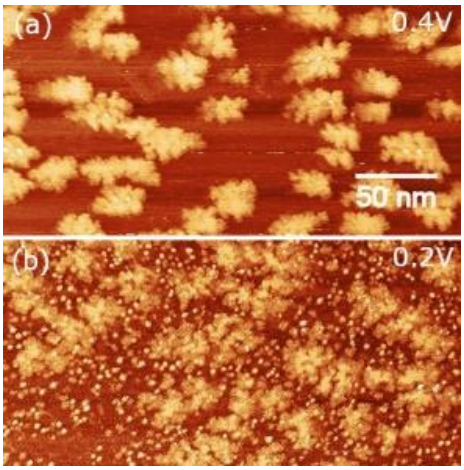

Figure S9: In situ EC-STM image of the Pd particle morphology obtained after another type of pretreatment where hydrogen species form. Here, the Au(111) surface was exposed to 6x500 ms potential steps to -0.1 V vs RHE (starting from 0.4 V vs RHE) in 0.1 M phosphate buffer, prior to the addition of ***SrPd$_{12}$*** *(amount corresponding to 0.3 equivalent Pd-monolayers). (a) After POP-addition, still at 0.4 V vs RHE, flower-like structures form instantaneously in a process, that probably is limited by hydrogen availability. (b) As the surface is set to 0.2 V vs RHE, remaining* ***SrPd$_{12}$*** *in solution can still be deposited in form of small particles. Imaging conditions: U_b=-100 mV, I_t=311 pA.*

4. On-Surface Polymerization of Triazido-Heptazine towards Carbon Nitride Films

Contributor Roles

Nicolas Bock: Investigation, Visualization, Writing
Matthias Krinninger: Investigation
Astrid De Clercq: Investigation
Sebastian Kaiser: Investigation
Peter Feulner: Resources
Francesco Allegretti: Resources
Klaus Köhler: Resources
Shengyang Guan: Investigation
Alexander Pöthig: Supervision
Ueli Heiz: Funding acquisition, Resources
Friedrich Esch: Conceptualization, Supervision, Funding acquisition

Carbon nitride materials CN_x have received sustained interest ever since first being mentioned by Liebig [74] in 1834, especially since semiconductive nitrogen-rich carbon nitride networks have shown huge potential for (photo)catalysis, e. g. water splitting or carbon dioxide photoreduction.[75,76] Besides their direct application for metal-free catalysis, the diverse nanostructures allow to tune N-rich binding pores for the stabilization of supported metal catalysts. Recently, a carbon nitride network was used to incorporate single Pd atoms for C–C coupling reactions.[77] The ability to bind catalyst particles from single atoms to entire clusters in an ordered way,[78] would steer size-dependent reactivities with high control. This plays a crucial role especially for the non-scalable size regime, where atom-by-atom size dependencies have shown strong support influence on reactivity[79] and ripening[80]. While nitrogen-bridged triazine (C_3N_3)- and heptazine (C_6N_7)-based 2D-CN_x structures are the most studied, the structural variety of 2D-CN_x materials is manifold and opens up the possibility to draft catalyst supports with multiple binding sites, that could even combine photocatalysis on the carbon nitride with electrocatalysis on supported particles.

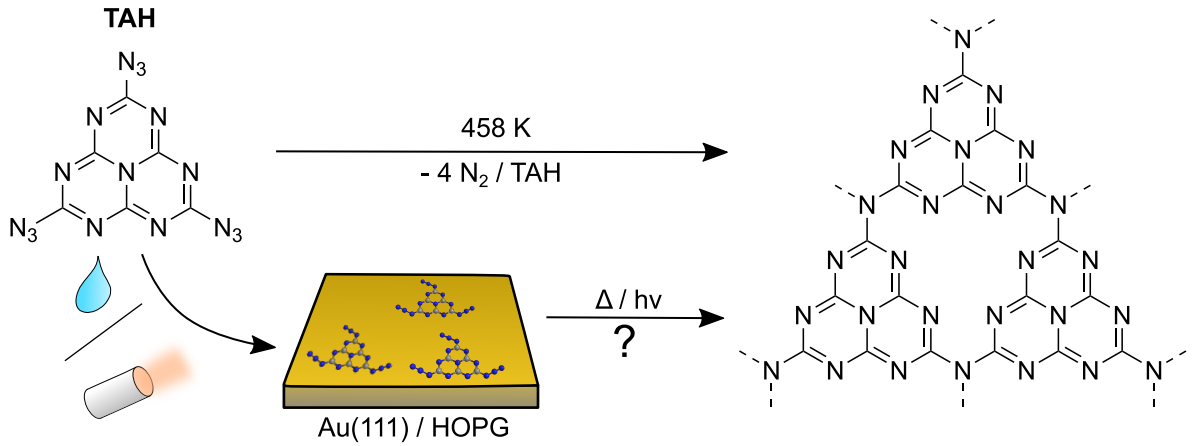

Figure 4.1. Polymerization of TAH precursor molecule with nitrogen gas release to carbon nitride network (dashed bonds indicate further heptazine units). Suggested novel on-surface synthesis on gold and graphite surfaces after deposition of TAH molecules via liquid or vacuum deposition methods.

Despite intensive research with laser-electric discharge methods[81], chemical vapor deposition[82], electrodeposition[83], spray deposition[84], liquid-gas interface separation[85], and exfoliation[86], a formation of structured CN_x layers, often called graphitic carbon nitride (g-C_3N_4) remains experimentally challenging. Especially the formation of single atomic layers is still hardly accessible with current methods.[87]

In this work we present our attempts to form single graphitic carbon nitride layers of bridged *s*-heptazine (C_6N_7) units on Au(111) and highly oriented pyrolytic graphite (HOPG) surfaces (see Figure 4.1). Such well-defined surfaces were used extensively before to steer classical organic reactions such as Ullmann coupling[88] or N=N bond coupling from aryl azides[89] and enabled the formation of a variety of structural motifs by on-surface polymerization. A previous report by Gillan [90] on the carbon nitride formation demonstrates, that the hydrogen content in the formed network increases its corrugation as –NH– groups allow a rotation and break the in-plane symmetry. Therefore, we opted for a hydrogen-free 2,5,8-triazido-*s*-heptazine (TAH) as a precursor for the on-surface polymerization. The synthesis from melamine via melem and 2,5,8-trihydrazino-*s*-heptazine to the final product TAH was performed and described by Krinninger [91]. The three $-N_3$ azide groups are very reactive and known to react both thermally at 458 K[92,93] and light-induced[94,95]. The C_6N_7-core of TAH ($C_6N_7(N_3)_3$) is completely planar and while the azide group is slightly bent, it is still centered in the molecular plane of the C_6N_7 core.[92] These precursors form closed packed, layered crystals that indicate the feasibility of co-planar adsorption and flat 2D coupling along the surface.

4.1. Vapor and Liquid Deposition of TAH Precursor

Crucial requirement for an extended molecular network is a well-ordered initial precursor superstructure. This is especially of importance as the polymerization by azide decomposition of TAH is known to be highly exothermic, releasing energy-rich nitrogen molecules. This tends to counteract the formation of a monoatomic layer.[93] In order to deposit well-defined single layers of TAH precursor molecules, we used both vacuum evaporation and liquid deposition techniques. The starting compound TAH, with the three reactive azide groups is known to react above temperatures of 458 K.[92] An evaporation is therefore only possible, if the vapor pressure below this reaction temperature is high enough and if the molecule remains intact during this evaporation. The molecule flux needs to be high enough to obtain a film deposition within minutes. Miller, Holst, and Gillan [93] showed by thermogravimetric-differential analysis (see Figure 4.2) that the heated TAH powder looses weight already above 25 °C (298 K). As this method is chemically unspecific, it is unclear if the TAH is evaporated intactly or whether part of the reactive azide groups are already decomposed. In order to rule out a decomposition of the TAH molecule, a further mass analysis of the gas products is needed. At 190 °C (463 K), the weight drops drastically, which is attributed to the actual TAH polymerization process and release of gaseous nitrogen. Above this reaction temperature the weight gradually decreases, as the carbon nitride thermally decomposes or restructures.[93]

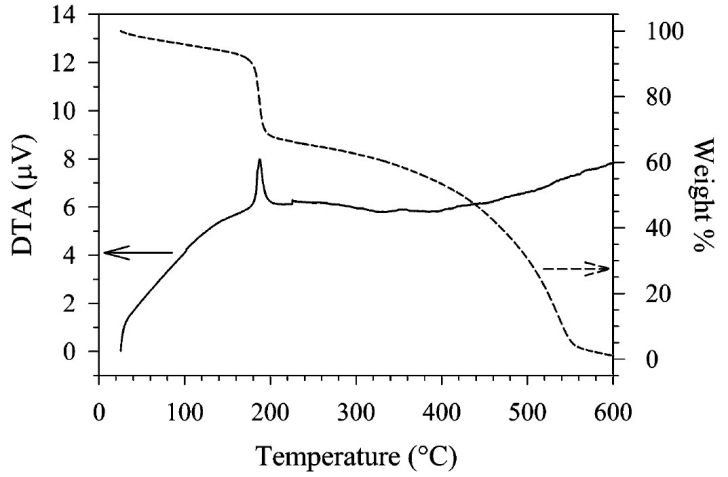

Figure 4.2. Thermogravimetric-differential analysis shows a weight loss above 25 °C (298 K). The sudden decrease at 190 °C (463 K) is attributed to the gas release during the polymerization. At higher temperatures the formed carbon nitride is decomposed. Reprinted with permission from D. R. Miller, J. R. Holst, E. G. Gillan, *Inorganic Chemistry* **2007**, *46*, 2767–2774. Copyright 2007 American Chemical Society.

Intact Evaporation

In order to perform a mass analysis of the evaporated products and to explore the evaporability of the precursor, a TAH-filled tantalum crucible was placed in front of a mass spectrometer and heated in vacuum conditions. Figure 4.3 shows the TAH molecule and its fragments, detected during a temperature ramp from room temperature to 600 K (0.05 K/s). Throughout the heating series, traces of H_2O, CO, and CO_2 were detected, which resulted from the residual gases in the vacuum system ($p < 5{\cdot}10^{-8}$ mbar). At temperatures above 415 K, the TAH molecule ($C_6N_7(N_3)_3$: 296 amu), as well as fragments, including N_2 (identified by mass 14 and 28 amu) were detected. Three distinct spikes are visible above 460 K throughout all TAH fragment masses, which we assign to explosion-like desorption of TAH molecules at hot spots. The resistance-heated tantalum cup filled with TAH might develop small temperature gradients throughout the powder, leading to possible molecule ejection or autocatalytic explosions at hot spots.

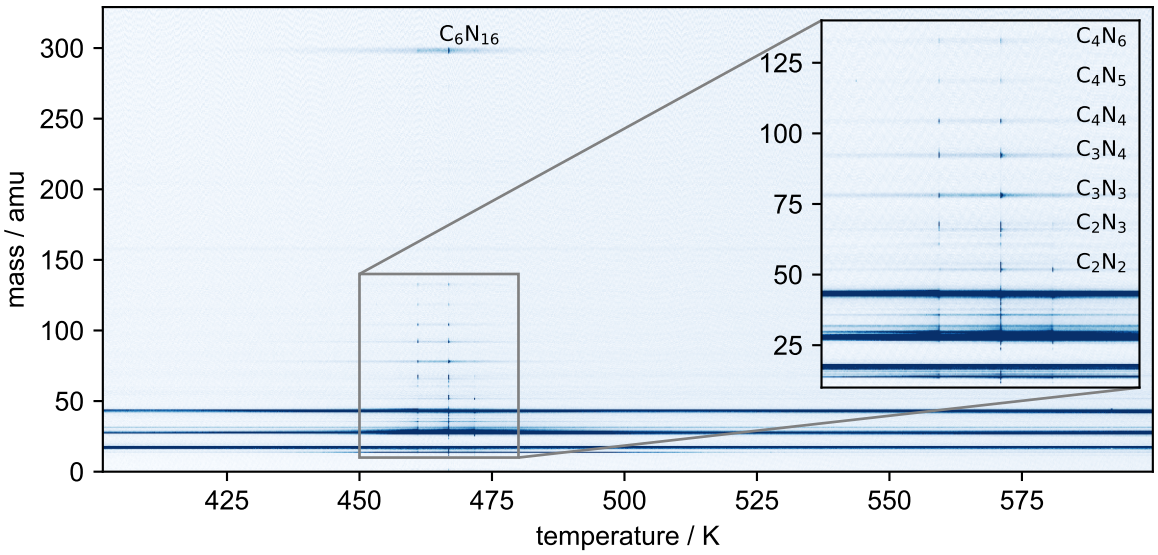

Figure 4.3. Vapor products and their fragments detected in a mass spectrometer, while heating to 600 K (temperature ramp 0.05 K/s). Throughout all temperatures H_2O, CO_2, and CO were detected. The TAH mass at 296 amu and its fragments were detected above temperatures of 415 K. Three signal spikes are found across all detected molecule masses, which are attributed to ejection of intact TAH.

The detected masses at 470 K are shown in a semi-logarithmic plot in Figure 4.4. At this temperature the highest TAH intensities were detected. Surprisingly, no pure heptazine core C_6N_7 signals (mass 170 amu) were found in the fragmentation pattern. However, the C_3N_3 triazine element and also C_3N_4 with additional nitrogen from the azide group were found. If the heptazine unit was fragmented into one triazine, a ring

closure of the remaining molecule is expected. This would also result in the mass of a C_3N_4 unit. The masses that could be detected were assigned to the following chemical compositions: C_4N_6, C_4N_5, C_4N_4, C_2N_3, and C_2N_2. However, their structural motifs remain unclear. Importantly, the unique fragmentation pattern of the TAH molecule allows the clear identification of the precursor molecule its distinction from melamine, which was the starting compound in the TAH synthesis. Furthermore, it proves the intact evaporation of TAH molecule before thermal decomposition sets in.

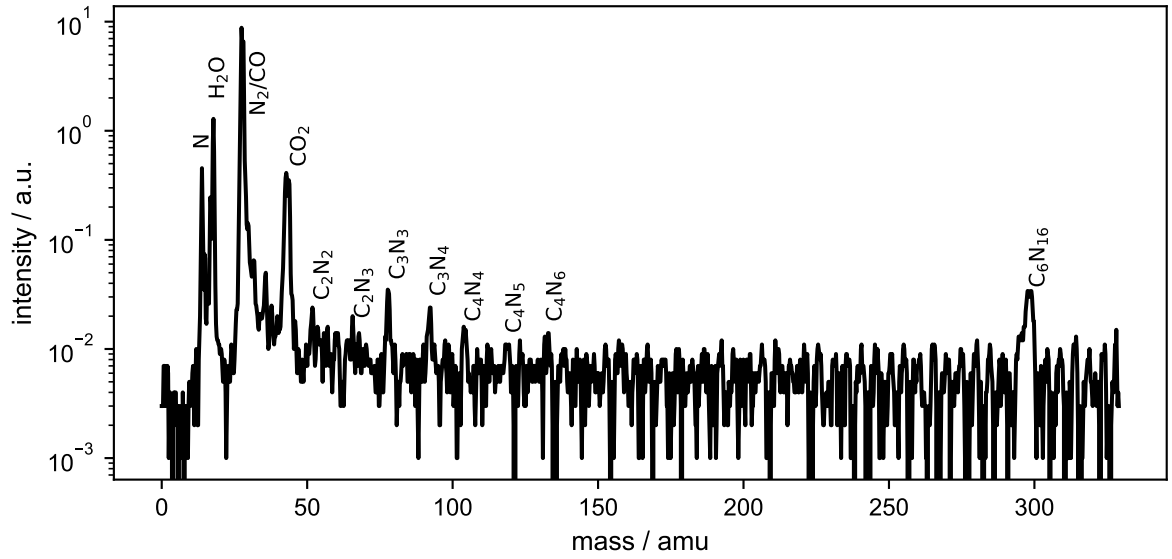

Figure 4.4. The mass spectrum of the gas products of TAH powder at 470 K shows the TAH molecule, its fragments, and the residual chamber gas with H_2O, CO, and CO_2.

In order to study the temperature window where TAH can be evaporated intactly, the TAH and nitrogen mass traces are plotted in Figure 4.5a. As the mass 28 amu could also result from residual CO in the vacuum system, the analysis of the N_2 mass trace was carried out with the mass 14 amu signal. The detected nitrogen results both from the fragmentation of the TAH molecule and the nitrogen-releasing polymerization reaction itself. This explains the presence of the same signal spikes in both mass traces, which originated from the already mentioned ejection of TAH molecules. In order to disentangle the two contributions, we fitted the TAH mass baseline to match the one from mass 14 amu (see Figure 4.5b). Simultaneously, the nitrogen and TAH signal started to increase at 415 K. Until the temperature of 445 K, the nitrogen signal matches well the mass trace of the TAH molecule, which implies that the nitrogen originates only from the fragmented evaporated TAH. This late onset of evaporation compared to the report by Miller, Holst, and Gillan [93] might

be explained by a reduced sensitivity of our experimental setup. Above 450 K the slope of nitrogen exceeds the one of TAH significantly, which suggests the onset of the polymerization reaction. This onset temperature is in good agreement with the literature-known reaction temperature of 458 K.[92] Therefore, the temperature range from 415 to 445 K offers us the opportunity to evaporate the intact TAH molecules, without triggering the reaction already in the powder crucible. This is especially important for the repeated use of the molecular evaporator for surface preparation under vacuum conditions.

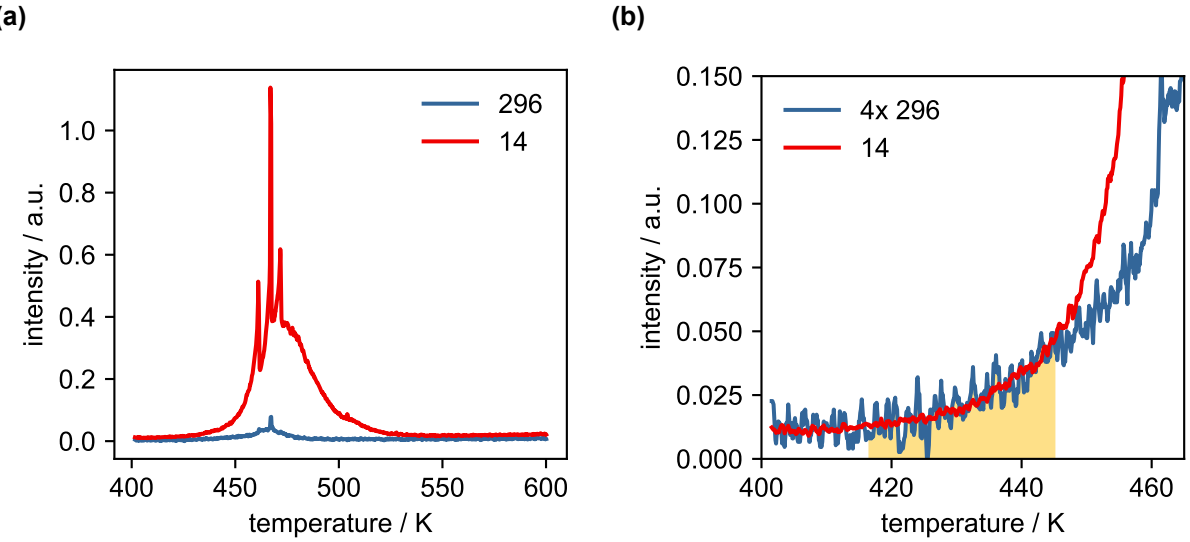

Figure 4.5. **(a)** The mass trace of TAH (■ 296 amu) and nitrogen (■ 14 amu) during a heating experiment measured with a mass spectrometer. The spikes are present in both signals and therefore interpreted as molecule ejections (see text for further explanation). The nitrogen signal exceeded at a certain point the TAH slope. At this point the polymerization reaction sets in and additionally nitrogen as a side product is released. The signal decay originates from the full polymerization of all TAH powder in the crucible. **(b)** The TAH signal is fitted to match the nitrogen onset. The ideal evaporation temperature range is highlighted in ■, where TAH is evaporated, but no polymerization occurs.

For the deposition of TAH films in a reasonable time scale, a significant molecular flux is needed in the temperature range below 445 K. We used a quartz microbalance to confirm the evaporation flux and deposition of TAH. The microbalance was placed in a line-of-sight geometry in front of a freshly filled tantalum crucible. The temperature was measured with a type K thermocouple, spot-welded to the tantalum cup. The microbalance working principle is based on the oscillation of a quartz crystal at its resonance frequency. As soon as molecules are deposited on the quartz, the oscillation changes. From the impedance analysis, the negative frequency shift Δf and the broad-

ening of the resonance can be derived. With the Sauerbrey equation the deposited mass Δm can be estimated:[96]

$$\Delta m = -\frac{A \cdot \sqrt{\rho_q \mu_q} \cdot \Delta f}{2 f_0^2} \tag{4.1}$$

Where f_0 is the resonant frequency, A the crystal area, ρ_q the crystal density, and μ_q the crystal shear modulus. With the TAH density of 1.829 g/cm^3,[97] the deposited layer thickness can be derived. Figure 4.6 shows the deposition rate of TAH molecules over time. After reaching the chosen evaporation temperature of 442 K, the molecular flux stabilizes and remains relative constant for longer deposition times. We believe the two prominent sigmoidal spikes to be measurement artifacts. As soon as the temperature dropped below 420 K, the evaporation decreased significantly. The film preparation performed within this temperature range allowed various consecutive depositions in the vacuum setup without refilling the crucible. The deposited amount calculated here is several times higher than the corresponding STM images of thermally polymerized carbon nitride suggest (see Section 4.2.2), however one has to take into account the desorption of precursor molecules upon heating up, prior to the reaction.

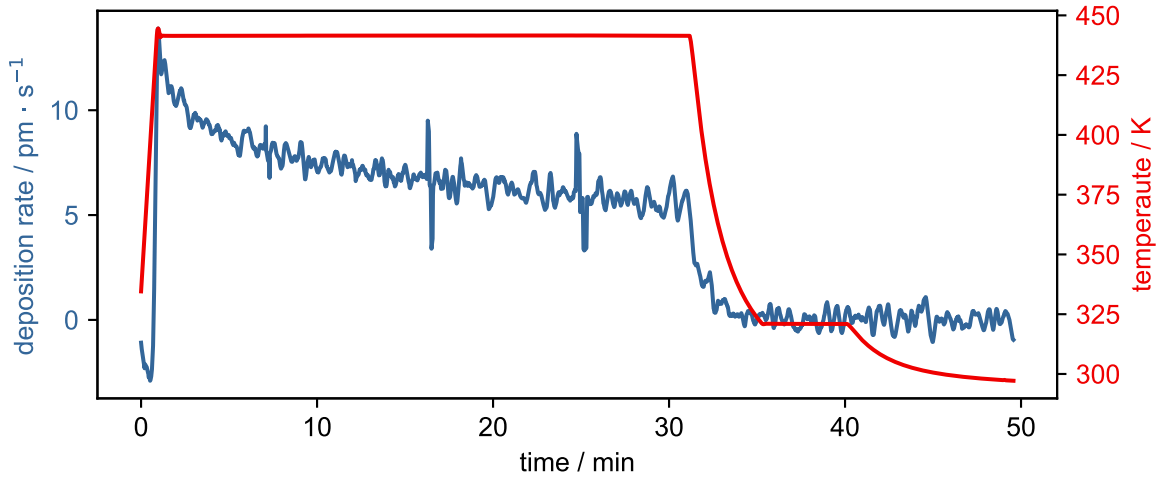

Figure 4.6. The deposition rate of TAH molecules is plotted versus the time as a function of the applied evaporator temperature.

4.1.1. Influence of Molecular Topology on the Adsorption

Only little is known about the adsorption behavior of the TAH molecule on single crystal surfaces. Zheng et al. [94] performed an extensive DFT study of gas-phase heptazines with different substituents. Figure 4.7b shows the extended π-system across

the C_6N_7 core with a similar electronic structure as the triazine. The π-conjugation is enabled through the $2p_z$ orbitals of the carbon and nitrogen atoms. Inline with the heptazine structure the intrinsic element-specific electronegativity, the positive carbon charge increases when inserting the atom into the heptazine structure, while the negative nitrogen charge is lowered even further. Our precursor however, is a heptazine substituted with three azide $-N_3$ groups. Here, the in-plane azide groups not only change the molecule symmetry from D_{3h} to C_{3h}, but also alter the electronic structure of the C_6N_7 core. The electron donating azide group weakens the adjacent N–C bonds in the heptazine cycle. However the stabilization due to the π-system and the strong donor-acceptor interaction between the lone electron pair of the $-N_3$ groups and the π^*-orbitals of the C_6N_7 core are strong enough to compensate this charge transfer. The highest occupied molecular orbital (HOMO) decreases in energy when the azide is added. The lowest unoccupied molecular orbital (LUMO) increases in energy. This results in a overall HOMO-LUMO gap of 4.14 eV.[94] The theoretical band gap values of the yellow-colored TAH powder were confirmed experimentally by UV-Vis spectroscopy, revealing two absorbance peaks at 275 and 295 nm (4.51 resp. 4.2 eV) attributed to the $\pi \rightarrow \pi^*$ and $n \rightarrow \pi^*$ transitions.[98] Figure 4.7c – d shows the HOMO and LUMO representation of the TAH molecule. The heptazine core shows an alternating orbital polarity, as known for alternant aromatic hydrocarbon systems according to the Hückel rule.[99]

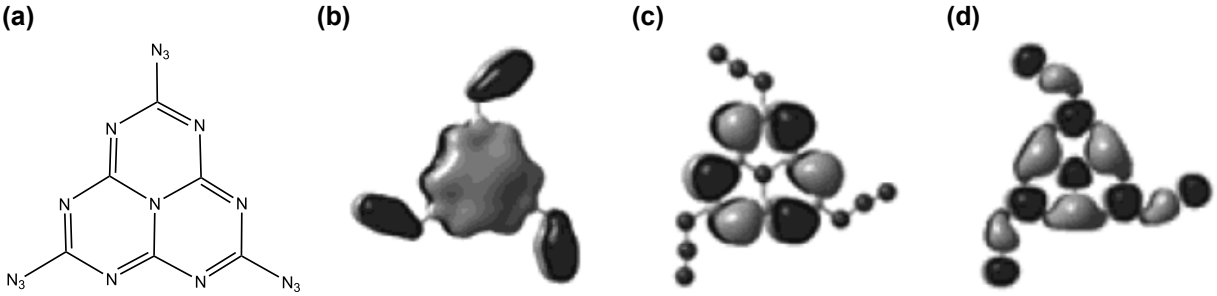

Figure 4.7. **(a)** TAH molecule structure with heptazine C_6N_7 core and three $-N_3$ azide groups. **(b)** π-system shows a delocalization throughout the heptazine. **(c – d)** The HOMO and LUMO model of the TAH molecule. **(b – d)** Reprinted adapted with permission from W. Zheng et al., *The Journal of Physical Chemistry A* **2004**, *108*, 97–106. Copyright 2004 American Chemical Society.

The extended π-system throughout the C_6N_7 core of TAH could promise a strong interaction with extended surfaces: It has been shown that the electronic orbital structure of similar hydrocarbon determines whether a physisorption or chemisorption character dominates the binding. Especially nonalternant aromatic systems have shown huge differences on specific surfaces. Chemisorption was observed for a non-

alternant aromatic system, like azulene on a copper surface, while physisorption occurred on a silver surface.[100] The isomer and alternant napthalene instead showed a physisorption character on both surfaces.[101] Density functional theory simulations (DFT) predict a physisorption on Au(111) for a heptazine molecule with three diacetylene rests instead of the azide groups.[102] In order to understand the surface-specific behavior, we investigated the TAH adsorption by means of x-ray photoelectron spectroscopy (XPS), temperature programmed desorption (TPD) and scanning tunneling microscopy (STM) on two surfaces: graphite and Au(111). Gold with high valence electron density high is expected to interact more stongly.

4.1.2. Deposition on Au(111)

In the following first experiments on the deposition of TAH, the molecule has been vapor-deposited on Au(111)/glass support for 30 min, at 440 K evaporator temperature. The gold film on the glass support had been annealed in air prior to the experiment to yield a Au(111) surface termination (see section 2.4.1 for further preparation details). The sample was then transferred through air to the XPS setup. Figure 4.8 shows the resulting XPS spectra. Besides gold, carbon, and nitrogen, also an oxygen 1s (O1s) signal at 531.4 eV was detected. This indicates an adventitious carbon impurity, which was introduced during the atmospheric sample transfer.[103]

All measured spectra are shifted to match the a reference value 84 eV of the $Au4f_{7/2}$ signal.[104] Transition metals are known for their asymmetric peaks shapes and therefore the one gold contribution is fitted with the Doniach-Sunjic function. All the other signals are fitted with Voigt functions. These represent the convolution of a Gaussian (accounting for the instrumental broadening) and a Lorentzian function (accounting for the limited lifetime of the respective core hole). In order to obtain reliable XPS results, the identical fitting routine was applied to all samples.

The molecular flux from the quartz microbalance measurement suggests a deposited film of approximately 12 nm thickness. However, Figure 4.8c shows the gold 4f (Au4f) signal of the sample substrate. The Mg-Kff x-ray source is expected to penetrate only up to 2 nm into the bulk. Therefore, the presence of an Au4f signal can only be explained by a lower deposition rate, due to evaporator-sample misalignment or a slightly increased sample temperature that could not be measured during the deposition or XPS measurement, but what might have increased in front of the evaporator sufficiently to make multilayer desorption (310 K) occur.

The carbon 1s (C1s) signal shows two major contributions. By comparison to compatible reference data, the larger peak can be divided equally into two experimentally

unresolved sp^2 carbon contributions at 287.4 and 287.9 eV from the C_6N_7 core. In each heptazine unit containing six carbons, three respective carbons are chemically identical, identified as C_1 and C_2 in Figure 4.8b. The carbon atoms adjacent to the electron donating azide groups are expected to show a slightly lower binding energy than the γ-carbon and are therefore attributed to the signal at 287.4 eV. The chemical shift of the TAH carbon species is in good agreement with 288.3 eV, the N–C=N signal of already polymerized carbon nitrides known from literature.[105] The peak at 284.5 eV can be attributed to the alkyl compounds (C–C) in adventitious carbon impurity that is always found on samples transferred through air. However, the presence of oxygen signal suggest also a contribution from ketone (C=O) or ether (C–O–C) functional groups, as well common for adventitious carbon.[103] These oxygen-containing groups have a C1s binding energy of 288.2 and 285.8 eV and are hidden below the other signals. Due to the low coverage, this contribution it is not considered in the signal fitting. Possible shake-up satellite from the π-system of the TAH molecule, which are expected at approximately 292 eV were not resolved.

The nitrogen 1s (N1s) signal in Figure 4.8e shows four nitrogen contributions, which match the nitrogen atoms in the molecular structure (see Figure 4.8b). During the fitting we kept the ratios within the heptazine core (N_{center}:N_{ring} = 1:6) and the azide group ($N_{central}$:N_{outer} = 1:2) constant. The lowest binding energy signal at 398.1 eV can be assigned to six nitrogen atoms of the C_6N_7-ring, while the central nitrogen at 399.6 eV is shifted to higher binding energies. Although tertiary amines are usually found at 401.5 eV[106], the delocalized π-system can explain the lowered binding energy of this nitrogen atom.[94] The binding energies of the six nitrogens of the C_6N_7-ring are in good agreement with literature-known values for already polymerized TAH molecules at 398.8[105] or 399.1 eV[106].

The N1s signals of the azide group can be divided into two contributions. The binding energy of 400.6 eV is associated to the two outer nitrogens, while the central nitrogen with the positive charge appears with a binding energy of 403.8 eV. A previous report with ether-group stabilized azides shows XPS signals at 401.8 and 405.4 eV, slightly higher in binding energy compared to our results.[107] This deviation can be explained by an electron back-donation in the anti-binding π^* orbital of the adjacent heptazine. The intensity of the reactive azide group signals showed only 69 % of the expected intensity when comparing to the heptazine N1s signals. This suggests that the TAH molecule lost one out of three azide group in average during the XPS measurement. This x-ray induced photolytic azide decomposition (discussed in detail in Section 4.2.3) leads most probably to the formation of an amine species at 399.8 eV. The removal of one azide group in average is also reflected in the decreased

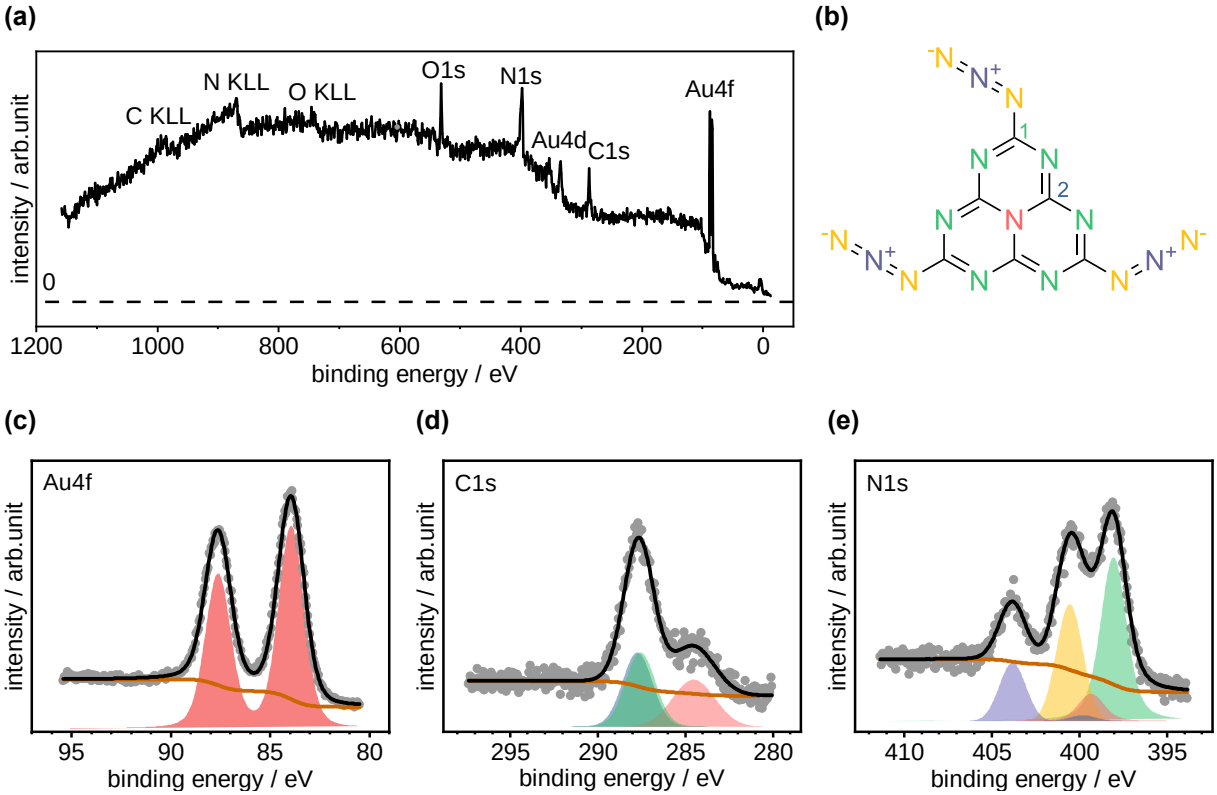

Figure 4.8. X-ray photoelectron spectra of TAH vapor-deposited on Au(111) for 30 min at an evaporator temperature of 440 K. **(a)** The overview spectrum shows carbon, nitrogen, gold, and oxygen signals. **(b)** Molecular structure with color-coded atoms that match the four nitrogen and two carbon contributions. **(c)** The gold 4f signal of the Au(111) surface. **(d)** The C1s spectrum with the two TAH-carbon contributions (■ carbon adjacent to the azide group and ■ triazine-briding carbons). ■ Adventitious carbon is present due the sample transfer in air. **(e)** N1s spectrum with two signal contributions for each azide and heptazine unit. The ■ centered nitrogen of the azide group shows the highest binding energy, followed by the ■ remaining azide nitrogen. The ■ amine and the ■ sp^2 nitrogen form the heptazine core. As one azide group was removed, the formed amine species is fitted by ■.

overall nitrogen content. The total measured C:N ratio was 0.45 and does not match the expected atomic ratio 0.38 of TAH. This calculation includes a correction for the different N1s and C1s cross sections.[108]

The ease of making carbon nitride materials will be decisive for its applicability. Simple preparation techniques are therefore advantageous. We investigated the deposition of TAH on Au(111) surfaces also from a solvent-based approach. We dipped the gold sample in TAH/benzene solution (c_{TAH}: 0.35 mM) and retracted the sample after 15–30 min. The remaining liquid film on the gold surface had a volume of approximately 10 µL as estimated from the deposition of droplets on similar surfaces. At such

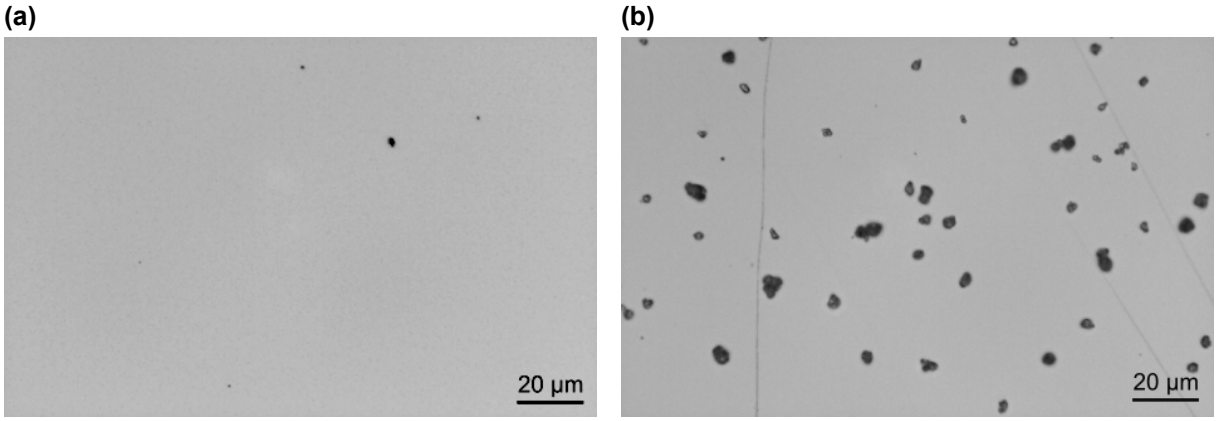

Figure 4.9. Optical microscopy images of **(a)** vapor-deposited TAH on Au(111). The film thickness estimated via the Sauerbrey equation is 12 nm. The sample was already exposed to x-ray and 385 nm UV light and is expected to be fully polymerized. **(b)** The gold surface with liquid-deposited TAH film from benzene solution. The solution concentration was matched to result in 12 nm layer thickness. The sample was not exposed to radiation or elevated temperatures.

volumes and concentrations, the calculated remaining TAH layer after solvent evaporation should correspond to 12 nm film thickness. Again, the sample was transferred to UHV and investigated by XPS. Figure 4.10a shows the overview XPS spectrum with the gold, carbon, nitrogen, and oxygen signals. The appearance of the Au4p peak, not seen for the vapor-deposited sample, indicates a lower TAH coverage. However, optical microscopy reveals rather an aggregation of TAH on the support and hence a lower apparent XPS signal (see Figure 4.9). Indeed, AFM measurements probe the presence of nanoparticles that are higher than 2 nm and therefore were not be fully penetrated by XPS (see Figure 4.15b). The vapor-deposited sample in contrast shows only little agglomeration. The aggregation of TAH molecules can be explained by capillary flow effects during the solvent evaporation.[109] Initial attempts with a spin-coater did not prevent aggregation. For a homogeneous deposition, more advanced liquid deposition approaches such as electrospray ionization deposition, possible with subsequent mass filtering, are needed.[110] The presence of TAH between the aggregates is confirmed by detection of the local fluorescence response related to TAH, upon excitation with laser light.

Figure 4.10b shows the C1s signal, with the heptazine and adventitious carbon contributions. The amount of adventitious carbon for the liquid-deposited sample (determined by referencing against the Au4f signal from the overview spectra) decreased by 25 % compared to the vapor deposition, confirming at least a full removal of the benzene solvent. The N1s signal in Figure 4.10c contains the same signal contributions as in the vapor-deposited sample. The TAH molecules had 61 % of the azide groups from

the synthesis left, i. e. the same amount as for the vapor-deposited sample. Again, the TAH molecule reacted under the x-ray beam. Besides the TAH aggregation during the deposition, the liquid sample preparation can fully substitute the vapor deposition.

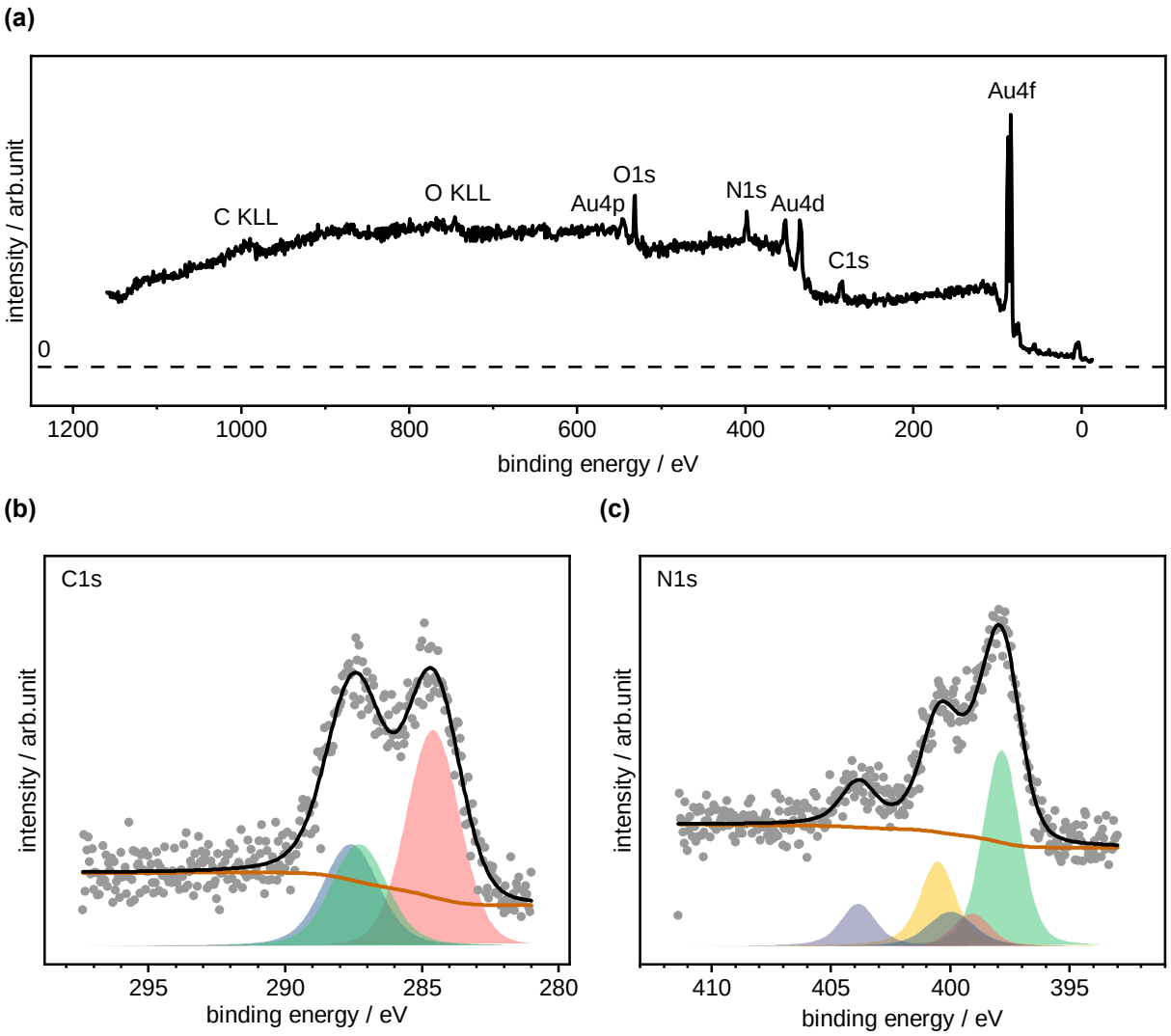

Figure 4.10. X-ray photoelectron spectra of TAH on Au(111), liquid-deposited from a benzene solution. While a similar amount has been deposited as by vapor deposition in Figure 4.8, the here detected XPS signal is lower due to aggregation. **(a)** The overview spectrum incluedes a Au4p signal. **(b)** The C1s signal with the two heptazine (■, ■) contributions and the ■ adventitious carbon. **(c)** The N1s signal with two nitrogen species for the heptazine (■, ■) and the azide (■, ■), respectively. As one azide group reacted during the XPS measurement, a formed amine species is added (■). The color-coding is referenced to Figure 4.8b.

4.1.3. Deposition on Highly Ordered Pyrolytic Graphite

We investigated the TAH deposition as well on HOPG for two reasons. On the one hand we intended to optimize the formation of a well-ordered network by modulating the

interaction to the support, expected to be much lower on graphite. On the other hand, for a technological perspective: A pure carbon support, cheap, easy to prepare, and electrochemically stable would be the ideal platform. As with the gold sample, we deposited the TAH molecule on the HOPG surface with the vapor and liquid approaches. Optical microscopy revealed a similar behavior for both depositions, on HOPG as on gold. More large aggregates were found on the liquid-deposited HOPG sample, but here as well the area between large particles was covered with TAH molecules. Vapor deposition and liquid deposition resulted in similar XPS spectra on HOPG.

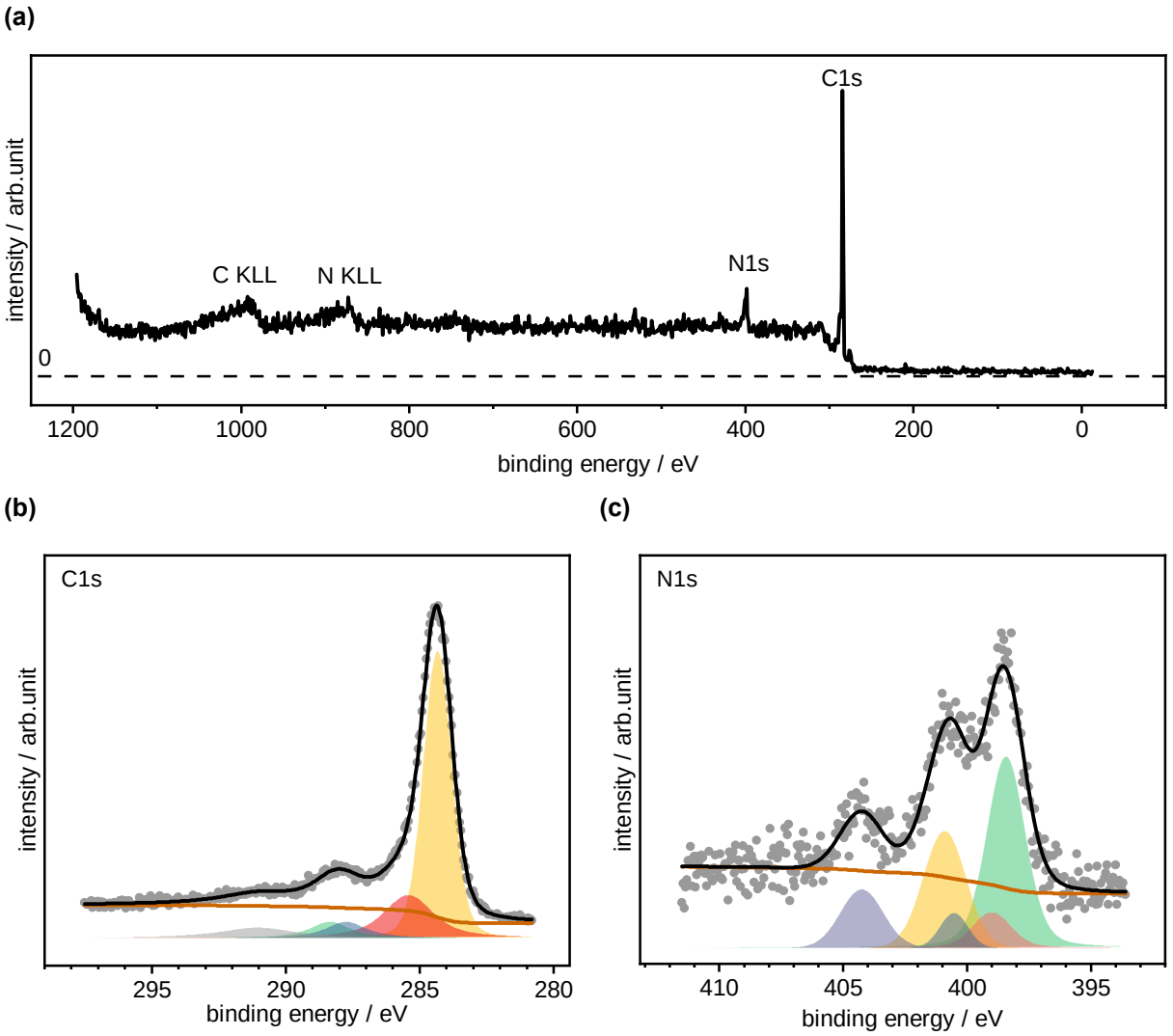

Figure 4.11. X-ray photoelectron spectra of TAH liquid-deposited on HOPG from a benzene solution. The deposited TAH amount was identical to that on the gold sample. **(a)** The overview spectrum with carbon and nitrogen signals. **(b)** The C1s signal with two ■, ■ heptazine contributions, ■ adventitious carbon, ■ sp^2 carbon from HOPG, and ■ graphite shake-up satellite. **(c)** The N1s signal with two nitrogen species for the heptazine (■, ■) and the azide (■, ■), respectively. The color-coding is referenced to Figure 4.8b.

Figure 4.11 shows the XPS spectra of a liquid-deposited sample, which were shifted to match the HOPG signal at 284.3 eV.[104] The overview spectrum shows the carbon and nitrogen photoelectron and Auger signals. The C1s signal is dominated by the sp^2 carbon contribution from HOPG at 284.3 eV. The graphite peak is known for its asymmetry and the adjacent signal at 285 eV is therefore a convolution of the asymmetrical sp^2 carbon and the adventitious carbon contribution. At 287.7 and 288.4 eV the two carbon species from the heptazine are found. At 291 eV the shake-up satellite due to the $\pi \rightarrow \pi^*$ transition can be found, known for graphitic materials.[111] Again, the N1s signal consists of four peak contributions. The heptazine sp^2 nitrogen is located at 398.4 eV and the central one at 399.9 eV. The azide group is divided into the outer nitrogens at 400.9 eV and the inner nitrogen at 404.3 eV. As before, x-ray beam damage lead to 63 % of the original azide amount. The resulting amine peak appears in the fit at a binding energy of 400.6 eV, still with a slightly lower intensity than expected, but less deficient than for the deposition on Au(111). While a previous study reports the possible reaction of highly reactive azide groups e. g. azidoformate or cyanogen azide, with benzene solvent to azepines (as shown in Figure 4.12) and hence we observe the same azide concentration on the liquid-deposited as on the vapor-deposited sample, this side reaction does not occur during our liquid deposition approach.

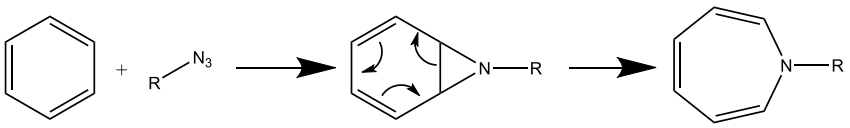

Figure 4.12. The literature-known decomposition of azide group and reaction with benzene solvent was not observed in our case.[95]

Table 4.1 summarizes the peak positions of the XPS signals for the two deposition approaches on the two surfaces. Literature values are also listed, but it has to be noted that these values originate from already polymerized carbon nitride. As a general trend we can state that the values for the gold sample are slightly lower in binding energy by 0.3±0.1 eV than of the graphite sample and of the bulk reference data. This shift of all peaks can be explained by the enhanced core hole shielding by the metal substrate. The ejected photoelectron is attracted by the positive charge of the created core hole, but if this charge is partly screened by the metal surface charge density, the electron leaves the surface with a higher kinetic energy. The binding energy appears then to be lowered.[112] This effect was observed as well for other adsorbed π-systems like porphyrins and phthalocyanines. A tetraphenylporphyrin monolayer showed a shift for both N1s and C1s of approximately 0.5 eV on an Au(111) surface compared to the multilayer signal.[113] The presence of this effect pronounces a low coverage similar to

a monolayer. However, it was not possible to determine the TAH surface coverage by STM, as the TAH did not self-assemble and was highly mobile on the surface.

Table 4.1. Summary of N1s and C1s peak positions of the TAH molecule for different depositions methods (vapor- and liquid deposition) on Au(111) and HOPG surfaces. Literature values are given for comparison, but only values for already reacted carbon nitride networks CN_x are reported so far.

	Au(111)		HOPG		CN_x polymer
	vapor	liquid	vapor	liquid	
C=**N**–C	398.08	397.85	398.42	398.44	399.06[106], 398.8[105]
N–C_3	399.61	399.61	399.87	399.9	400.36[106], 400.1[105]
–**N**=N=**N**	400.57	400.39	400.77	400.85	
–N=**N**=N	403.81	403.74	403.97	404.31	
$C_{hept,\ 1}$	287.35	287.29	287.69	287.71	
$C_{hept,\ 2}$	287.93	287.61		288.39	288.6[106], 288.3[105]

4.2. Polymerization to Carbon Nitride

The polymerization of TAH offers a synthesis route to carbon nitride without release of hydrogen. This reduces the amount of possible reactants for termination by formation of primary and secondary amines and enables a higher selectivity and structural uniformity in the network formation. Miller, Holst, and Gillan [93] observed the explosion-like reaction of TAH at 470 K. The yellow powder turns into a porous, fluffy, and brown powder, that transforms into yellow-tanned after several weeks of storage in air, due to possible hydrolysis. The carbon nitride is thermally stable for short time periods at 873 K, then slowly decomposes over hours. The thermogravimetric analysis shows an overall release of three N_2 molecules per TAH unit during the reaction.[93] This indicates only a partial polymerization, as a full network formation would result in the formation of four N_2 molecules per TAH.

We start here with the polymerization of TAH powder to carbon nitride at 473 K, both in argon atmosphere and under vacuum conditions ($p < 5 \cdot 10^{-2}$ mbar). Figure 4.13 shows the infrared spectra of attenuated total reflection IR spectroscopy (ATR-IR) measurements before and after the reaction. The TAH molecule shows the four specific vibrations from the heptazine ring at 818, 1356, 1526, and 1601 cm^{-1}, in good agreement with the literature values at 818, 1359, 1529, and 1608 cm^{-1}.[93] Hereby, the vibration at 818 cm^{-1} can be traced back to the triazine subunit.[114] The region at 2260 – 2140 cm^{-1} was previously assigned to the azide group.[115] While in the TAH spectrum an azide signal at 2169 cm^{-1} can be found, the two reacted samples show, if at all, only minimal azide traces left. An indication for a highly linked network formation of carbon nitride is the absence of primary and secondary amine groups around 3200 cm^{-1}. For both samples the N – H contribution was very small, suggesting a good linkage, expected for reactions in absence of water.[114] In the fingerprint region below 2000 cm^{-1}, both spectra of the reacted sample are similar to those observed for other bulk carbon nitride syntheses.[116] The heptazine and triazine vibration signals are broadened and damped, which can be attributed to the polymeric character of the product. Tong et al. [116] observe an oxygen-induced cleavage of the heptazine-bridging amine group, which resulted in the increase of oxygen signals at 1712, 1088 and 972 cm^{-1}. As none of these signals occur at the reacted samples, the interaction with oxygen can be excluded.

TAH with the three azide groups shows a 2.55x higher molar heat of formation ($C_6N_7(N_3)_3 \longrightarrow 8\,N_2 + 6\,C$) than hydrogen terminated heptazine ($C_6N_7H_3 \longrightarrow 3.5\,N_2 + 1.5\,H_2 + 6\,C$),[94] which indicates the immense energy stored in the azide group.

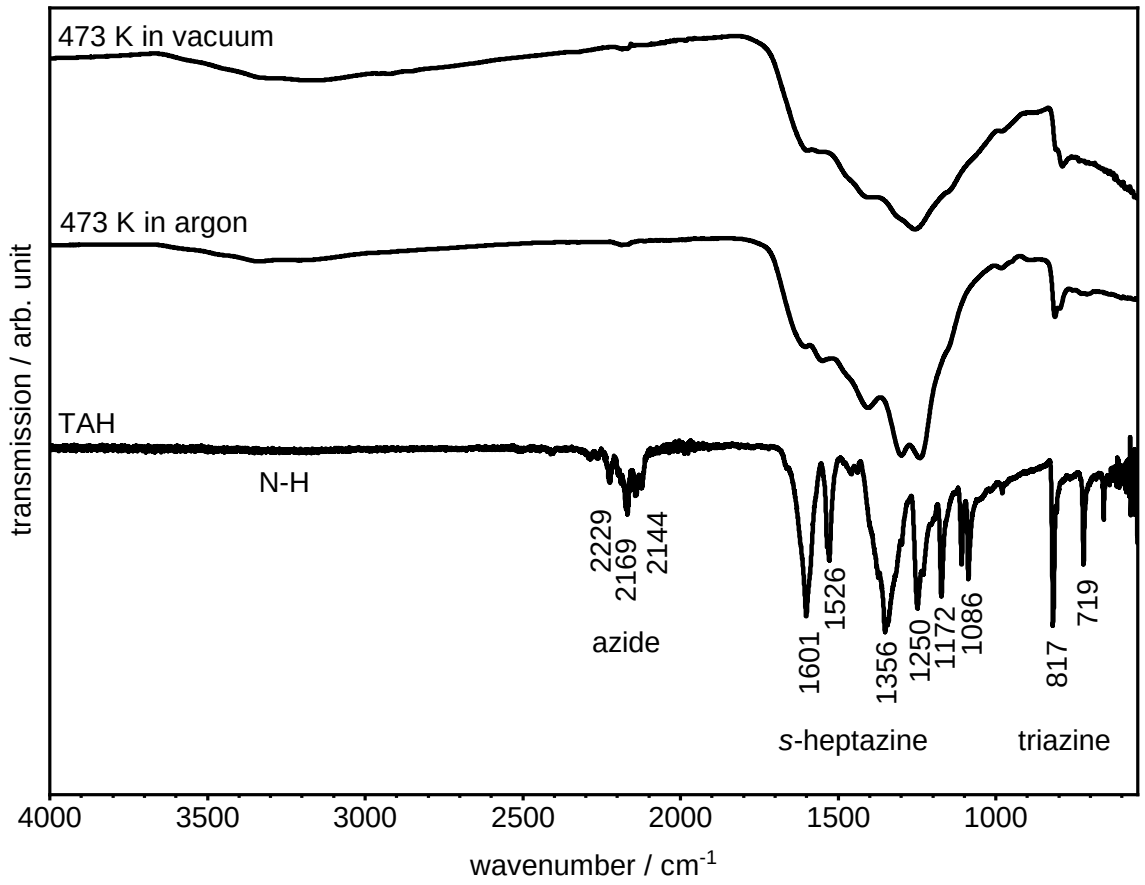

Figure 4.13. IR spectra of TAH precursor and bulk reaction products reacted at 473 K under argon or vacuum conditions. The TAH molecule was identified by the *s*-heptazine, triazine and azide vibrations. The azide contribution vanishes for the reacted carbon nitride, while N – H species are formed. A detailed signal analysis can be found in the text.

The resulting irreversible formation of nitrene radicals has to be steered appropriately to yield well-ordered 2D films that are well interlinked. The binding of the precursor and potential intermediates to the surface are hence expected to play a crucial role in the network formation. Besides the impact on the film morphology, the volatile nature of TAH that permits its deposition by evaporation can at the same time lead to an evaporation before and during the reaction (see Section 4.1). As the on-surface reaction is performed with very small TAH concentrations, a partial desorption of the reactant will strongly influence the network formation. In the following the on-surface reaction is studied on HOPG and Au(111).

4.2.1. Triazido-Heptazine Interaction with Graphite

As the TAH polymerization evolves gaseous nitrogen as a side-product, mass spectrometry enables us to follow the reaction. However, already the mass spectrometry study of the powder evaporation described in section 4.1 showed a constant evaporation of TAH before and throughout the reaction. For a mass detection with elevated sensitivity, a sniffer was placed above the surface while heating (distance < 0.2 mm). This instrument houses a mass spectrometer and has an increased sensitivity due to exclusion of external background signals and a high product collection efficiency.[117] However, this setup is limited to the mass 100 amu and the fragment mass 78 amu was therefore used to identify the mass 296 amu of TAH itself. In order to disentangle the nitrogen signal from intact TAH from that of the nitrogen-releasing reaction, the TAH fragment trace was scaled in intensity to match the nitrogen mass 14. All the nitrogen signal that exceeds the TAH signal can then be assigned to the on-surface reaction of the TAH molecule. Figure 4.14a shows the gaseous products that are detected by the mass spectrometry during the temperature ramp from room temperature to 533 K under UHV conditions.

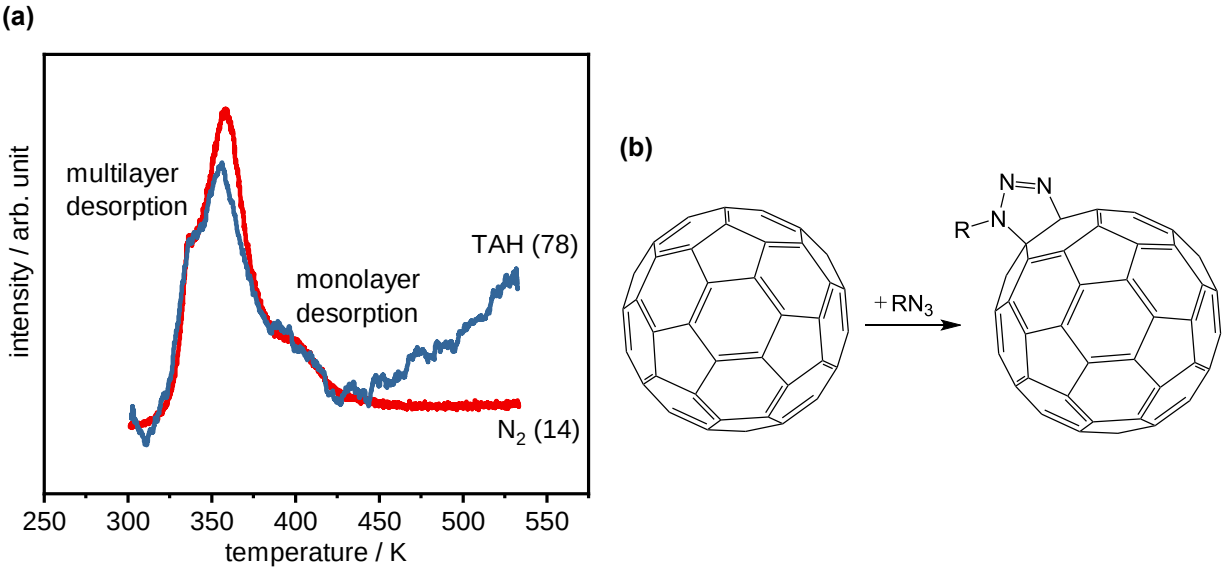

Figure 4.14. **(a)** Gaseous products evolving during heat-induced desorption and reaction of TAH on HOPG. The vapor deposition yielded a multilayer starting coverage. The heating rate was 1 K/s. **(b)** [3 + 2] Cycloadditions of $R-N_3$ azide with sp^2 carbon in fullerenes that occur already at 333 K. This reaction is the first step of several possible pathways, followed by subsequent N_2 release.[118]

Similar to the powder sample in Figure 4.2, the evaporation of intact TAH starts at 330 K. The majority of the detected nitrogen can be attributed to TAH evaporation,

as the signals largely overlap. The first peak in the desorption signal is assigned to the multilayer desorption, which is expected to show the lowest binding energy. The shoulder above 380 K is attributed to monolayer desorption from HOPG. Above 425 K no nitrogen is detected and therefore, we believe that the further increase of TAH signal above 450 K is a measurement artifact that might be related to background contributions due to nozzle heating. This early desorption of TAH explains the lack of excessive nitrogen generation at reaction temperature around 445 K, which would be expected for the polymerization. The binding between the HOPG and TAH is not strong enough to exceed the enthalpy of vaporization. However, above 350 K we observe a nitrogen that is somewhat larger than the TAH signal, as the result of some ongoing TAH reaction activity. A possible reaction in this context might be the [3 + 2] cycloaddition of the organic azide to the HOPG surface, similar to the one observed upon fullerene functionalization, that occurs already at temperatures of 333 K (see Figure 4.14b).[118] However, such reaction pathways would lead to nitrogen atoms binding to the surface. As only vanishing N1s signal intensity was detected in the XPS, the TAH desorbs mostly unreacted.

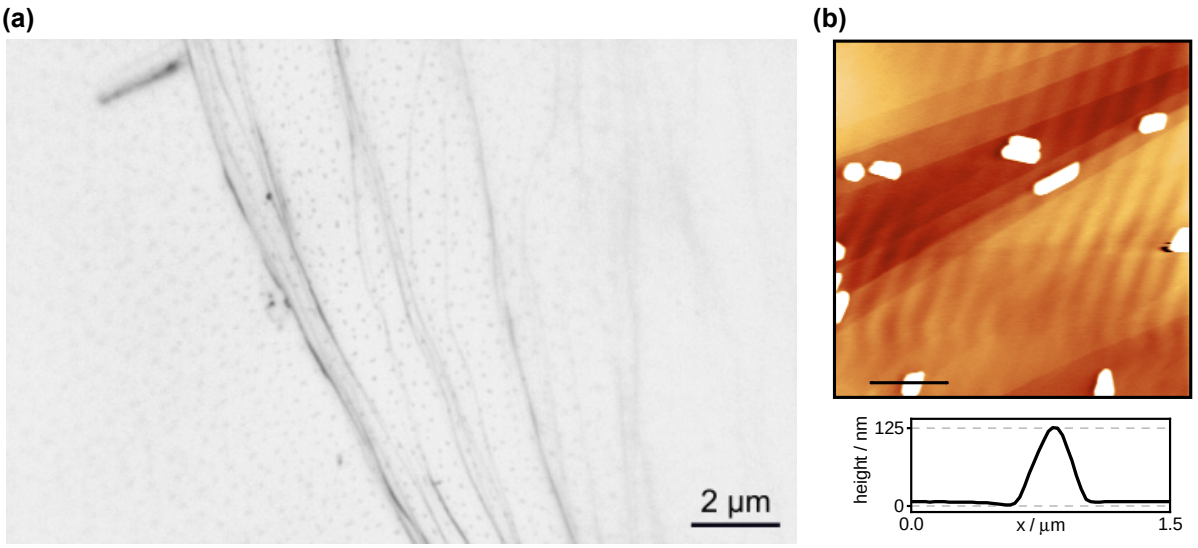

Figure 4.15. **(a)** Optical microscope image of thermally polymerized carbon nitride on HOPG. The aggregate structure which resulted from the liquid deposition remained stable during the reaction. **(b)** AFM measurement of the carbon nitride sample with indicated line profile revealed the submicrometer particle size. Image size: 7x7 µm.

While the vapor-deposited HOPG sample did not result in any reaction products detected by means of XPS, however, the liquid-deposited sample with its aggregate structures lead to carbon nitride signals. The aggregate structures did not fully desorb during the heating to 453 K. Figure 4.15 shows optical microscopy and AFM

measurements. The aggregates were uniformly distributed over the surface without any preferred surface site. A reordering during the elevated temperatures seems unlikely. The line profile indicates the submicrometer size of the particles. The carbon nitride in those particles is expected to be fully decoupled from the HOPG surface and hence, we expect the same chemical nature as in the powder polymer.

XPS has been applied to understand the chemical changes during the reaction. The reaction of the azide group to a tertiary amine, as shown exemplary in Figure 4.16, offers the possibility to follow the reaction by the decrease of N1s azide signal and the increase of a novel N1s amine contribution. The different binding energy of the newly formed amine compared to the central heptazine amine can be explained by the delocalized π-system.

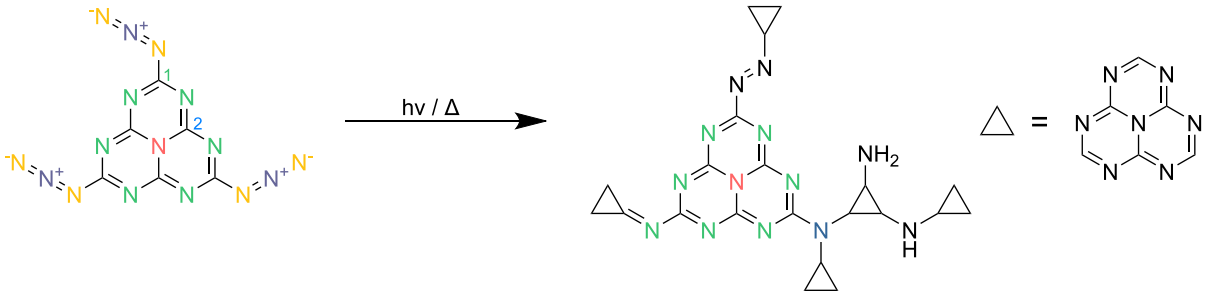

Figure 4.16. Possible condensation pathways of the TAH polymerization to carbon nitride under the release of nitrogen via an assumed nitrene radical intermediate. The reaction is initiated either by light irradiation or thermal activation. The two azide (■, ■) contributions vanish, while the ■ tertiary amine increases, if the network is formed. However, also azo, sp^2 nitrogen, primary, or secondary amines can occur. The ■ and ■ heptazine nitrogen contributions do not change their intensity throughout the reaction. The two carbon heptazine species in the TAH molecule are chemically indistinguishable after the removal of the electron-donating azide group.

Figure 4.17 compares the XPS spectra of the aggregates on HOPG with carbon nitride nanosheets prepared via a melamine synthesis. The preparation of the carbon nitride nanosheets consisted of the melamine powder reaction, the liquid exfoliation with ultrasonication, and the drop-cast deposition on Au(111).[119] The carbon signals in Figure 4.17 vary only because of the different supports. The nanosheets were supported on gold and therefore the C1s signal in Figure 4.17a shows only two contributions from the heptazine carbon at 288.3 eV and the adventitious carbon from the sample transfer at 285.1 eV. The HOPG sample instead, contains the previously observed contributions from the sp^2 carbon from HOPG and additionally at 288 eV the heptazine carbon (see Figure 4.17c). An XPS study by Burdina et al. [81] attributes a double-peak feature in C1s spectra to amorphous CN_x species, while crystalline ones

only lead to a single contribution. Hence, both our samples are expected to have a crystalline character.

The nitrogen signal gives insights into the chemical species of the formed amine. Figure 4.17b shows the XPS spectra of the nanosheet sample with the outer heptazine nitrogen at 398.6 eV and the central tertiary heptazine amine at 399.8 eV. The latter was coupled in intensity during the fitting to the heptazine sp^2 nitrogen atoms to match the atomic ratio of 1:6. At 401 eV the novel amine species appears, which again indicates by the chemical XPS shift the formation a tertiary amine. The amount of novel linking nitrogen species is similar to that of the central amine in the heptazine and matches therefore very well an overall linking nitrogen content of one per heptazine unit. The nitrogen signal from the TAH polymerization on HOPG again shows the two respective contributions from the heptazine at 398.7 and 399.9 eV. The novel linking nitrogen species can be found at 401.2 eV. The condensation pathways described in Figure 4.16 suggest the possible formation of several nitrogen species, that would be found at similar binding energies. Indeed, the Lorentz width of the signal was much higher than the nanosheets sample, which indicates the presence of more than one nitrogen linking species. Also the shift to higher binding energies suggest the presence of primary and secondary amine species and hence more N–H terminations. The total intensity of the linking nitrogen suggest 3.7 nitrogen atoms per heptazine unit, which significantly surpasses the theoretical value of 1. While the XPS cannot fully resolve the small differences in binding energies of the different condensation products, the formation of N–H terminations appears very likely, as hydrogen and water are present under UHV conditions.

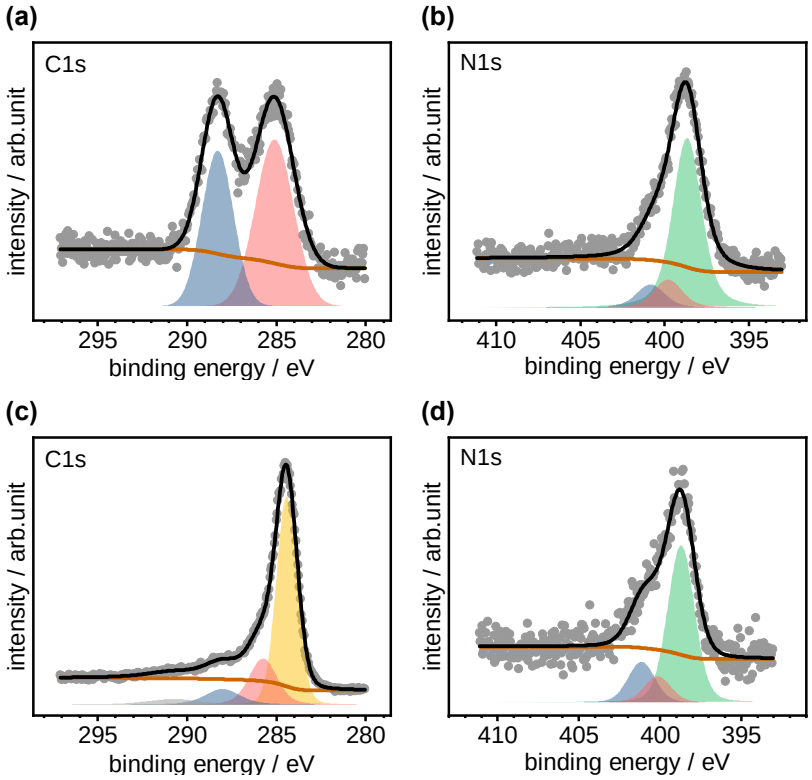

Figure 4.17. **(a – b)** XPS analysis of carbon nitride nanosheets prepared from melamine and drop-casted on Au(111). **(a)** The C1s signal shows the ■ heptazine and ■ adventitious carbon signal. **(b)** The nitrogen signal consists of the ■ heptazine ring, the ■ central heptazine amine, and the ■ linking nitrogen species. Both, the intensity and the chemical shift of the latter suggest the primary formation of tertiary amines and hence a good linkage. **(c – d)** The polymerized liquid-deposited TAH on HOPG: **(c)** The C1s signal is dominated by the HOPG substrate with the ■ sp^2 carbon and the ■ shake-up satellite. Additionally, ■ adventitous carbon is present. The ■ heptazine carbon can be found at 288 eV. **(d)** The nitrogen signal shows besides the ■ heptazine, and the ■ tertiary amine also the ■ linking nitrogen signal. The intensity of the latter exceeds the expectations from tertiary amine linkage. For details see the text.

4.2.2. On-Surface Polymerization on Au(111)

Similar to the HOPG sample, TAH was vapor-deposited on the gold single crystal and the reaction was induced by heating. The gaseous products were detected by mass spectrometry. Figure 4.18a shows the gaseous nitrogen and TAH intensity during a heating-induced reaction starting from room temperature to 627 K. Again, all the nitrogen signal that exceeds the TAH signal can be assigned to the ongoing polymerization reaction. Note that here the deposition time was adjusted to reach a coverage below one monolayer of TAH. Although we deposited only a submonolayer coverage, already from 310 K TAH molecules started to desorb, similar to the multilayers on the

HOPG sample. The polymerization reaction sets in at 405 K, which can be identified by the sudden extensive release of nitrogen, while the TAH signal remains constant. The successful polymerization on the gold support suggests a higher interaction between TAH and gold compared to the HOPG sample. The reaction temperature is 40 K lower compared to that in the powder sample, the polymerization is hence catalyzed by the gold surface. The reduced reaction temperature was evidenced by the measurement of a fully reacted carbon nitride N1s XPS signal after the sample was heated to 438 K. The measured spectra were consistent with samples heated to temperatures above 445 K.

Whether the desorption of TAH molecules at 310 K originates from the first or a higher layer is answered by the variation of the deposited coverage. Figure 4.18b shows the reaction of a TAH/Au(111) sample with a multilayer coverage. The onset of the desorption is identical to that of the previous sample, however a clear multilayer desorption peak emerges. Again the TAH desorption continues throughout the reaction at a rather constant level. Why the amplified TAH signal does not match the nitrogen signal above temperatures of 350 K, similar to the HOPG sample remains unclear. We hypothesize background signals from the sniffer nozzle, observed for large TAH dosages when the nozzle gets heated. As the multilayer desorption was observed at the same temperatures as the previous sample, we attribute the TAH desorption for the submonolayer coverage to a second layer desorption. TAH is expected to adsorb in well-ordered layers as it does in its crystal structure.[102,120] Since the first adlayer is strongly polarized by the support, the interaction to the second layer will be stronger as the interaction between second and higher layers. We therefore attribute the second broad desorption peak to a second TAH layer that experiences a strong, coverage dependent binding to the surface. This is in good agreement with second-layer features observed with STM performed on these samples. The molecule-surface interaction between first-layer TAH and gold matches well the enthalpy of vaporization of the TAH molecule and ensures the persistence of TAH throughout the heating. It is advantageous for a successful 2D film growth, that the desorption of the amorphous multilayer occurs before the reaction sets in.

The chemical analysis of the product by means of XPS gives insights into C_3N_4 product yield and N–H termination, similar as for the powder-like sample in section 4.2.1. Here, a liquid-deposited gold sample was heated for 15 min to 473 K in vacuum, without exposure to UV or x-ray light. The sample was then transferred to a separate XPS vacuum system. The overview spectrum in Figure 4.19a shows the expected presence of oxygen, carbon, nitrogen, and gold. The high-resolution scan of the Au4f signal in Figure 4.19b reveals the existence of a single gold species. Similar to the powder and

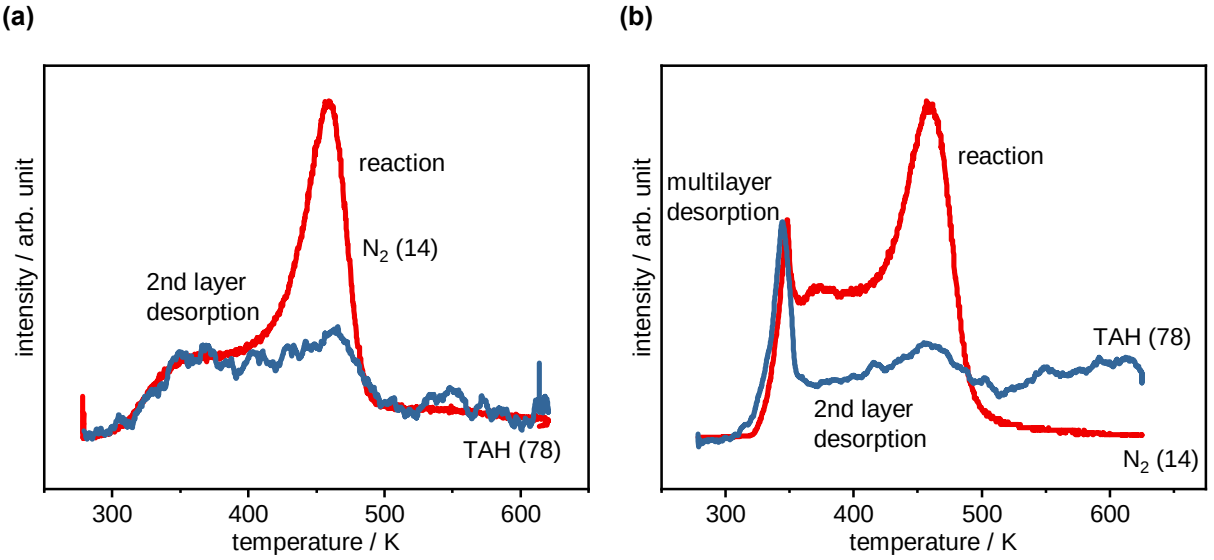

Figure 4.18. Gaseous products during heat-induced desorption and reaction of TAH on Au(111) with **(a)** submonolayer coverage (2 min vapor deposition) and **(b)** multilayer coverage (8 min vapor deposition) . The heating rate was 1 K/s for both samples. The ■ TAH signal was fitted to match the onset of the ■ nitrogen signal.

nanosheet samples, the C1s signal in Figure 4.19c shows only two contributions, from the sp^2 heptazine carbon atoms from the adventitious carbon. Figure 4.19d shows the N1s signal with the two heptazine signals at 298.4 and 299.3 eV. The linking nitrogen species can be found at 400.6 eV. The intensity analysis results in 1.9 nitrogen atoms per heptazine unit, which suggests that about every third linking nitrogen atom is a terminating one, pointing more to a chain rather than a network formation ($2 \cdot 0.5$ bridging $+ 1 \cdot 1$ terminating N atom per heptazine). Both, chemical shift and intensity are more similar to the nanosheet N1s spectrum than to the results on HOPG (powder-like sample), indicating a high degree of linkage. The gold surface appears to influence the condensation mechanism, which leads to a higher cross-linking of the heptazines. This and the possible formation of nitrene intermediates is discussed in Section 4.2.3. The total carbon to nitrogen content suggests a stoichiometry of $C_3N_{3.8}$. Although the value fits well the expected theoretical value of a fully linked carbon nitride network, the N–H termination suggested by the N1s signal together with STM images (see Figure 4.20), indicate that the heptazine carbon signal is overestimated in our XPS evaluations. As stated earlier, the presence of oxygen-containing carbon groups from the adventitious carbon – which were not considered during the fitting – are convoluted for the heptazine carbon signal and might be the reason for this overestimation. The vapor-deposited sample shows similar XPS spectra and hence confirms the improved network formation on the gold surface as compared to the powder-like HOPG samples.

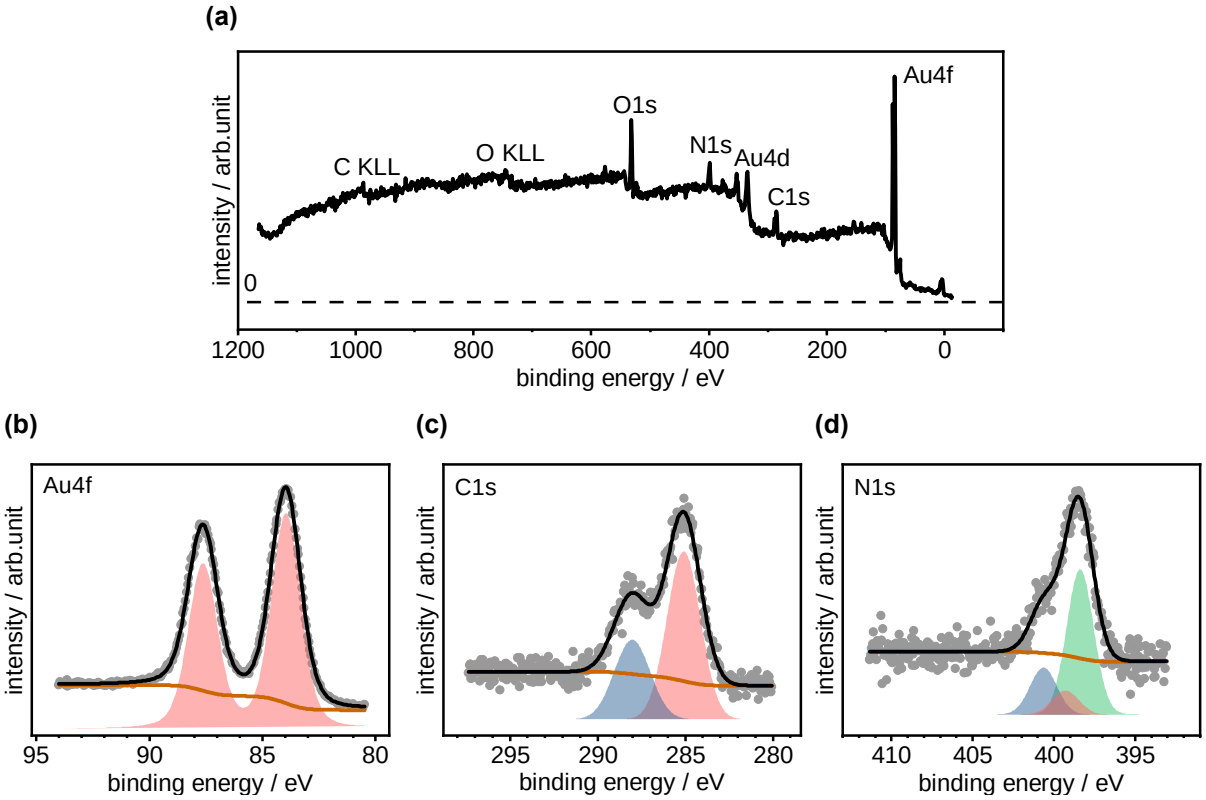

Figure 4.19. X-ray photoelectron spectra of TAH, liquid-deposited on Au(111) from a benzene solution. The sample was heated to 473 K to induce the polymerization. **(a)** The overview spectrum reveals the presence of gold, carbon, oxygen, and nitrogen. **(b)** C1s signal with the ■ heptazine contributions and ■ adventitious carbon. The possible presence of oxygen-containing groups, as suggested by the presence of an O1s signal, were not considered. **(c)** N1s signal with nitrogen species for the ■ heptazine and ■ the amine nitrogen respectively. The novel ■ linking nitrogen species is expected to include different, tertiary and secondary amine species. The color-coding is referenced to Figure 4.16.

The structure of the polymerized carbon nitride films on Au(111) was studied with UHV-STM (see Figure 4.20). The samples were vapor-deposited, heated and subsequently imaged under UHV conditions without exposure to air. Therefore no introduction of adventitious carbon is expected. Although the same evaporator and similar deposition times and distances were used for the film preparation, the sample showed a lower surface coverage after annealing to 673 K instead of 623 K (see Figure 4.20a). This could be due to slight decomposition as shown by the thermogravimetric-differential analysis in Figure 4.2. Similar results due to the higher annealing temperature were also observed by Wang and Gillan [114] for the triazine-based carbon nitride. The thermal decomposition to nanographitic particles and carbon nanotubes can set in at temperature above 550 K.[114] Figure 4.20a – b shows STM image of several Au(111) terraces separated by monoatomic steps. The carbon nitride film appears

to not overgrow the edge of an Au(111) step, but the growth appears to preferrable start from the edges on the adjacent terraces both, upper and lower. However, also nucleation on the terraces themself is observed. The film height was extracted with line profiles for each respective image. It has ans apparent height between 0.13 and 0.19 nm. Especially in Figures 4.20c – d a second layer of carbon nitride can be observed. However, this second layer is laterally not as extended as the first layer. With an apparent height of 0.25 nm, it is higher than the first layer. This height corresponds well to the stacking height of 0.3 nm in crystalline TAH[120,121] – the different first layer height includes electronic effects related to the strong interaction with the support. However, also the second-layer has to be polymerized, as a desorption was not observed even after heating to 673 K. Whether this second layer forms during heating from the first layer TAH has to be further investigated. From the XPS results, a certain N – H termination of the carbon nitride film is expected and this is indeed observed in the STM images at least when taking the holes and island borders into account. The termination of the film does not show a higher height or interaction with the STM tip, which suggests the absence of sterically demanding end groups. Especially secondary amine termination is expected to lead to a rotation of the adjacent heptazine unit, at least in bulk carbon nitrides.[90] Hence, we expect mainly primary NH_2 terminations. Figure 4.20d shows a detailed STM image in which the crystalline carbon nitride structure can be anticipated. This structure was only observed in the first layer. The lattice constant of $a = 0.78$ nm is in good agreement with the value 0.73 nm determined with TEM.[121]

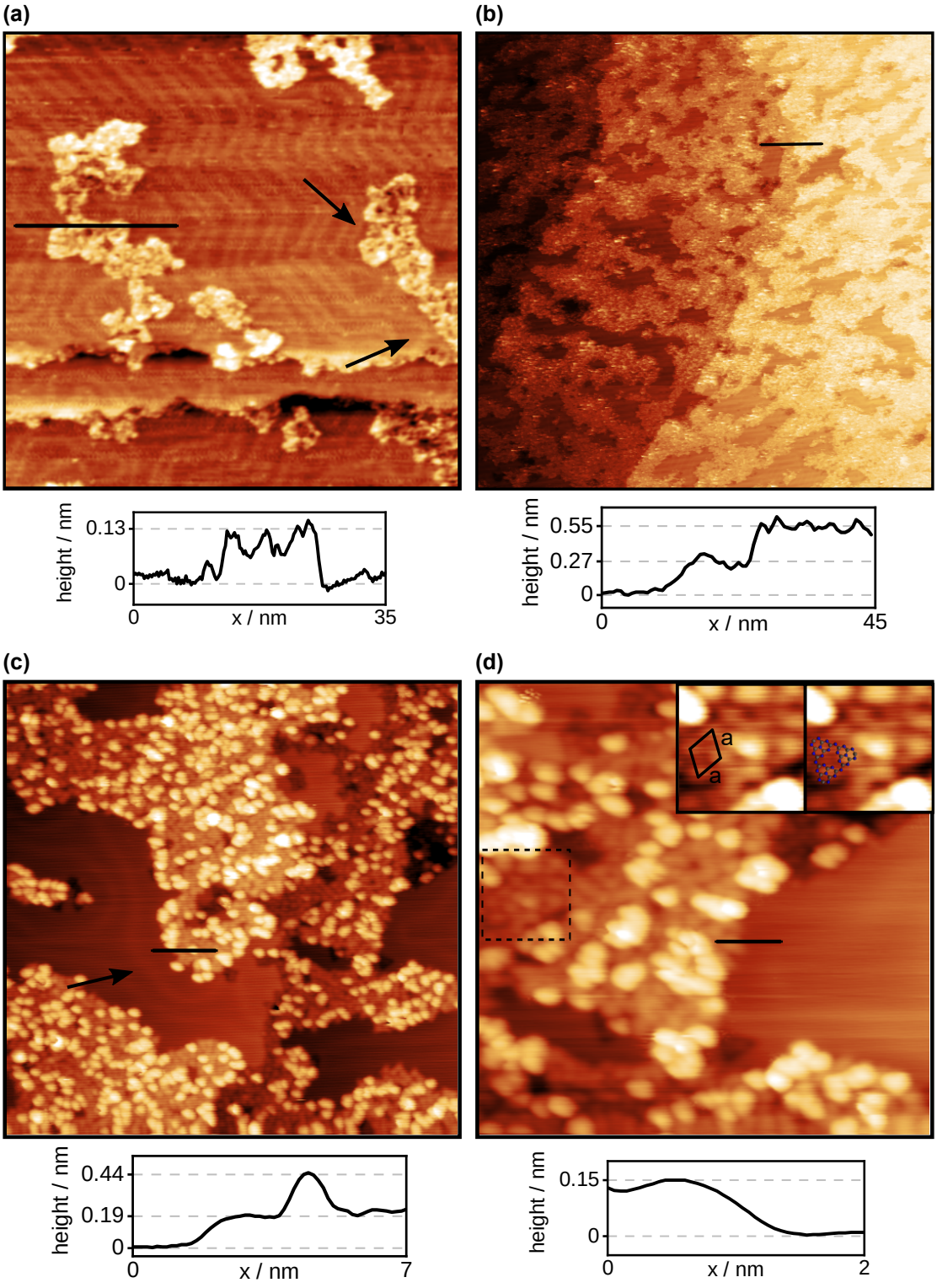

Figure 4.20. STM images of polymerized carbon nitride films on Au(111): **(a)** Low coverage deposition (2 min) and subsequent heating to 673 K. The arrows indicate the alignment of the reconstruction with the carbon nitride film. **(b – d)** Low coverage deposition of TAH, heated to 623 K under UHV conditions. **(c)** Again, the arrow highlights the alignment of the reconstruction with the film. **(d)** The first layer of carbon nitride shows a crystalline structure, which results in a lattice constant a: 0.78 nm. STM details: U_B: 1.5 V, I_T: 400 pA **(a)** 330x330 nm^2, **(b)** 100x100 nm^2, **(c)** 50x50 nm^2, and **(d)** 20x20 nm^2 image size.

Figure 4.20a, c shows the interplay between the carbon nitride film and the Au(111)(22x$\sqrt{3}$) reconstruction. The gold herringbone reconstruction aligns well with the film termination. It remains challenging to disentangle whether the herringbone structure steers the film growth or the surface reconstruction reorders during the polymerization. A concomitant gold hole formation can also be observed (see island borders in Figure 4.20c). The presence of a high gold adatom mobility might allow the recovery of the surface reconstruction after the film formation. The influence of an organic film on a metal surface was already observed for the growth of graphene on copper, where a reconstruction occurred after an annealing step.[122]

4.2.3. Reaction Stimulus: Azide Pyrolysis and Photolysis

Azides are a highly reactive functional group, that can exist either as acid or as aryl azides. While the former can release also N_3 on activation, the aryl azides exclusively form N_2 and a nitrene group. Besides the thermal activation, light irradiation also decomposes the azide group. This offers a second route to carbon nitride networks, besides the thermolysis of the azide group. The formed nitrene species has two non-bonding electrons for the population of two p-orbitals and therefore can exist in either a singlet or a triplet state. The spin conservation especially upon photoexcitation dictates the formation of a singlet state after the azide decomposition. However, an intersystem crossing can lead to a triplet state that is energetic favored, where two non-bonding electrons are separated into different orbitals. The example of phenyl azide demonstrates that the two spin states have a different reaction behavior.[123,124] While the phenylnitrene singlet can undergo ring expansion, the triplet state leads to azoarenes.[89] Yamada, Shizuka, and Matsui [125] suggest for triazide structures (subunit of heptazine) a singlet formation but no ring opening. While phenyl azides form under ring opening azepin structures, the triazide six-ring remains intact.

In the following the photolysis of the TAH azide is compared to the previous results from pyrolysis. The exposure of yellow TAH powder to UV light (365 nm, 3.4 eV) at room temperature under vacuum conditions led to a brownish color. Therefore, the polymerization can be triggered below the calculated TAH band-gap of 4.14 eV.[94] Raman spectroscopy was used to compare the polymer structure from on-surface reactions induced by heating to 453 K or UV light at room temperature (see Figure 4.22). The samples studied here were prepared by liquid TAH deposition. A Raman excitation wavelength of 785 nm was used to supress the known fluorescence of the carbon nitride film and to avoid broad fluorescence-related peaks underlying the background,

that dominate for higher excitation energies. The TAH powder signal shows several peaks, which vanish after the reaction. Also the peak width increased comparable to the IR spectra in Figure 4.13. As both spectra of the reacted samples are similar, no significant structural difference is expected for the two reaction stimuli.

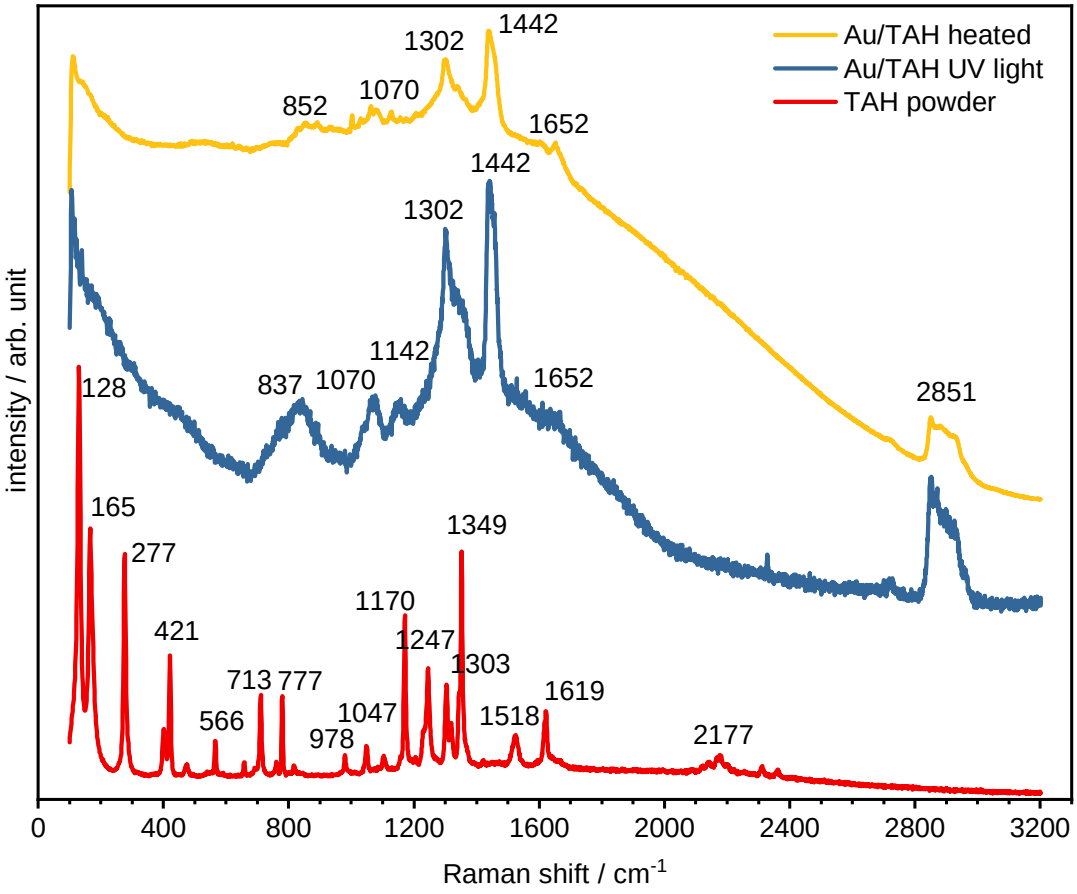

Figure 4.21. Raman spectra of TAH powder and polymerization products either by light or heat-induced reaction, measured with 785 nm laser excitation.

Our TAH-based carbon nitride Raman signals can be compared to carbon nitride nanosheet spectra by Jiang et al. [87] who prepared nanosheets from melamine. They found the heptazine vibrational modes at 543 cm^{-1} (in-plane vibration) and 705, 751 cm^{-1} (both out-of-plane vibration). Also in our case, the TAH powder showed blue-shifted signals at 566, 713, and 777 cm^{-1}. After both reactions, these contribution convoluted to one broad signal at 837 and 852 cm^{-1} respectively. This blue-shift suggest a material contraction, however further research is needed to confirm this hypothesis. Jiang et al. [87] attributed a further blue-shift of the sp^2 bending vibration, from 1234 to 1250 cm^{-1} to the difference between bulk and single layer carbon nitride.[87] Therefore, the peak position of 1302 cm^{-1} that we observe,

suggests single-layer coverage for our samples. This is supported by the very little signal contribution at 1481, 1555, and 1616 cm^{-1} as these represent crystalline bulk vibrations.[87]

In order to study further the structural differences between the light and the heat induced reaction, UHV-STM was used to image the polymer morphology after photoreaction. TAH molecules were vapor-deposited on Au(111) for 2 min and illuminated with UV light for 30 min at 110 K in UHV conditions. Figure 4.22a shows the STM image of the carbon nitride film. A higher surface coverage is observed than previously for the thermally activated samples. This can be explained by the absence of multilayer desorption prior the reaction. Besides domains of ordered flat-lying carbon nitride (see Image inset), novel, standing-up aligned molecule structures are found throughout the sample giving rise to linearly stacked molecule arrays. The lateral extension of these structures suggests already a partial heptazine linkage while the increased height seems to indicate an upright orientation, i. e. a binding via the linking nitrene nitrogen atom directly to the surface. This seems to reduce the photoreactivity of the remaining azide groups, as not all react off (see TPD in the following). Such nitrene-surface species have been proposed before.[89] The height profile shows the difference between a flat heptazine unit, as observed before and the standing molecule. The height difference of 0.09 nm suggests a total height of 0.25 nm for a standing molecule. This is much less than the expected ~0.8 nm of a heptazine diameter, but electronic effects might have a strong impact on the STM height.

The sample in Figure 4.22a was heated to 573 K. The gaseous products were again detected by mass spectrometry (see Figure 4.22b). However, it was not possible to measure the TAH mass 78 amu, as the signal intensity was too small. The nitrogen signal shows a similar curve as without previous UV irradiation, but with lower intensity by a factor of 3. The signal onset was shifted to higher temperatures compared to the sample without light exposure. This suggests that a part of second layer TAH molecules has already reacted. The reaction peak of the nitrogen signal at 460 K however, has the same shape as before. Here, still the same reaction seems to take place, even if the molecules have a different orientation. This is evidenced by STM measurements after the heating, which revealed a similar film morphology as observed with the heated-only sample in Figure 4.20. It seems the UV irradiation at 110 K forms a reaction intermediate. The upright orientation of the molecules requires sufficient energy to overcome the surface physisorption and hence a surface-bond appears likely. The gold-bound species is expected to be a nitrene, which is formed after the photolysis. This was observed before for other transition metals like copper.[89] A further discus-

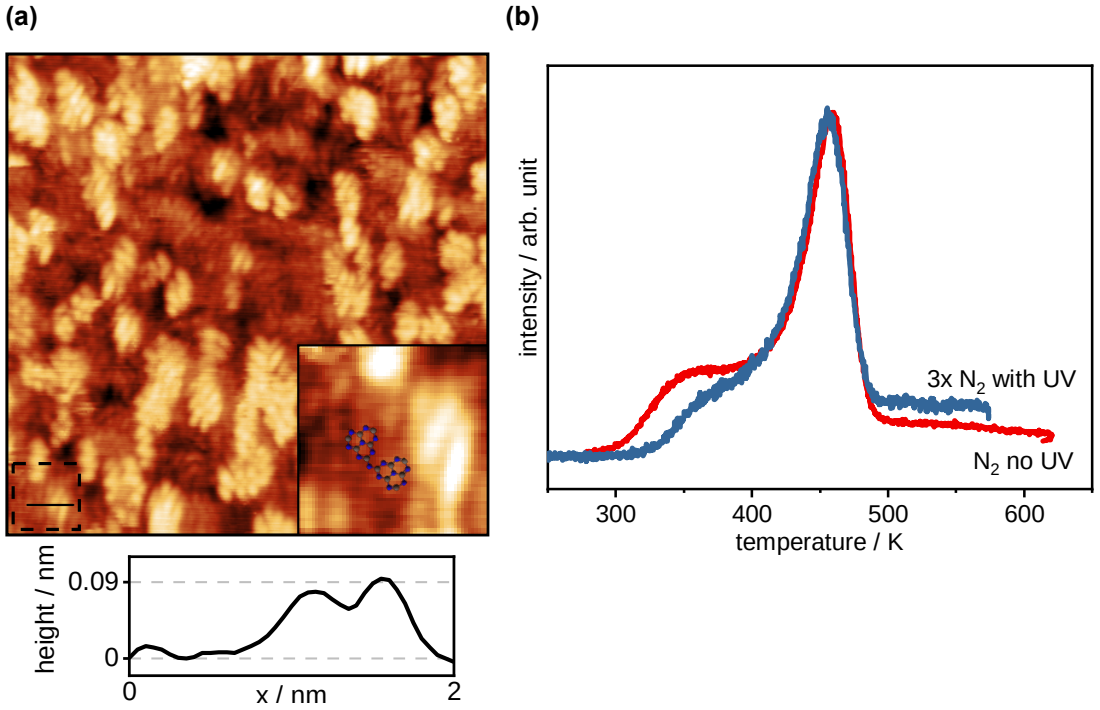

Figure 4.22. **(a)** UHV-STM image of TAH supported on Au(111) after 30 min UV light (365 nm) exposure at 110 K. The measurement was performed at room temperature. The inset shows a molecular structure of two flat-lying linked heptazine units. The line profile shows the height difference between flat and standing heptazine molecules. **(b)** The sample was heated to 573 K after the STM measurement. The ■ signal shows the nitrogen intensity in the mass spectrometer with previous UV light exposure and the ■ trace without light treatment.

sion about the metal bond with nitrenes is given in Section 4.3. The coincident polymerization onset in Figure 4.22b suggest that the kinetic barrier is not changed by the intermediate formation. This implies that the azide activation is the rate-determining step.

X-Ray Induced Reaction

In XPS, the supported TAH showed a reduced azide content already directly after the deposition. The loss of about one azide group out of three can be explained by the x-ray beam damage during the first spectrum. Figure 4.23 shows the decrease of the azide signal with ongoing x-ray irradiation. One azide group per TAH remains intact after the prolonged x-ray light exposure. This was observed for both, the liquid- and vapor-deposited sample. The partially decomposed TAH remains stable over night under UHV conditions. The linking amine contribution did not follow a systematic trend. As described earlier, in the case of a perfect network formation, the linking amine content would follow the inverse trend of the azide content (Figure 4.23b) and

finally reach the value 1 in Figure 4.23c. The deviation from the expected behavior can be explained by the low XPS signal-to-noise ratio, a result of the pass energy of 20 eV and short measurement duration.

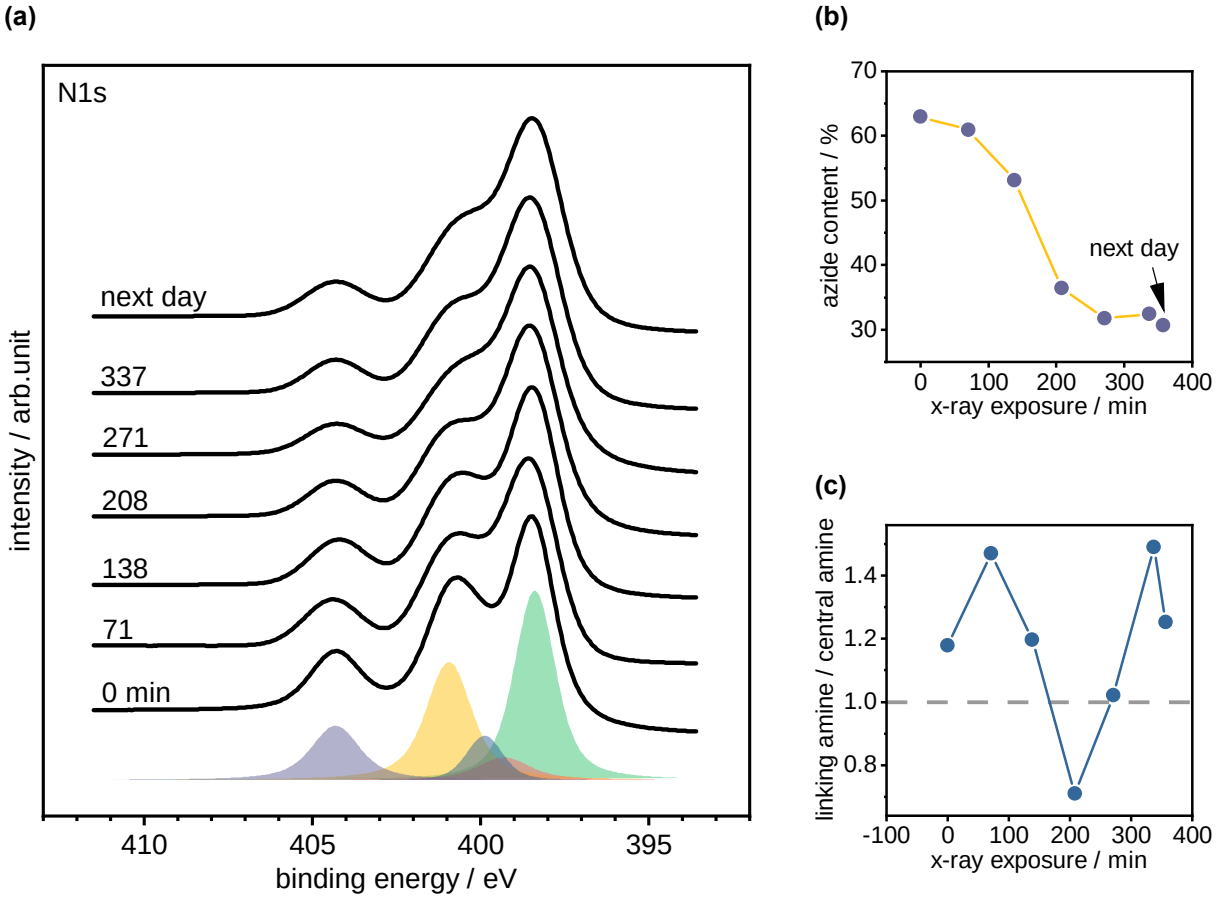

Figure 4.23. X-ray photoelectron spectra of TAH liquid-deposited on HOPG from a benzene solution. **(a)** The N1s signal is observed over x-ray exposure time. The black lines represent the fit result with the color-coded contributions, which refer to Figure 4.16. The raw data is not shown for clarity. **(b)** The azide (■, ■) contributions decay with ongoing x-ray exposure. **(c)** The ■ linking amine content did not increase in the same systematic way as the azide decomposition occurred. The dashed, horizontal line shows the expected content for a full network formation.

4.3. Metal Bond with Unsatisfied Octet Atoms

The STM measurements in Section 4.2.3 indicated a vertical surface-bound nitrene intermediate. We had the chance to have a glimpse on a related, molecular system, in order to explore a metal bond to an isoelectronic carbene by XPS. A novel octanuclear *N*-heterocyclic carbene complex class was introduced by Altmann and Pöthig [126]. This pillarplex molecule consists of two calix[4]imidazolium[2]pyrazole[127] ring-shaped

ligands, which are bridged with eight silver or gold atoms (see Figure 4.24a). The ring shape structure allows the intercalation of a linear guest molecule. Such host-guest interaction has received sustained interest for e. g. biological sensing, drug delivery, or catalysis.[128] The use of a spatial confined catalyst, which includes a specific site of for a certain intermediate can facilitate the product selectivity. The carbon dioxide reduction reaction e. g. described in Section 5 requires well adjusted CO binding site, as a molecular cavity can offer, were retention times are sufficiently long that multi-electron transfers can occur.[129]

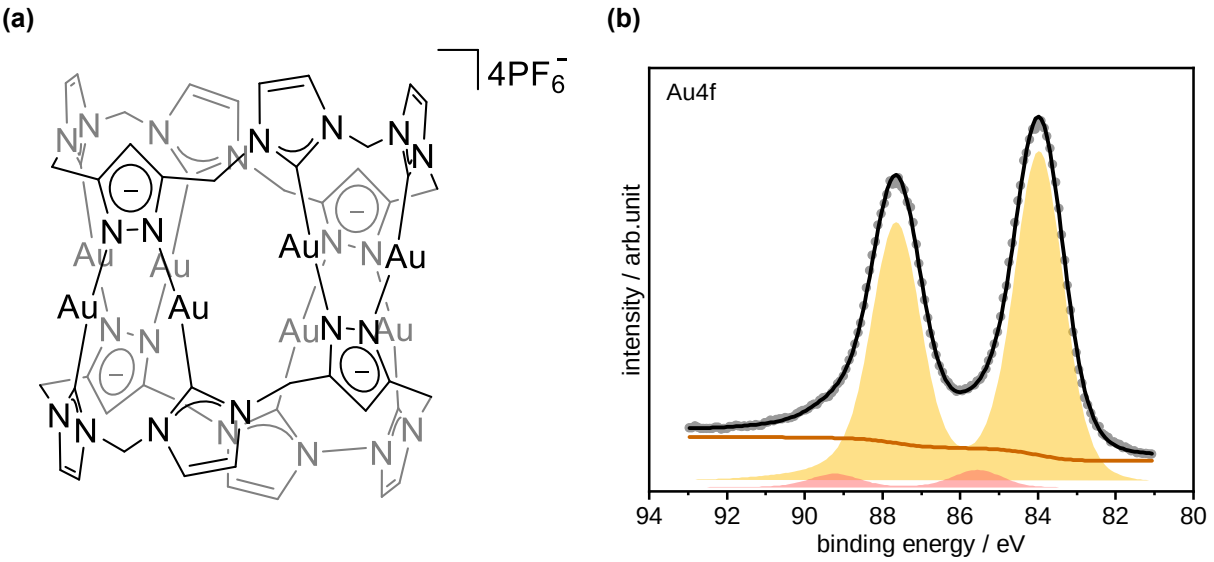

Figure 4.24. **(a)** Au–pillarplex structure with two carbene ligand rings bridged via eight gold atoms. Reprinted with permission from P. J. Altmann, A. Pöthig, *Journal of the American Chemical Society* **2016**, *138*, 13171–13174. Copyright 2016 American Chemical Society. **(b)** XPS spectra of Au-pillarplex drop-casted on Au(111) surface reveals shifted gold contribution from the pillarplex. **(b)** The Au4f signal of the ■ Au(111) surface and the ■ Au-pillarplex. The latter is shifted to higher binding energies, because of the oxidation state +I.

The pillarplexes were drop-casted on Au(111) from an aqueous solution and studied with XPS. Figure 4.24b reveals the Au4f pillar contribution shifted by 1.5 eV to higher binding energies. This aligns well with the +I oxidation state of the eight gold atoms in the pillarplex.[126] The measurement of the Au4f signal shows that the carbene-bound gold species can be identified even on a gold surface. This paves the way to further study the found nitrene intermediates in Section 4.2.3 with XPS analysis.

5. Influence of Support on Gold Nanoparticle Dynamics

Contributor Roles

Nicolas Bock: Investigation, Visualization, Writing
Jaime Aviles Acosta: Investigation, Visualization
Christopher Hahn: Conceptualization, Supervision, Funding acquisition
Thomas Jaramillo: Funding acquisition, Resources
Ueli Heiz: Funding acquisition
Friedrich Esch: Funding acquisition

The chemical pathways towards the production of renewable chemical feedstock described in section 1 include the activation of CO_2, which occurs as a byproduct of current high-scale petrochemical reactions and as an end-product of carbon fueled combustion processes. The chemical portfolio which can be derived from CO_2 is manifold and includes CO, CH_3OH, or C_2H_x. However, the hydrogenation of CO_2 with thermal catalysis is energetically demanding, and even a selective hydrogenation, which would allow for the generation other products apart from CH_4, remains challenging.[130] Especially C_2H_x-products such as ethane, which could substitute natural gas, are only accessible through electrochemical reduction.

The first step in the electrochemical transformation of carbon dioxide into any product is the CO_2 reduction to CO ($CO_2 + 2H + 2e^- \longrightarrow CO + H_2O$). In various catalyst systems a possible subsequent reaction can lead to a further transformation of CO. In general, metal catalysts can be divided into four groups depending on their main reduction product: H_2, CO, $HCOO^-$, and $>2e^-$ products.[131] All carbon-containing products apart from CO rely on adsorbed CO for further reaction. This multi-step reaction challenges the catalysts to match the adsorption energies of all involved reaction intermediates so that there is high chemical turnover without catalyst poisoning. Although the full reaction mechanism is not completely understood at this point, the binding of CO as an intermediate after the first reaction step is known to play a crucial role. If the CO-catalyst binding is weak, CO will desorb without further reaction. A high binding energy, on the other hand, could lead to a full coverage with CO and therefore poison the active sites if no further reaction is possible. Understanding fundamental catalyst phenomena helps to provide insights into the

complex processes that this multi-step reaction is composed of. This work focuses on the crucial catalyst-support interaction in order to understand the aggregation of the catalyst during the first CO-producing reaction step. A gold catalyst is used because it almost exclusively produces CO under reaction conditions.

Materials like carbon black, glassy carbon (GC), or highly oriented pyrolytic graphite (HOPG) have shown great potential as a support for electrocatalysis. These carbon based materials are conductive, electrochemically and pH inert in a wide range, and easily accessible. Although they are widely used in electrocatalysis, e. g. in hydrogen fuel cells[132] or methanol fuel cells,[133] the essential catalyst-support interaction remains opaque. It is necessary to understand the electronic and structural properties of the interface in order to achieve a further improvement of the catalyst performance. In this work, both glassy carbon and HOPG were used as a support for nanoparticles. HOPG is atomically flat and hence ideal for SPM methods, but its limited surface-to-volume ratio makes it less suitable for integral electrochemical tests. Glassy carbon provides the same chemical sp^2 state of the carbon atoms as HOPG, but comes with a bally fullerene-type structure which is prone to more defects and oxygen heteroatom termination at its boundaries.[134]

The gold nanoparticles were prepared by means of *ex situ* thermal vapor deposition (see experimental section 2.4.1). The resulting deposition was confirmed to be uniform with scanning electron microscopy images (SEM) (see Figure 5.2a). A particle detection routine helped to quantify the particles in the SEM images.[a] Figure 5.2e shows the surprisingly narrow distribution of the obtained nanoparticle sizes, given that no size filter was applied during the deposition. This is very important as a previous study by Pattadar and Zamborini [136] found that smaller nanoparticles and higher coverages lead to an increase in the Oswald-ripening rate. That is, the size of the nanoparticles affects their electrochemical equilibrium potential.

5.1. Nanoparticle Dynamics during CO_2 Reduction Reaction

Gold nanoparticles supported on glassy carbon were used to examine the particle-support interaction during the electrochemical CO_2 reduction reaction (CO_2R) which was driven at potentials below –0.65 V vs RHE in a CO_2 purged $KHCO_3$ electrolyte.

[a] Used software for particle analysis: Gwyddion 2.53 by Nečas and Klapetek [135].

Previous studies by Manthiram, Surendranath, and Alivisatos [137] show that a negative polarization of dodecanethiol-capped Au catalysts in electrochemical conditions leads to an aggregation of the nanoparticles. Thiol-capped nanoparticles are known to stabilize catalysts in reductive conditions like HER and prevent ripening processes. Figure 5.1a shows SEM images of the Au nanoparticles supported on glassy carbon. The CO_2R catalyst was exposed to several negative polarization times at –1.2 V vs RHE in 0.1 M $NaHCO_3$ electrolyte. The nanoparticles with an initial diameter of 3–5 nm increase in size throughout the reaction and formed large dendritic structures after a few minutes.[137]

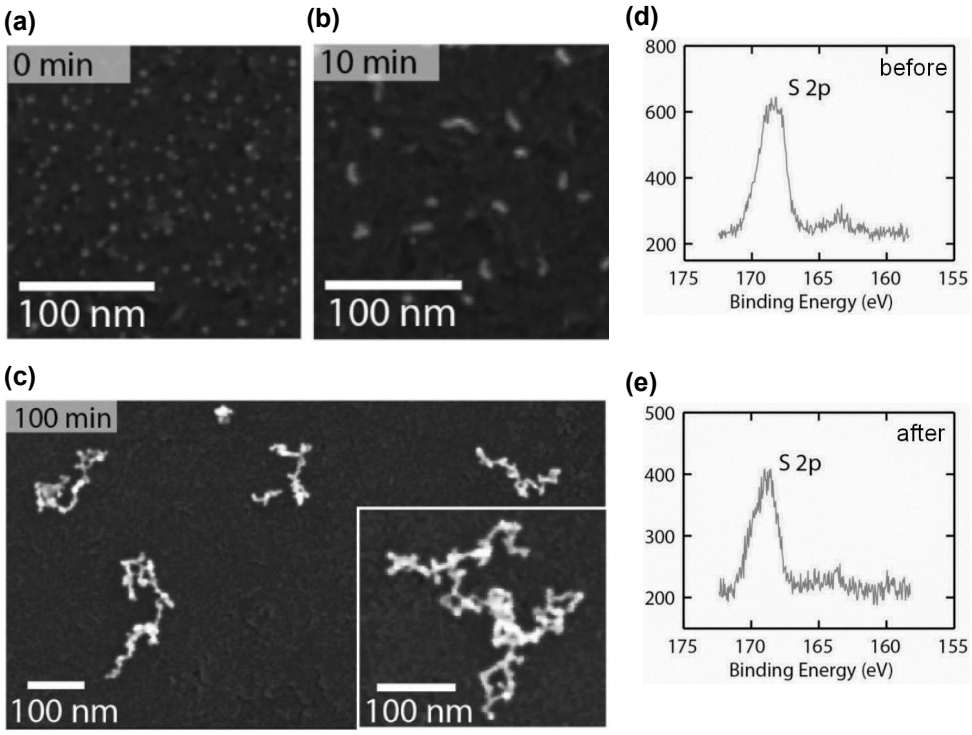

Figure 5.1. SEM images of Au nanoparticles **(a)** before and after **(b)** 10 min and **(c)** 100 min exposition to a negative polarization at –1.2 V vs RHE in 0.1 M $NaHCO_3$ buffer shows an aggregation of the particles in dendritic structures. **(d)** The XPS S2p spectra reveals, that the dodecanethiol for the nanoparticle stabilization is chemically bound to the gold. **(e)** After the chemical exposure to reductive potentials, the thiol species remains only physisorbed after the thiol-gold bond is ruptured below –0.6 V vs RHE. **(a–e)** Reprinted and adapted with permission from K. Manthiram, Y. Surendranath, A. P. Alivisatos, *Journal of the American Chemical Society* **2014**, *136*, 7237–7240. Copyright 2014 American Chemical Society.

Manthiram, Surendranath, and Alivisatos [137] were able to model the particle aggregation with a simple random walk model, which shows that the aggregates remained mobile on the surface. Possible reasons for the particle movement might be brownian motion, gas bubble formation, or electric field effects. However, the exact

aggregation mechanism remains unclear, especially since the dodecanethiol-gold bond cleavage below −0.6 V vs RHE influences the chemical potential of the particle and therefore the observed aggregation. Interestingly, approximately two thirds of the thiol species stays physisorbed on the gold nanoparticles or the glassy carbon support after the rupture of the chemisorption bond between gold and the thiol ligand (see XPS spectra before and after polarization in Figures 5.1d–e). The remaining dodecanethiol influences the aggregation process more than dodecylamine, which is attributed to dodecylamine's higher solubility in water. This shifts the equilibrium between physisorption and solvation towards the latter.[137] In order to disentangle the effect of the chemi-/physisorbed thiol molecule from the bare catalyst-support interaction, the aggregation of unmodified gold nanoparticles on modified surfaces is studied.

5.1.1. Influence of Reaction Overpotential on Aggregation

Figure 5.2a shows an SEM image of a freshly deposited Au particles on glassy carbon. Besides the uniformly distributed gold nanoparticles, there is also some residue from the AlOx polishing suspension in form of large spherical particles. After switching to a diamond based polishing suspension and electrochemical cleaning cycles before deposition (see section 2.4.1), these impurities did not reappear in SEM images and XPS spectra. Figure 5.2b – 5.2d shows a series of images of freshly deposited gold particles exposed to various reductive potentials for 5 min. The dendritic structures, which are known be built after negative surface polarization, were observed here as well, while the small gold nanoparticles disappeared. The aggregation is strongly dependent on the applied overpotential, as previously reported by Manthiram, Surendranath, and Alivisatos [137]. The quantitative analysis of the particle areas suggests a sigmoidal trend with increasing overpotential. The highest increase in area occurred at a potential of −1.3 V vs Ag/AgCl. At −1.6 V vs Ag/AgCl, the average particle area seems to saturate at 250 nm^2. The total gold area in the SEM images decreased with further aggregation. The sample exposed to −1.6 V vs Ag/AgCl retained only 88 % of the gold area after deposition, which suggests an increase in height of the aggregates, given that further quantitative XPS measurements found a constant gold content on the surface.

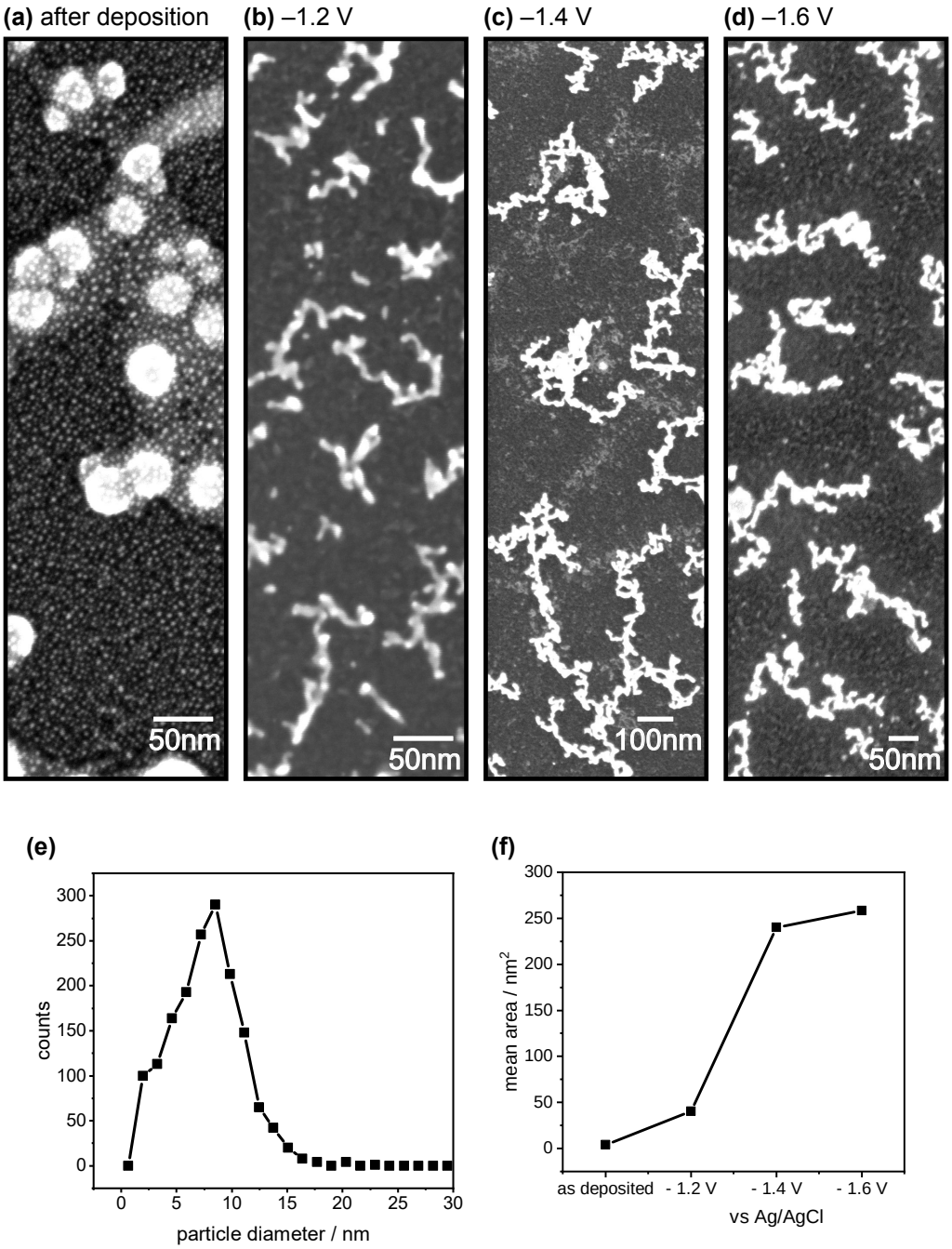

Figure 5.2. SEM image of Au nanoparticles on glassy carbon **(a)** directly after deposition with **(e)** a narrow particle diameter distribution and an average particle size of 8 nm. **(b – d)** –1.2, –1.4, and –1.6 V vs Ag/AgCl were applied for 5 min, respectively. Dendritic structures were formed, **(f)** which increased in size with higher overpotential until an area plateau at around 250 nm^2 was reached. SEM data was measured by Aviles Acosta [138].

5.1.2. Chemical and Structural Catalyst Changes

In addition to the structural catalyst properties, also the chemical nature of the supported particle is important to understand the catalyst system. Figure 5.3d shows the x-ray photoelectron overview spectrum of the gold nanoparticles deposited on GC. Carbon (74 %), gold (12 %), and oxygen (15 %) were found in the freshly prepared sample.

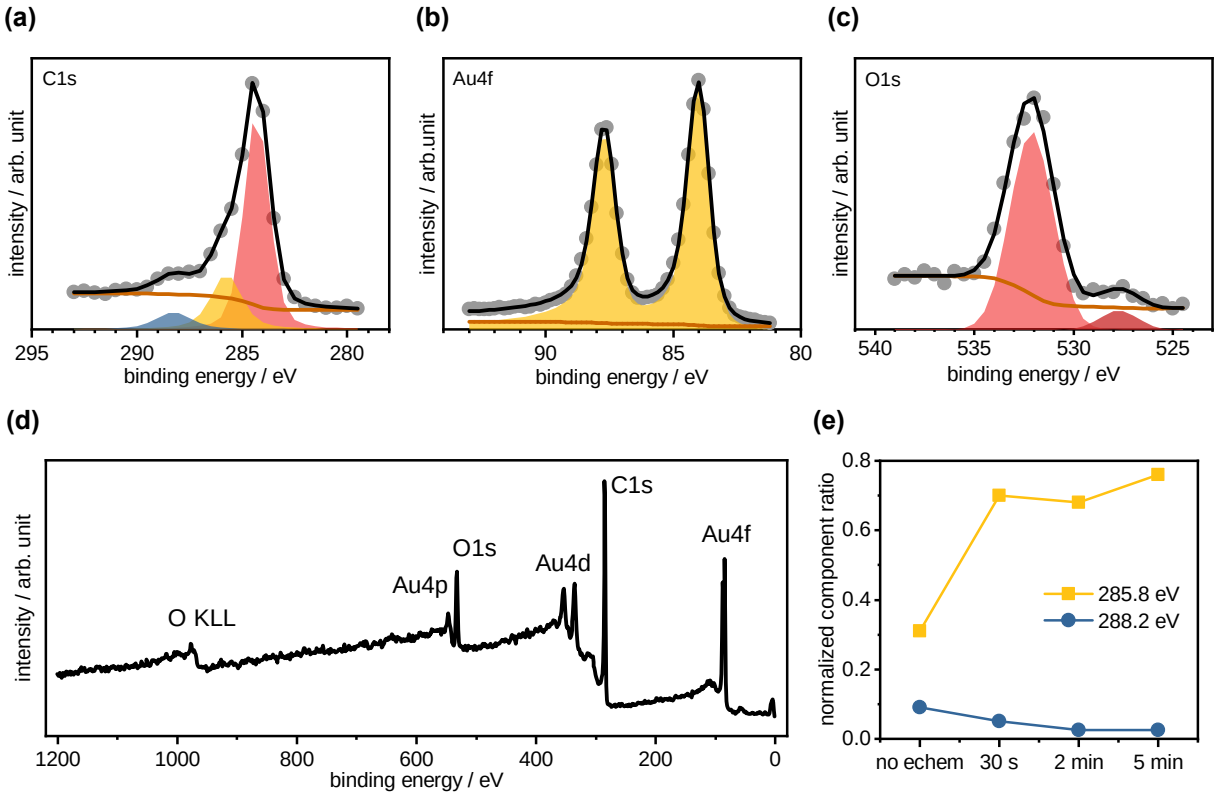

Figure 5.3. X-ray photoelectron spectra with fitted Voigt signal contributions of a glassy carbon sample with freshly deposited gold: **(a)** C1s signal with contributions from ■ glassy carbon sp^2, ■ ketone, and ■ ether groups which can be attributed to adventitious carbon or surface terminating groups. **(b)** The Au4f signal suggests that the gold nanoparticles are in the metallic state. The signal is slightly asymmetric, which is known for transition metals and therefore fitted with Doniach-Sunjic functions instead of Voigt. **(c)** The O1s signal intensity is in good agreement with the oxygen-containing carbon groups found in the C1s signal. The second signal contribution at lower binding energies can be attributed to hydroxyl groups. **(d)** Overview spectrum with carbon signal (74 %), oxygen (15 %), and gold (12 %). **(e)** During the CO_2 reduction at –1.0 V vs Ag/AgCl with different reaction durations, the ketone content decreased and more ether groups were formed. The Shirley background is shown in ■.

Figure 5.3a shows the carbon 1s signal (C1s) which consists of three components. The peak contribution at 284.3 eV can be attributed to the sp^2 carbon from the GC.[104] All spectra were shifted to match this value in order to compensate for the

work function of the studied sample. The signal at 285.8 eV is a convolution between the asymmetric peak shape of the sp^2 carbon species[139] and ether groups (C–O–C). However, as no $\pi \rightarrow \pi^*$ transition was observed as a shake-up satellite at 291 eV, the asymmetry of the glassy carbon sp^2 species is expected to be not significant and is therefore not further considered.[139] The contribution at 288.2 eV results from a ketone (C=O) group. These two additional ether and ketone contributions to the GC signal are known to occur for samples that were exposed to atmosphere and are hence contaminated with adventitious carbon.[103] Another possible explanation is that the GC surface itself contains ketone and ether groups. These can be introduced by the electrochemical cleaning cycles, which were performed before the deposition.[140] The electrochemical CO_2 reduction accompanied by the strongly negative surface polarization can influence possible surface functionalizations. Figure 5.3e shows the content of the two C–O species normalized to the sp^2 carbon signal. The ketone contribution was reduced with prolonged reduction time, while the ether group increased in signal intensity. The underlying mechanism of these surface changes is unknown at this point, but it seems most likely that the surface itself contains ketone and ether groups as the adventitious carbon impurity is introduced after the electrochemical treatment. Further studies are needed to investigate whether the surface shows a hysteresis after the cleaning cycles. In order to disentangle the two additional contributions, *in situ* XPS analyses of the GC samples are required where no adventitious carbon is present. The two carbon species also explain the large peak of the oxygen 1s (O1s) signal at 532.1 eV in Figure 5.3c. The additional species at 527.7 eV is known to occur for hydroxyl groups.[141] However, this feature was not found in any other GC sample and is therefore most likely an impurity of this specific sample. Figure 5.3b shows the gold 4f (Au4f) signal of the gold nanoparticles in the metallic state.

The chemical composition of carbon shown in Figure 5.4a did not change significantly throughout the reduction reaction. Since a different sample from the same deposition batch was used for each measurement time, minor changes in gold intensity can be a result of small deviations in the amount of deposited gold. Also, a variation of the adventitious carbon impurity introduced during the sample transfer to vacuum conditions can dampen the gold signal. This could also explain the variations in the oxygen signal, although a clear trade-off between adventitious carbon and gold signal reduction was not observed. However, the gold nanoparticles remained on the surface and also the oxygen-carbon groups seem to be stable at the applied reductive potential.

In order to study the kinetics of the aggregation mechanism, the temporal evolution of the particle size after reaction conditions was investigated with SEM. A reduction potential of –1.0 V vs Ag/AgCl was chosen to avoid a saturation of the aggregation size. This potential marks the onset of the aggregation according to the trend observed in Figure 5.2f. The gold particle diameter distribution after 30 s, 2 min, and 5 min of reductive polarization extracted from an SEM image analysis is shown in Figure 5.4b. Interestingly, only few changes were observed after 30 s of reduction reaction. After 2 min, the particle diameter distribution had broadened. The distribution after 5 min did not differ significantly from the 2 min sample. This suggests a saturation of the aggregation at this overpotential. Due to varying contrasts in the SEM images, the particle detection can contain a certain error.

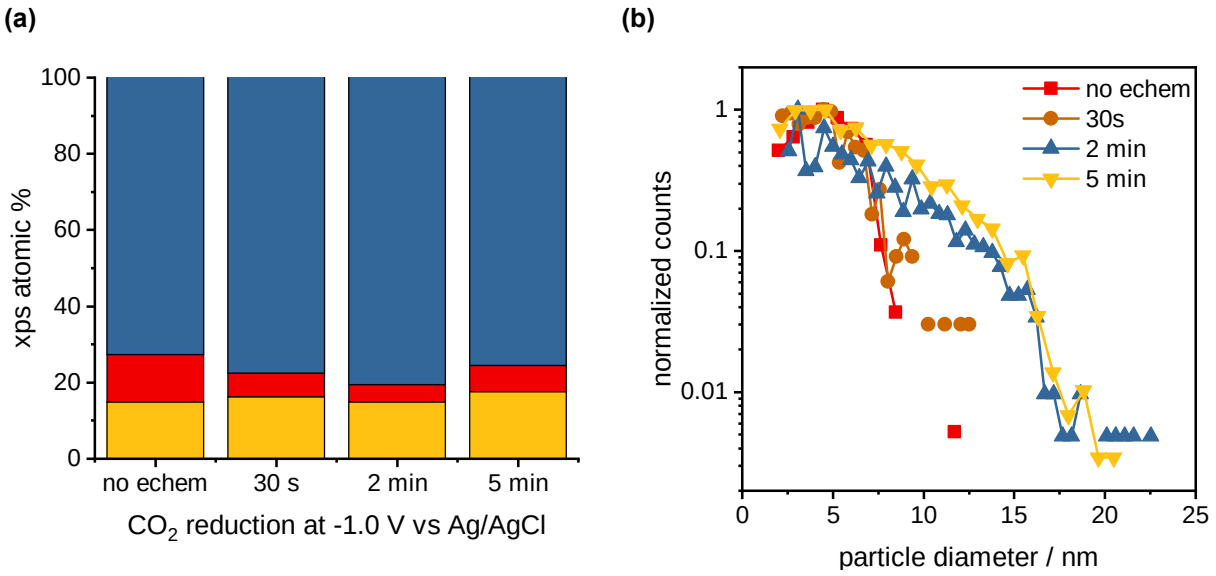

Figure 5.4. Gold deposited on glassy carbon and exposed to the CO_2 reduction reaction at –1.0 V vs Ag/AgCl for different amounts of time: **(a)** Atomic composition of ■ carbon, ■ oxygen, and ■ gold obtained from XPS after different electrochemical conditions. The gold and oxygen-containing groups were not significantly altered during the reductive conditions. **(b)** Particle diameter distribution of untreated, pristine glassy carbon sample after 30 s, 2 min, and 5 min of reductive polarization at –1.0 V vs Ag/AgCl in comparison with the diameter distribution of glassy carbon without applied electrochemistry.

5.1.3. Support Morphology Influence

Another important factor in the possible aggregation, besides the chemical state and the catalyst structure, is the morphology of the support. Better insights into the topography of the carbon surface can be gained by applying atomic force microscopy (AFM). The intrinsic roughness of glassy carbon can potentially provide a link between the

particle dynamics and the surface morphology. Figure 5.5 shows AFM measurements before and after the reductive surface polarization including the non-contact AFM phase signal which emphasizes the chemical contrast and helps to identify the location of the gold nanoparticles. While the particles were well dispersed before the reductive surface polarization, aggregate structure are formed after applying –1.0 V vs Ag/AgCl. The aggregates can be found in the pits of the corrugated glassy carbon substrate. This finding highlights the importance of considering the support morphology when investigating aggregation mechanisms.

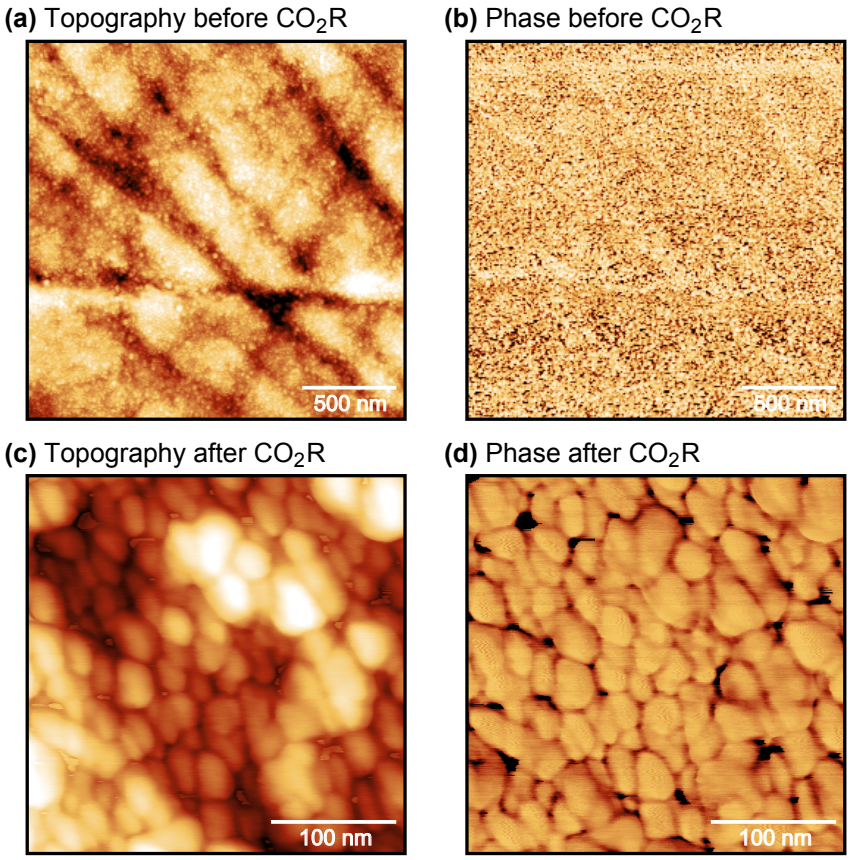

Figure 5.5. Atomic force microscopy images of gold nanoparticles deposited on glassy carbon **(a)** before the exposure to electrochemical conditions and **(c)** after CO_2 reduction at –1.0 V vs Ag/AgCl. **(b, d)** Images of the respective phases of the measurement emphasize the chemical contrast and therefore the gold nanoparticle sites which appear in black.

5.2. Strategies for Tuning Interface Properties

The morphology and the chemical state of the support play a major role in the stabilization of catalysts. The carbon support used in this project allows for the modification of the surface terminating groups, which influences the binding sites of the

nanoparticles. Two types of surface modification were applied in this study: (1) Partial oxidation of the carbon surface by oxygen plasma treatment and (2) the incorporation of sulfur heteroatoms.

5.2.1. Carbon Surface Oxidation

One well-established approach to modify carbon catalyst supports is an oxygen plasma treatment which introduces defects and leads to a surface termination with oxygen-containing groups.[142] The oxygen plasma treatment introduces several changes, one of which affects the chemical state. This does not only influence the catalyst binding itself, but also alters the wetting with electrolytes. A previous report has shown that an oxidation of the carbon support can increase the activity of HER catalysts because of the improved wetting of the catalyst surface.[143] Besides the chemical change, also the morphology changes drastically. Figure 5.6a shows the glassy carbon surface after 10 min of oxygen plasma treatment and the deposition of the gold nanoparticles. The oxygen plasma was created in a Diener *Pico* setup. The surface appears to be more corrugated than pristine glassy carbon, which indicates an oxidation of the surface with CO_2 release. This is in agreement with previous glassy carbon oxidation with electrochemical methods.[140] AFM measurement attempts revealed that the surface was interacting with the tip, which is usually a sign of weakly bound adsorbates, such as delaminated carbon flakes.

In order to study the morphological changes introduced by the plasma treatment, HOPG (mosaic spread angle was $0.4° \pm 0.1°$)[144] samples were exposed to oxygen plasma for 1 s. Note that the plasma exposure time is not comparable to the sample investigated with SEM, as the oxygen plasma was created in a Schlenk flask filled with 0.4 mbar oxygen gas and ignited with 900 W in a conventional household microwave oven. The resulting HOPG surface was covered with mobile species and an imaging was first possible after a thermal cleaning step at temperatures above 450 K. Figure 5.6b shows an STM image of the sample which was annealed after the plasma treatment at 923 K for 1 min. This temperature is known to further grow the initial pits.[145] Besides the randomly distributed holes, residual graphene flakes were observed. The largest pit showed a step height of 0.4 nm, which is larger than one HOPG step with 0.35 nm. Because of the large STM tip dimensions compared to the small pit, a full penetration of the tip into the hole is not possible and STM might underestimate the height. Therefore a hole depth of at least two HOPG step heights can be expected. The higher corrugation of the plasma-treated samples can hinder the particle aggregation and should therefore be considered when studying particle dynamics.

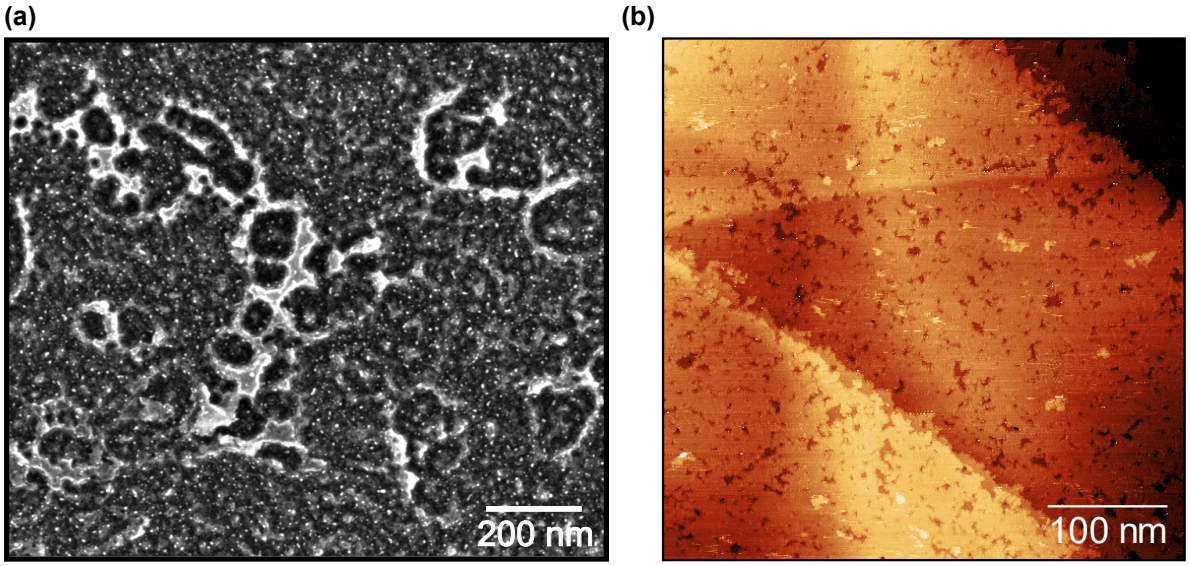

Figure 5.6. Surface modifications introduced by the oxygen plasma treatment. **(a)** SEM image of 10 min oxygen plasma treated glassy carbon sample with deposited gold nanoparticles. The surface was roughened by the treatment due to partial decomposition of the glassy carbon surface. The image was measured by Aviles Acosta [138]. **(b)** An HOPG was exposed to 1 s of oxygen plasma, followed by a 1 min annealing step at 923 K. The HOPG surface showed pit formation and step edge etching.

The chemical composition of glassy carbon was expected to change with the oxygen plasma treatment. Indeed the O/C-ratio increased by a factor of almost two from 0.44 to 0.81 as a result of the exposure to plasma. Figure 5.7c shows the O1s signal with one oxygen species at 532.1 eV. While this signal is identical in position to the untreated GC sample, it is slightly broader in LORENTZ width, which is an indication of overlapping oxygen components. The C1s signal contains the same three components from sp^2, ketone, and ether groups. Surprisingly, the C-sp^2-normalized ratio of the two oxygen-containing groups was similar to the one of the untreated sample (in parentheses): 0.39 (0.31) ether and 0.15 (0.09) ketone. This poses the question whether the adventitious carbon masked the underlying carbon species. Figure 5.7b shows the Au4f signal, which suggests one gold nanoparticle species.

During the electrochemical CO_2 reduction at −1.0 V vs Ag/AgCl, the higher oxygen signal remained stable for 5 min and was slightly reduced after 20 min (see Figure 5.8a). Therefore, the oxygen-containing groups were expected to be stable over the course of the reduction reaction. Interestingly, the gold signal decreased during all three electrochemical measurements. The reduced Au4f signal could be explained by gold etching or partial delamination of the glassy carbon surface with bound gold nanoparticles, but this would also result in a reduction of the O1s signal.

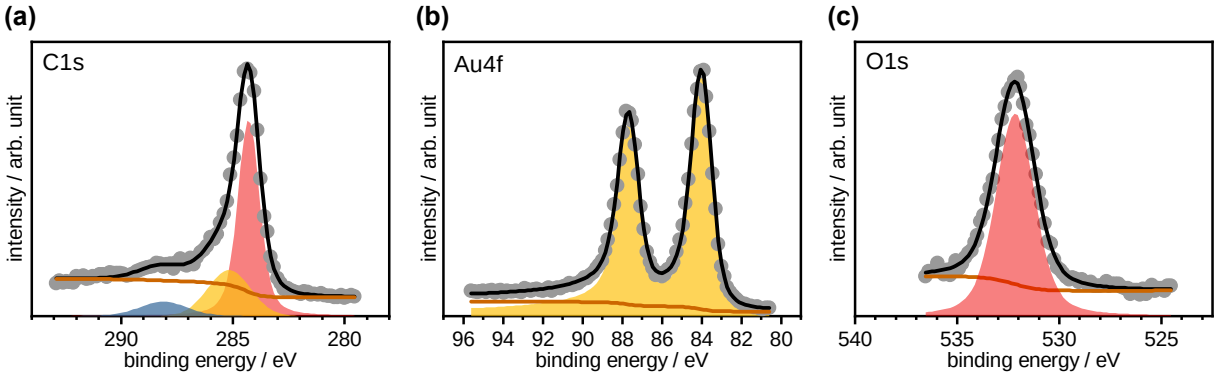

Figure 5.7. X-ray photoelectron spectra with fitted Voigt signal contributions of a plasma treated glassy carbon sample with subsequent gold nanoparticle deposition: **(a)** C1s signal with contributions from ■ glassy carbon sp^2, ■ ketone, and ■ ether groups which can be attributed to adventitious carbon or surface terminating groups. (**b**) The Au4f signal suggests that the gold nanoparticles are in the metallic state. The signal is slightly asymmetric, which is known to occur for transition metals and is therefore fitted with Doniach-Sunjic functions instead of Voigt. **(c)** The O1s signal intensity is in good agreement with the oxygen-containing carbon groups found in the C1s signal. The Shirley background is shown in ■.

It is more likely that the gold nanoparticles changed their structure during the reaction and increased in height. The penetration depth of the x-ray beam only reached the top 2 nm of the material which is why the complete nanoparticle might not be detected.[146] The height change of the gold nanoparticle instead of an actual decrease in total gold amount is supported by the reduction current of −11.33 mA after 60 s at −1.0 V vs Ag/AgCl, which is almost 80 times higher compared to the untreated sample (−0.148 mA after 60 s). A higher activity of plasma-treated samples was also observed by Sanchez et al. [143] who suggest that a better wetting improves the reaction turnover.

Figure 5.8b shows the gold nanoparticle diameter with progressing reaction at −1.2 V vs Ag/AgCl. The higher overpotential compared to the sample investigated with XPS, caused larger aggregates with a diameter of up to 130 nm. However, the trend of the aggregation was different from the untreated sample. While the nanoparticles on the pristine GC sample homogeneously increased in size, the gold particles on the plasma-treated sample showed a certain stability at their initial size. After 5 min, only a fraction of the Au had aggregated, which resulted in the local maximum at 40 nm. After 50 min, this shoulder in the distribution flattened and larger particles were formed. The majority of nanoparticles stayed at their original size, indicating a stabilizing effect for certain particles. As both the surface morphology and the chemical nature change, the exact mechanism for better particle binding needs further investigations with plasma-treated flat HOPG samples.

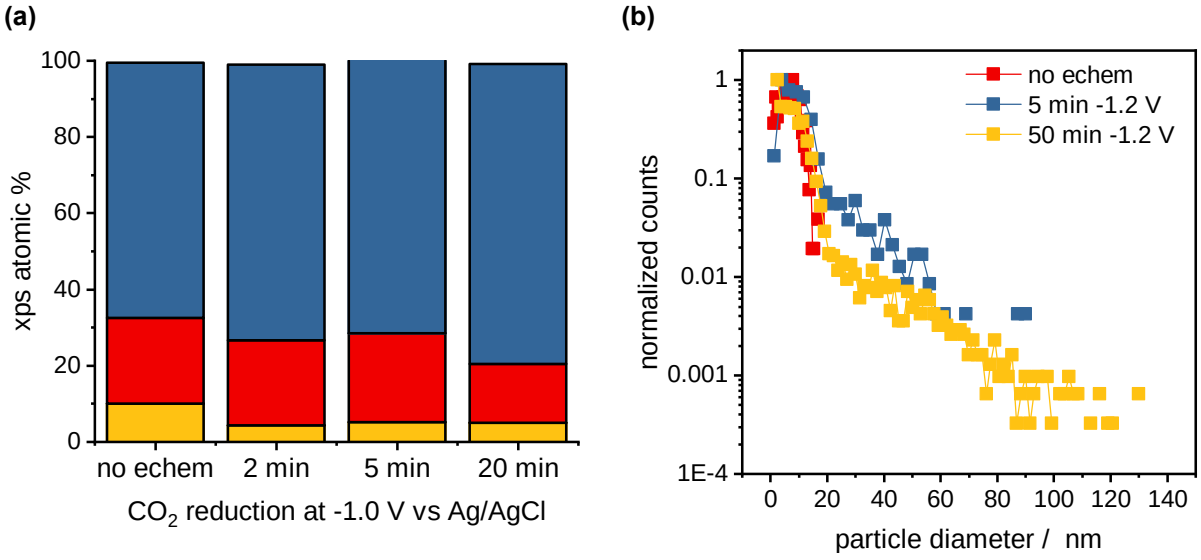

Figure 5.8. Oxygen plasma-treated glassy carbon sample with deposited gold nanoparticles used for CO_2 reduction. **(a)** Elemental composition of ■ carbon, ■ oxygen, and ■ gold extracted from XPS. The sample was exposed to 5 min of O_2 plasma before deposition and the applied reduction potential was –1.0 V vs Ag/AgCl. **(b)** Gold nanoparticle diameters extracted from SEM images show a stable regime at 15 nm throughout the whole reaction, while certain particles aggregate up to 130 nm in diameter. This sample was treated with 10 min of O_2 plasma and the applied potential was –1.2 V vs Ag/AgCl.

5.2.2. Introduction of Sulfur Binding Sites

The stabilization of metal nanoparticles with thiols has received sustained interest in the last two decades.[147] Especially for reactions with moderate reaction conditions, adding ligands can prevent the particles from aggregating. However, at very high overpotentials, which are used for the CO_2 reduction reaction, the thiol-metal bond is cleaved and the stabilization effect is reduced. Therefore, an electrochemically stable incorporation of sulfur in the support itself appears resonable. Several approaches, such as solvothermal synthesis of graphene in dimethyl sulfoxide,[148] thermal exfoliation of graphite oxide in the presence of sulfur-compounds,[149,150] and SO_2 / H_2O plasma applied on HOPG and GC[151] have previously shown to be successful in the doping of carbon materials with sulfur atoms. Here, we annealed the GC samples to 623 K for one hour under H_2S / H_2 gas flow. Figure 5.9d shows the S2p signal, which indicates the presence of 1.1 % sulfur on the sample. Although the $p_{1/2}$ and $p_{3/2}$ spin orbit splitting was expected for S2p electrons, it was not possible to properly fit the signal due to a low signal-noise ratio and overlaying species. The two contributions at 162.9 and 168.3 eV were therefore fitted with a Voigt function with large Gauss and Lorentz widths. These two sulfur components match the sulfate (168 eV) and

oligothiophenes species that are known from the literature, e. g. R–S–H and R–S–R (164 eV).[148] Poh et al. [150] reported a sulfur doping without sulfate contribution, suggesting that this species originates from a side reaction during the annealing process. Apart from the known adventitious carbon contributions, the C1s signal in Figure 5.9a reveals a new species at 286.9 eV, which could origin from an R–S–R species.[152] The oxygen and gold signals remained unchanged by the hydrogen sulfide annealing compared to the untreated sample.

Yang et al. [149] showed a successful annealing of graphene oxide in the presence of benzyl disulfide. They suggest that sulfur doping can be achieved by replacing the oxygen atom of an ether group with sulfur atoms. If this holds true, a higher concentration of oxygen-containing groups at the GC surface could increase the incorporation of sulfur. Therefore, an oxygen plasma treatment was applied to a GC sample which was subsequently subjected to the annealing process at 723 K in H_2S / H_2 gas flow for 1 h. Auger spectroscopy showed an increase in oxygen content which confirmed the introduction of oxygen-containing groups. Surprisingly, the oxidation of the surface remained stable during the annealing in reductive gas (see Figure 5.9f). Also, the measurement did not quantify a higher sulfur content. It has to be noted that the Auger signal might differ in signal intensity from the XPS measurement due to their respective surface sensitiveness.

The sulfur-doped sample was exposed to the electrochemical CO_2 reduction at –1.0 V vs Ag/AgCl for different reaction times and analyzed *ex situ* by means of XPS (Figure 5.10a) and SEM. The sample exposed to 30 s of reductive potential showed a high adventitious carbon content indicated by the large oxygen content. This led to charging problems during the XPS measurement. This carbon overlayer also explains the low gold nanoparticle signal for this sample, but a decrease in gold content was also observed for all other electrochemically exposed samples. In contrast to the oxygen-treated sample this aligns with a reduced current of –0.069 mA after 60 s (–0.148 mA for untreated sample). Again, the reduced Au4f signal is due to the increase in particle height caused by the aggregation. However, a sulfur species bound to the nanoparticle surface could potentially stabilize and facilitate the desorption of gold and explain the decrease in reduction current compared to the untreated sample. The sulfur contents decreased from 1.1 % to 0.6–1 %, whereas there was no sulfur found in the sample after 2 min of reaction time. Whether this decomposition occurs only in certain sulfur-species is investigated by means of the analysis of the two S2p components. Figure 5.9e shows the intensity ratio of the species throughout the reaction. While no significant change occurred after 2 min, the sulfate species surprisingly increased after 5 min of

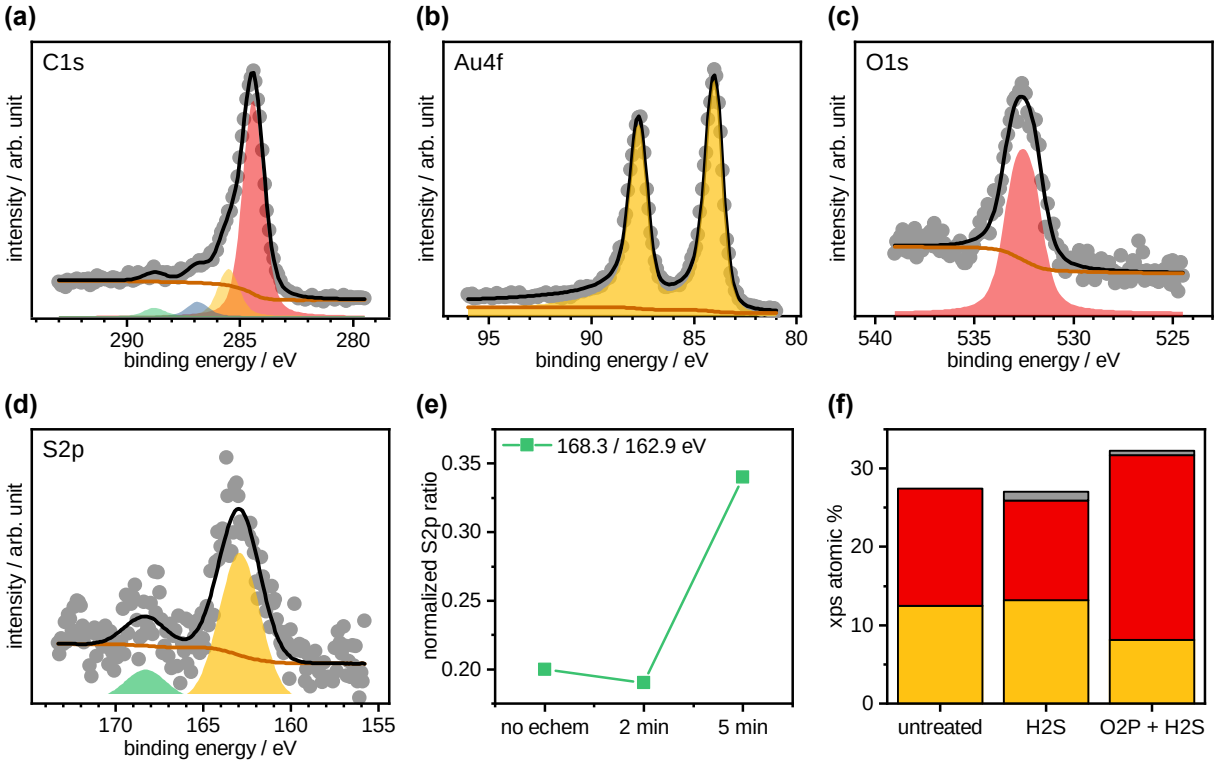

Figure 5.9. X-ray photoelectron spectra of GC sample annealed at 623 K in H_2S / H_2 gas flow for 1 h. **(a)** The C1s carbon signal shows an additional ■ species besides the known ■, ■ adventitious carbon and ■ glassy carbon contributions. **(b)** The gold signal shows the presence of metal gold nanoparticles. **(c)** The O1s signal is similar in comparison with the untreated sample, showing one oxygen species. **(d)** The presence of sulfur was confirmed by the two components in the S2p signal. **(e)** During CO_2 reduction the ratio of the S2p signals varies, however no clear trend is observed. **(f)** Atomic composition of ■ sulfur, ■ oxygen, and ■ gold result from XPS measurement. The oxygen plasma exposure before the H_2S annealing process did not result in a higher sulfur incorporation in the Auger spectrum of the GC sample.

reaction. The increase in the sulfur's oxidation state was unexpected, as the reaction potential would suggest a reduction.

The gold particle aggregation in Figure 5.10b is similar to the one exhibited by the untreated sample. There was no significant aggregation in the first 30 s of the reaction. After 2 min, the gold particles showed a systematic increase in diameter. A stabilization effect as observed in the oxygen plasma-treated sample did not occur. Possible reasons for that could be the shortage of sulfur sites in comparison to the amount of gold nanoparticles or an uneven distribution of the sites across the surface. In order to study the homogeneity of the introduced sulfur groups, a sample was treated with oxygen plasma, annealed with H_2S / H_2, exposed to 5 min of CO_2 reduction, and finally scanned using Auger spectroscopy. Figure 5.11 shows the area of this sample with gold and sulfur mapping. On the left side of the area the gold nanoparticles

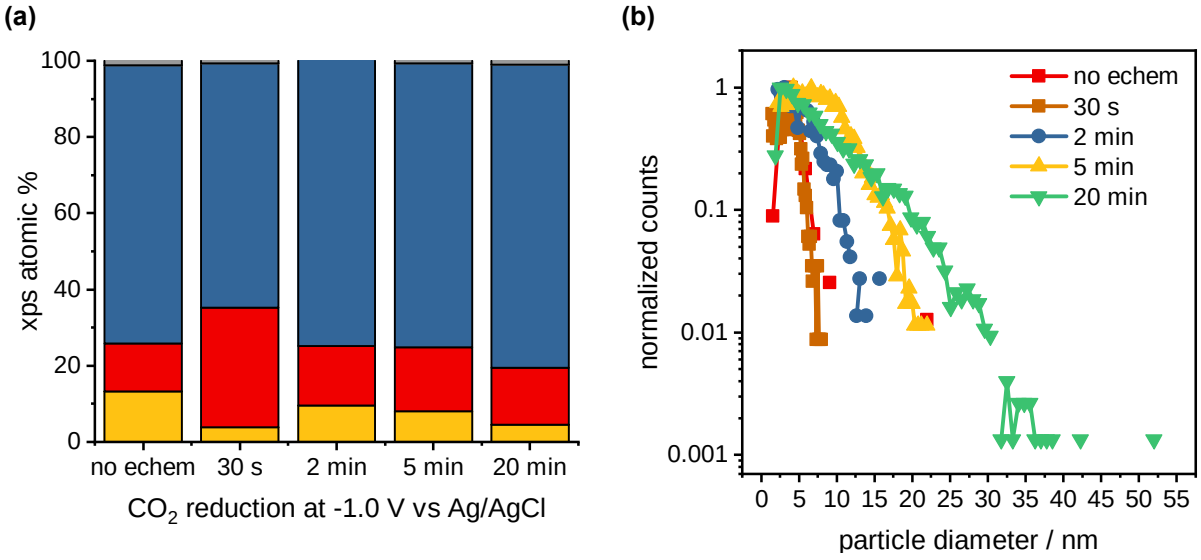

Figure 5.10. Chemical and morphological changes of the sulfur-doped GC sample during the CO_2 reduction reaction at –1.0 V vs Ag/Ag/Cl. **(a)** The XPS elemental composition of ■ sulfur, ■ carbon, ■ oxygen, and ■ gold throughout the reaction reveals a removal of gold and sulfur from the surface. **(b)** SEM surface images of the supported gold nanoparticles showed an aggregation similar to the one that was observed in the untreated sample.

are equally distributed, as can be seen in both the SEM image and the gold mapping. Also, sulfur is detected on the scanned area, which suggests a successful surface treatment. Due to the surface sensitiveness of Auger spectroscopy, gold and sulfur maps are complementary which means that underlying sulfur atoms are not visible where a gold nanoparticle is located. On the right side of the measured area a larger sulfur aggregate is visible, while no gold is found in this region. The sulfur aggregate species was obviously generated during the CO_2 reduction reaction, as the gold nanoparticles deposition was the last step in the sample preparation. This suggests a change of the sulfur species throughout the reaction, which supports the results from the XPS measurements.

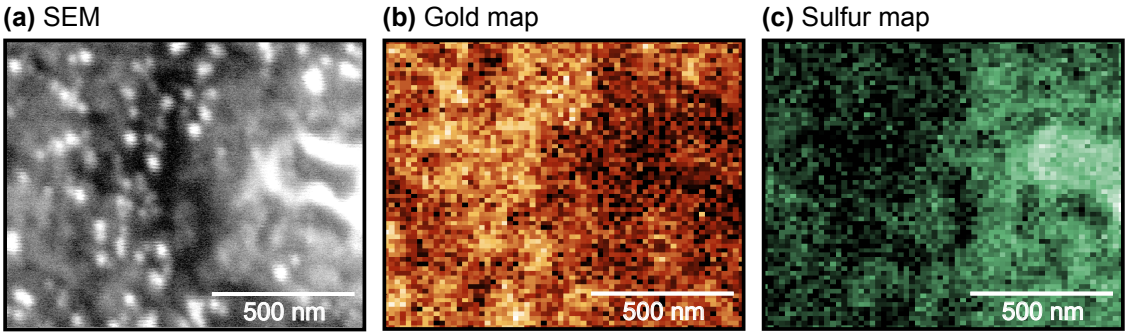

Figure 5.11. The oxygen plasma-treated sample with subsequent H_2S / H_2 annealing revealed a sulfur-containing species on the right side of the image, which was generated during the CO_2 reaction.

6. Conclusion

Supported metal nanoparticles have shown remarkable capabilities for catalysis and represent hence a key opportunity for the transition to a renewable chemical feedstock production. However, a fundamental understanding of supported nanoparticle dynamics, also at the solid-liquid interface, is required for durable catalytic applications. This doctoral work includes the preparation of well-defined particle catalysts, a novel catalyst substrate, and the study of nanoparticle dynamics under reaction conditions.

We developed a novel deposition approach for Pd nanoparticles from aqueous solutions with enhanced size-selectivity. A palladium-containing polyoxometalate (POP) was electrochemically reduced to create size-selected supported nanoparticles on Au(111). The POP substance class spans a variety of transition metals and offers hence the possibility to deposit different catalyst materials. In contrast to previous electrochemical nanoparticle deposition methods, this approach exploits the precise number of metal atoms, present in the POP in an oxidized state. By electrochemical reduction of the metal, the ligands get stripped, and bare metallic clusters are deposited. The Pd-POP reduction occurred at potentials below 0.2 V vs RHE, which implies a significant overpotential of 0.5 V with respect to simple solvated ions. The resulting monolayer Pd clusters were imaged and studied with electrochemical STM. The narrow area distribution of the clusters showed a maximum for apparent diameters of 2 nm. Interestingly, apparent area and height increase, when the electrochemical potential is lowered to the onset of the hydrogen evolution reaction. This behavior was previously observed for larger metallic Pd nanostructures and attributed to hydrogen absorption. Furthermore, the presence of hydrogen intermediates during the deposition process opens up an alternative chemical reduction pathway for the POP precursor. The resulting large, flower-like Pd structures differ significantly from that obtained by electrochemical reduction. A third deposition approach was explored as well, namely the oxidative deposition of the POP, upon which the ligands are stripped off and remain in the solution, while Pd oxide clusters form on the surface. A subsequent reduction with a very low overpotential results in metallic clusters. This study paves the way to investigate metal clusters at the solid-liquid interface on electrochemically addressable supports. Even porous catalyst substrates are suitable that would not be accessible for established vacuum deposition techniques.

A second part of this work concerned the development of novel, flat catalyst supports for their *in situ* investigation under the electrochemical STM. The standard Au(111) support itself, used in the first part of this work, tends to restructure, especially at higher electrochemical potentials, which interferes with detailed studies of cluster dynamics. Semi-conductive carbon nitride films, instead, promise great potential in both the stabilization and the functionalization of metal catalysts and represent hence a focus of current electrocatalytic research. Their structural building blocks determine both, the size of the molecular cavity for cluster stabilization by multiple coordination via nitrogen atoms, and the light absorption properties for photocatalytic applications. We created supported carbon nitride films by the on-surface polymerization of triazido-*s*-heptazine (TAH). This hydrogen-free precursor promises a higher degree of crosslinking than other starting materials, such as melamine. The highly reactive TAH was deposited intact both, from benzene solutions and by evaporation under vacuum. However, the liquid deposition led to aggregate structures during the solvent evaporation process, which reacted similarly as powder samples. During the reaction, the azide group decomposes under nitrogen release and amine nitrogen species are formed. This can be followed both, by XPS and mass spectrometry and has been investigated on highly ordered pyrolytic graphite (HOPG) and Au(111) surfaces, whereby distinct differences were observed. On HOPG, the interaction between TAH and the surface was too weak to prevent desorption before reaching the reaction temperature. On Au(111), instead, the surface binding was significantly stronger and the thermally induced reaction occurred at 405 K, which is 40 K lower than the powder reaction temperature, pointing to a catalytic influence of the support. Similar to HOPG, the volatile nature of TAH led to a multilayer desorption from Au(111), at 310 K before the reaction started. This is advantageous for the growth of just a single layer of the 2D film. STM measurements revealed extended films. The film growth started preferably, but not exclusively, at the Au(111) step edges. Crystalline domains with a lattice constant of 0.78 nm were found in the film, in good agreement with the heptazine dimensions and reference structures. Additionally, second layer features were found in the STM images, with an apparent height compatible with the stacking in crystalline TAH and an expected -stacking. Both, second layer features and first layer island borders indicate that not all heptazine building units are linked perfectly by tertiary amine species. This is supported by the broadened XPS N1s amine signal, which points to the presence of other species, e. g. secondary and primary amines. However, this XPS peak is more narrow for the on-surface synthesis than for the powder sample, which indicates that the surface favors a better crosslinking. Alternatively, the reaction was also photoinduced, by

UV light irradiation at 110 K. Novel upright molecular intermediates were found in the STM. A subsequent heating led to similar films as the heated-only samples. This suggests the formation of a vertical, gold-bound nitrene intermediate. Additional evidence for the strong interaction at the metal-organic interface is the alignment of the Au(111)–($22 \times \sqrt{3}$) herringbone reconstruction with the carbon nitride film – reconstruction lines avoid the islands and do not cross them.

Besides the development of novel catalyst materials, their dynamics were investigated under reaction conditions. The chemical and structural changes of gold nanoparticles supported on pristine, O_2 plasma-treated, and sulfur-doped glassy carbon samples were studied during the CO_2 reduction reaction. Adventitious carbon from atmospheric sample transfer masked the chemical state of carbon support. However, an increase in the oxygen signal by a factor of two and morphological changes indicated a successful oxygen plasma treatment. An annealing procedure under H_2S gas flow enabled the incorporation of sulfur as shown by the presence of a C–S species and sulfate in the XPS spectrum. Both, the oxygen and sulfur treatment were stable throughout the reaction, as only a small signal decrease was observed. The chemical state of the gold nanoparticles did not change during the reaction, but the particles aggregated and thereby built large dendritic structures. This aggregation was strongly dependent on the applied potential and started at a potential of –1.0 V vs Ag/AgCl. The aggregation of gold nanoparticles was reduced significantly by the oxygen plasma-treatment. Here, the majority of particles remained at their initial size. The plasma-treated sample also showed the highest activity. Previous studies attributed this increase in activity by a factor of ten to a better catalyst wetting.[143] However, the almost 80 times higher reduction current observed for the oxidized sample in this thesis suggests that the better particle stabilization helps to preserve the catalytic performance. This again highlights the importance of catalyst-support interaction.

Bibliography

[1] G. Ceballos, P. R. Ehrlich, A. D. Barnosky, A. García, R. M. Pringle, T. M. Palmer, *Science Advances* **2015**, *1*, e1400253 (cit. on p. 7).

[2] J. T. Houghton, G. J. Jenkins, J. J. Ephraums, Climate Change - The IPCC Scientific Assessment, Cambridge University Press, **1990** (cit. on p. 7).

[3] Z. W. Seh, J. Kibsgaard, C. F. Dickens, I. Chorkendorff, J. K. Nø rskov, T. F. Jaramillo, *Science* **2017**, *355*, 146 (cit. on pp. 7, 8, 10).

[4] Electricity Information: Overview, IEA, **2020** (cit. on p. 7).

[5] A. Boulamanti, J. A. Moya, Energy Efficiency and GHG Emissions: Prospective Scenarios for the Chemical and Petrochemical Industry, European Commission, **2017** (cit. on p. 7).

[6] P. D. Luna, C. Hahn, D. Higgins, S. A. Jaffer, T. F. Jaramillo, E. H. Sargent, *Science* **2019**, *364*, DOI 10.1126/science.aav3506 (cit. on p. 7).

[7] J. A. Turner, *Science* **2004**, *305*, 972–974 (cit. on pp. 9, 10).

[8] G. Glenk, S. Reichelstein, *Nature Energy* **2019**, *4*, 216–222 (cit. on p. 9).

[9] M. Carmo, T. Roepke, C. Roth, A. M. dos Santos, J. G. R. Poco, M. Linardi, *Journal of Power Sources* **2009**, *191*, 330–337 (cit. on p. 11).

[10] E. Skúlason, V. Tripkovic, M. r. E. Björketun, S. Gudmundsdóttir, G. Karlberg, J. Rossmeisl, T. Bligaard, H. Jónsson, J. K. Nø rskov, *The Journal of Physical Chemistry C* **2010**, *114*, 18182–18197 (cit. on p. 11).

[11] *Nanocatalysis*, (Eds.: U. Heiz, U. Landman), Springer-Verlag, Berlin Heidelberg, **2007** (cit. on p. 12).

[12] T. Imaoka, H. Kitazawa, W.-J. Chun, S. Omura, K. Albrecht, K. Yamamoto, *Journal of the American Chemical Society* **2013**, *135*, 13089–13095 (cit. on p. 12).

[13] U. Heiz, F. Vanolli, L. Trento, W. Schneider, *Review of Scientific Instruments* **1997**, *68*, 1986–1994 (cit. on p. 12).

[14] C. Yin, E. Tyo, K. Kuchta, B. von Issendorff, S. Vajda, *The Journal of Chemical Physics* **2014**, *140*, 174201 (cit. on p. 12).

[15] J. Nordheim Riedel, M. David Rötzer, M. Jø rgensen, U. Grø nbjerg Vej-Hansen, T. Pedersen, B. Sebok, F. Frank Schweinberger, P. C. Kjæ rgaard Vesborg, O. Hansen, J. Schiø tz, U. Heiz, I. Chorkendorff, *Catalysis Science & Technology* **2016**, *6*, 6893–6900 (cit. on p. 12).

[16] S. Kunz, K. Hartl, M. Nesselberger, F. F. Schweinberger, G. Kwon, M. Hanzlik, K. J. J. Mayrhofer, U. Heiz, M. Arenz, *Physical Chemistry Chemical Physics* **2010**, *12*, 10288–10291 (cit. on p. 12).

[17] P. Losch, W. Huang, E. D. Goodman, C. J. Wrasman, A. Holm, A. R. Riscoe, J. A. Schwalbe, M. Cargnello, *Nano Today* **2019**, *24*, 15–47 (cit. on p. 12).

[18] C.-J. Jia, F. Schüth, *Physical Chemistry Chemical Physics* **2011**, *13*, 2457 (cit. on p. 12).

[19] L. M. Bronstein, Z. B. Shifrina, *Chemical Reviews* **2011**, *111*, 5301–5344 (cit. on p. 12).

[20] R. Young, J. Ward, F. Scire, **1872**, 14 (cit. on p. 12).

[21] G. Binnig, H. Rohrer, C. Gerber, E. Weibel, *Applied Physics Letters* **1982**, *40*, 178–180 (cit. on p. 13).

[22] R. Sonnenfeld, P. K. Hansma, *Science* **1986**, *232*, 211–213 (cit. on p. 13).

[23] J. Schneir, P. K. Hansma, *Langmuir* **1987**, *3*, 1025–1027 (cit. on p. 13).

[24] P. K. Hansma, J. Tersoff, 24 (cit. on p. 13).

[25] R. Sonnenfeld, B. C. Schardt, *Applied Physics Letters* **1986**, *49*, 1172–1174 (cit. on p. 13).

[26] F. A. Möller, J. Kintrup, A. Lachenwitzer, O. M. Magnussen, R. J. Behm, *Physical Review B* **1997**, *56*, 12506–12518 (cit. on p. 13).

[27] M. Baldauf, D. M. Kolb, *Electrochimica Acta* **1993**, *38*, 2145–2153 (cit. on p. 13).

[28] T. Tansel, O. M. Magnussen, *Physical Review Letters* **2006**, *96*, DOI 10.1103/PhysRevLett.96.026101 (cit. on p. 13).

[29] S. Pandelov, U. Stimming, *Electrochimica Acta* **2007**, *52*, 5548–5555 (cit. on pp. 13, 17).

[30] J. H. K. Pfisterer, Y. Liang, O. Schneider, A. S. Bandarenka, *Nature* **2017**, *549*, 74–77 (cit. on p. 13).

[31] R. W. Haid, R. M. Kluge, Y. Liang, A. S. Bandarenka, *Small Methods* **2020**, 2000710 (cit. on p. 13).

[32] C. Dri, M. Panighel, D. Tiemann, L. L. Patera, G. Troiano, Y. Fukamori, F. Knoller, B. A. J. Lechner, G. Cautero, D. Giuressi, G. Comelli, J. Fraxedas, C. Africh, F. Esch, *Ultramicroscopy* **2019**, *205*, 49–56 (cit. on p. 13).

[33] *Handbook of Electrochemistry*, 1st ed, (Ed.: C. G. Zoski), Elsevier, Amsterdam; Boston, **2007**, 892 pp. (cit. on pp. 15–17, 24).

[34] P. R. Unwin in *Encyclopedia of Electrochemistry*, (Ed.: A. J. Bard), Wiley-VCH Verlag GmbH & Co. KGaA, Weinheim, Germany, **2007** (cit. on p. 15).

[35] M. Dunwell, Q. Lu, J. M. Heyes, J. Rosen, J. G. Chen, Y. Yan, F. Jiao, B. Xu, *Journal of the American Chemical Society* **2017**, *139*, 3774–3783 (cit. on p. 16).

[36] N. Elgrishi, K. J. Rountree, B. D. McCarthy, E. S. Rountree, T. T. Eisenhart, J. L. Dempsey, *Journal of Chemical Education* **2018**, *95*, 197–206 (cit. on p. 17).

[37] A. J. Bard, L. R. Faulkner, *Electrochemical Methods: Fundamentals and Applications*, 2nd ed, Wiley, New York, **2001**, 833 pp. (cit. on p. 17).

[38] J. Friedl, R. Al-Oweini, M. Herpich, B. Keita, U. Kortz, U. Stimming, *Electrochimica Acta* **2014**, *141*, 357–366 (cit. on p. 17).

[39] A. V. Rudnev, M. R. Ehrenburg, E. B. Molodkina, A. Abdelrahman, M. Arenz, P. Broekmann, T. Jacob, *ChemElectroChem* **2020**, *7*, 501–508 (cit. on p. 18).

[40] K. Funke, Impedanzspektroskopie, **2002** (cit. on p. 18).

[41] D. Ende, K.-M. Mangold, *Chemie in unserer Zeit* **1993**, *27*, 134–140 (cit. on p. 19).

[42] G. K. H. Wiberg, Technische Universität München, München, **2010** (cit. on p. 21).

[43] M. Rost in *Reference Module in Chemistry, Molecular Sciences and Chemical Engineering*, Elsevier, **2017** (cit. on p. 22).

[44] N. J Tao, C. Z Li, H. X He, *Journal of Electroanalytical Chemistry* **2000**, *492*, 81–93 (cit. on p. 23).

[45] B. Voigtländer, *Scanning Probe Microscopy*, Springer Berlin Heidelberg, New York, NY, **2015** (cit. on p. 23).

[46] J. Ahn, M. Pyo, *Bull. Korean Chem. Soc.* **2000**, *21*, 644 (cit. on p. 24).

[47] J. Pan, T. W. Jing, S. M. Lindsay, *The Journal of Physical Chemistry* **1994**, *98*, 4205–4208 (cit. on p. 24).

[48] D.-H. Woo, E.-M. Choi, Y.-H. Yoon, K.-J. Kim, I. Jeon, H. Kang, *Surface Science* **2007**, *601*, 1554–1559 (cit. on pp. 24–26).

[49] *Scanning Tunneling Microscopy II: Further Applications and Related Scanning Techniques*, 2nd ed, (Eds.: R. Wiesendanger, H.-J. Güntherodt, W. Baumeister), Springer, Berlin ; New York, **1995**, 349 pp. (cit. on p. 24).

[50] A. Vaught, T. Jing, S. Lindsay, *Chemical Physics Letters* **1995**, *236*, 306–310 (cit. on p. 24).

[51] M. Hugelmann, W. Schindler, *Surface Science* **2003**, *541*, L643–L648 (cit. on pp. 25, 26).

[52] M. F. Toney, J. N. Howard, J. Richer, G. L. Borges, J. G. Gordon, O. R. Melroy, D. G. Wiesler, D. Yee, L. B. Sorensen, *Nature* **1994**, *368*, 444–446 (cit. on p. 25).

[53] M. Galperin, A. Nitzan, I. Benjamin, *The Journal of Physical Chemistry A* **2002**, *106*, 10790–10796 (cit. on p. 25).

[54] W. Schmickler, *Surface Science*, Proceedings of the IUVSTA Workshop on Surface Science and Electrochemistry **1995**, *335*, 416–421 (cit. on p. 26).

[55] F. C. Simeone, D. M. Kolb, S. Venkatachalam, T. Jacob, *Surface Science* **2008**, *602*, 1401–1407 (cit. on p. 26).

[56] W. Schmickler, C. Widrig, **1992**, 9 (cit. on p. 26).

[57] A. M. Kuznetsov, J. Ulstrup, *The Journal of Physical Chemistry A* **2000**, *104*, 11531–11540 (cit. on p. 26).

[58] A. M. Kuznetsov, I. G. Medvedev, J. Ulstrup, *The Journal of Chemical Physics* **2007**, *127*, 104708 (cit. on p. 26).

[59] I. V. Pobelov, Z. Li, T. Wandlowski, *Journal of the American Chemical Society* **2008**, *130*, 16045–16054 (cit. on pp. 26, 27).

[60] M. Wilms, M. Kruft, G. Bermes, K. Wandelt, *Review of Scientific Instruments* **1999**, *70*, 3641–3650 (cit. on pp. 28, 29, 34, 36).

[61] M. Wilms, M. Schmidt, G. Bermes, K. Wandelt, *Review of Scientific Instruments* **1998**, *69*, 2696–2703 (cit. on pp. 30, 124).

[62] S. Wieghold, TU Munich, Munich, **2016** (cit. on pp. 29, 124).

[63] C. J. Chen, *Introduction to Scanning Tunneling Microscopy* **2008**, 26 (cit. on p. 30).

[64] U Straumann, Elektronik Für Physiker - Physik Institut Universität Zürich, **2005** (cit. on p. 32).

[65] C. Schmid, J. Plansky, A. Rössler, F. Esch, N. Bock, *Labview - Drift Correction*, Munich: TU Munich, **2019** (cit. on p. 33).

[66] D. Rugar, P. Hansma, *Physics today* **1990**, *43*, 23–30 (cit. on p. 34).

[67] D. McMullan, *Scanning* **1995**, *17*, 175–185 (cit. on p. 34).

[68] J. M. Hollander, W. L. Jolly, *Accounts of chemical research* **1970**, *3*, 193–200 (cit. on p. 35).

[69] P. Daimel, F. Allegretti, Elemental and Chemical Analysis with X-Ray Photoelectron Spectroscopy, **2020** (cit. on p. 35).

[70] L. A. Kibler, **2003**, 56 (cit. on p. 38).

[71] D. M. Kolb, J. Schneider, *Electrochimica Acta* **1986**, *31*, 929–936 (cit. on p. 38).

[72] S. F. L. Mertens, Tip Etching Parameters for Pt/Ir Tips in KOH/KSCN Solutions, **2017** (cit. on p. 40).

[73] N. Bock, A. De Clercq, L. Seidl, T. Kratky, T. Ma, S. Günther, U. Kortz, U. Heiz, F. Esch, *ChemElectroChem* **2021**, *8*, 1280–1288 (cit. on p. 43).

[74] J. Liebig, *Annalen der Pharmacie* **1834**, *10*, 1–47 (cit. on p. 59).

[75] P. Kumar, E. Vahidzadeh, U. K. Thakur, P. Kar, K. M. Alam, A. Goswami, N. Mahdi, K. Cui, G. M. Bernard, V. K. Michaelis, K. Shankar, *Journal of the American Chemical Society* **2019**, *141*, 5415–5436 (cit. on p. 59).

[76] X. Wang, S. Blechert, M. Antonietti, *ACS Catalysis* **2012**, *2*, 1596–1606 (cit. on p. 59).

[77] Z. Chen, E. Vorobyeva, S. Mitchell, E. Fako, M. A. Ortuño, N. López, S. M. Collins, P. A. Midgley, S. Richard, G. Vilé, J. Pérez-Ramírez, *Nature Nanotechnology* **2018**, *13*, 702–707 (cit. on p. 59).

[78] S. M. Hosseini, M. Ghiaci, H. Farrokhpour, *Materials Research Express* **2019**, *6*, DOI 10.1088/2053-1591/ab3cbd (cit. on p. 59).

[79] A. S. Crampton, M. D. Rötzer, U. Landman, U. Heiz, *ACS Catalysis* **2017**, 6738–6744 (cit. on p. 59).

[80] Y. Fukamori, M. König, B. Yoon, B. Wang, F. Esch, U. Heiz, U. Landman, *ChemCatChem* **2013**, *5*, 3330–3341 (cit. on p. 59).

[81] K. P. Burdina, N. B. Zorov, O. V. Kravchenko, Y. Y. Kuzyakov, J. I. Kim, S. A. Kulinich, *Mendeleev Communications* **2000**, *10*, 207–208 (cit. on pp. 60, 79).

[82] J. Kouvetakis, M. Todd, B. Wilkens, A. Bandari, N. Cave, *Chemistry of Materials* **1994**, *6*, 811–814 (cit. on p. 60).

[83] C. Li, C.-B. Cao, H.-S. Zhu, *Materials Letters* **2004**, 4 (cit. on p. 60).

[84] M. Sima, E. Vasile, A. Sima, N. Preda, C. Logofatu, *International Journal of Hydrogen Energy* **2019**, *44*, 24430–24440 (cit. on p. 60).

[85] G. Algara-Siller, N. Severin, S. Y. Chong, T. Björkman, R. G. Palgrave, A. Laybourn, M. Antonietti, Y. Z. Khimyak, A. V. Krasheninnikov, J. P. Rabe, U. Kaiser, A. I. Cooper, A. Thomas, M. J. Bojdys, *Angewandte Chemie* **2014**, *126*, 7580–7585 (cit. on p. 60).

[86] M. J. Bojdys, N. Severin, J. P. Rabe, A. I. Cooper, A. Thomas, M. Antonietti, *Macromolecular Rapid Communications* **2013**, *34*, 850–854 (cit. on p. 60).

[87] J. Jiang, L. Ou-yang, L. Zhu, A. Zheng, J. Zou, X. Yi, H. Tang, *Carbon* **2014**, *80*, 213–221 (cit. on pp. 60, 88, 89).

[88] Q. Fan, L. Yan, M. W. Tripp, O. Krejci, S. Dimosthenous, S. R. Kachel, M. Chen, A. S. Foster, U. Koert, P. Liljeroth, M. Gottfried, **2020**, DOI 10.26434/chemrxiv.13423997.v1 (cit. on p. 60).

[89] Y.-W. Luo, C.-H. Chou, P.-C. Lin, C.-M. Chiang, *The Journal of Physical Chemistry C* **2019**, *123*, 12195–12202 (cit. on pp. 60, 87, 89).

[90] E. G. Gillan, *Chemistry of Materials* **2000**, *12*, 3906–3912 (cit. on pp. 60, 85).

[91] M. Krinninger, Master Thesis: On-Surface Carbon Nitride Film Polymerization after Liquid and Vapor Precursor Deposition, **2020** (cit. on p. 60).

[92] D. R. Miller, D. C. Swenson, E. G. Gillan, *Journal of the American Chemical Society* **2004**, *126*, 5372–5373 (cit. on pp. 60, 61, 64).

[93] D. R. Miller, J. R. Holst, E. G. Gillan, *Inorganic Chemistry* **2007**, *46*, 2767–2774 (cit. on pp. 60, 61, 63, 75).

[94] W. Zheng, N.-B. Wong, W. Wang, G. Zhou, A. Tian, *The Journal of Physical Chemistry A* **2004**, *108*, 97–106 (cit. on pp. 60, 65, 66, 68, 75, 87).

[95] G. L'abbe, *Chemical Reviews* **1969**, *69*, 345–363 (cit. on pp. 60, 73).

[96] G. Sauerbrey, *Zeitschrift für Physik* **1959**, *155*, 206–222 (cit. on p. 65).

[97] J. Yang, G. Wang, X. Gong, J. Zhang, *Journal of Materials Science* **2018**, *53*, 15977–15985 (cit. on p. 65).

[98] D. R. Miller, D. C. Swenson, E. G. Gillan, *Journal of the American Chemical Society* **2004**, *126*, 5372–5373 (cit. on p. 66).

[99] R. B. Mallion, D. H. Rouvray, *Journal of Mathematical Chemistry* **1990**, *5*, 1–21 (cit. on p. 66).

[100] B. P. Klein, J. M. Morbec, M. Franke, K. K. Greulich, M. Sachs, S. Parhizkar, F. C. Bocquet, M. Schmid, S. J. Hall, R. J. Maurer, B. Meyer, R. Tonner, C. Kumpf, P. Kratzer, J. M. Gottfried, *The Journal of Physical Chemistry C* **2019**, *123*, 29219–29230 (cit. on p. 67).

[101] B. P. Klein, N. J. van der Heijden, S. R. Kachel, M. Franke, C. K. Krug, K. K. Greulich, L. Ruppenthal, P. Müller, P. Rosenow, S. Parhizkar, F. C. Bocquet, M. Schmid, W. Hieringer, R. J. Maurer, R. Tonner, C. Kumpf, I. Swart, J. M. Gottfried, *Physical Review X* **2019**, *9*, 011030 (cit. on p. 67).

[102] A. Singhal, *J Mol Model* **2018**, 9 (cit. on pp. 67, 82).

[103] M. J. Calaway, M. D. Fries, *46th Lunar Planet. Sci. Conf.* **2015**, 5–6 (cit. on pp. 67, 68, 99).

[104] *Handbook of X-Ray Photoelectron Spectroscopy: A Reference Book of Standard Spectra for Identification and Interpretation of XPS Data*, (Eds.: J. F. Moulder, W. F. Stickle, P. E. Sobol, K. D. Bomben, J. Chastain, R. C. King Jr., I. Physical Electronics), Physical Electronics, Eden Prairie, Minn., **1995**, 261 pp. (cit. on pp. 67, 73, 98).

[105] K. Chen, Z. Chai, C. Li, L. Shi, M. Liu, Q. Xie, Y. Zhang, D. Xu, A. Manivannan, Z. Liu, *ACS Nano* **2016**, *10*, 3665–3673 (cit. on pp. 68, 74).

[106] J. Safaei, N. A. Mohamed, M. F. M. Noh, M. F. Soh, M. A. Riza, N. S. M. Mustakim, N. A. Ludin, M. A. Ibrahim, W. N. R. W. Isahak, M. A. M. Teridi, *Journal of Alloys and Compounds* **2018**, *769*, 130–135 (cit. on pp. 68, 74).

[107] A. C. Gouget-Laemmel, J. Yang, M. A. Lodhi, A. Siriwardena, D. Aureau, R. Boukherroub, J.-N. Chazalviel, F. Ozanam, S. Szunerits, *The Journal of Physical Chemistry C* **2013**, *117*, 368–375 (cit. on p. 68).

[108] J. J. Yeh, I. Lindau, *Atomic data and nuclear data tables* **1985**, 1–155 (cit. on p. 69).

[109] R. D. Deegan, O. Bakajin, T. F. Dupont, G. Huber, S. R. Nagel, T. A. Witten, *Nature* **1997**, *389*, 827–829 (cit. on p. 70).

[110] S. Rauschenbach, F. L. Stadler, E. Lunedei, N. Malinowski, S. Koltsov, G. Costantini, K. Kern, *Small* **2006**, *2*, 540–547 (cit. on p. 70).

[111] I Kusunoki, M Sakai, Y Igari, S Ishidzuka, T Takami, T Takaoka, M Nishitani-Gamo, T Ando, *Surface Science* **2001**, *492*, 315–328 (cit. on p. 73).

[112] P. S. Bagus, E. S. Ilton, C. J. Nelin, *Surface Science Reports* **2013**, *68*, 273–304 (cit. on p. 73).

[113] Y. Bai, Friedrich-Alexander-Universität Erlangen-Nürnberg, Erlangen, **2010** (cit. on p. 73).

[114] J. Wang, E. G. Gillan, *Thin Solid Films* **2002**, 7 (cit. on pp. 75, 84).

[115] T. Saplinova, V. Bakumov, T. Gmeiner, J. Wagler, M. Schwarz, E. Kroke, *Zeitschrift für anorganische und allgemeine Chemie* **2009**, NA–NA (cit. on p. 75).

[116] J. Tong, L. Zhang, F. Li, K. Wang, L. Han, S. Cao, *RSC Advances* **2015**, *5*, 88149–88153 (cit. on p. 75).

[117] S. Bonanni, K. Aït-Mansour, M. Hugentobler, H. Brune, W. Harbich, *The European Physical Journal D* **2011**, *63*, 241–249 (cit. on p. 77).

[118] A. Hirsch, B. Nuber, *Accounts of Chemical Research* **1999**, *32*, 795–804 (cit. on pp. 77, 78).

[119] X. Zhang, X. Xie, H. Wang, J. Zhang, B. Pan, Y. Xie, *Journal of the American Chemical Society* **2013**, *135*, 18–21 (cit. on p. 79).

[120] T. Tyborski, C. Merschjann, S. Orthmann, F. Yang, M.-C. Lux-Steiner, T. Schedel-Niedrig, *Journal of Physics: Condensed Matter* **2013**, *25*, 395402 (cit. on pp. 82, 85).

[121] M. J. Bojdys, J.-O. Müller, M. Antonietti, A. Thomas, *Chemistry – A European Journal* **2008**, *14*, 8177–8182 (cit. on p. 85).

[122] J. Tian, H. Cao, W. Wu, Q. Yu, N. P. Guisinger, Y. P. Chen, *Nano Letters* **2012**, *12*, 3893–3899 (cit. on p. 87).

[123] E. Leyva, M. S. Platz, G. Persy, J. Wirz, *Journal of the American Chemical Society* **1986**, *108*, 3783–3790 (cit. on p. 87).

[124] G. B. Schuster, M. S. Platz in *Advances in Photochemistry*, (Eds.: D. H. Volman, G. S. Hammond, D. C. Neckers), John Wiley & Sons, Inc., Hoboken, NJ, USA, **2007**, pp. 69–143 (cit. on p. 87).

[125] H. Yamada, H. Shizuka, K. Matsui, *The Journal of Organic Chemistry* **1975**, *40*, 1351–1353 (cit. on p. 87).

[126] P. J. Altmann, A. Pöthig, *Journal of the American Chemical Society* **2016**, *138*, 13171–13174 (cit. on pp. 91, 92).

[127] P. J. Altmann, C. Jandl, A. Pöthig, *Dalton Transactions* **2015**, *44*, 11278–11281 (cit. on p. 91).

[128] K. Yang, Y. Pei, J. Wen, Z. Pei, *Chemical Communications* **2016**, *52*, 9316–9326 (cit. on p. 92).

[129] B. Chatelet, L. Joucla, J.-P. Dutasta, A. Martinez, V. Dufaud, *Chemistry - A European Journal* **2014**, *20*, 8571–8574 (cit. on p. 92).

[130] L. Wang, L. Wang, J. Zhang, X. Liu, H. Wang, W. Zhang, Q. Yang, J. Ma, X. Dong, S. J. Yoo, J.-G. Kim, X. Meng, F.-S. Xiao, *Angewandte Chemie International Edition* **2018**, *57*, 6104–6108 (cit. on p. 93).

[131] S. Nitopi, E. Bertheussen, S. B. Scott, X. Liu, A. K. Engstfeld, S. Horch, B. Seger, I. E. L. Stephens, K. Chan, C. Hahn, J. K. Nø rskov, T. F. Jaramillo, I. Chorkendorff, *Chemical Reviews* **2019**, *119*, 7610–7672 (cit. on p. 93).

[132] J. Wang, G. Yin, Y. Shao, S. Zhang, Z. Wang, Y. Gao, *Journal of Power Sources* **2007**, *171*, 331–339 (cit. on p. 94).

[133] M. Carmo, A. R. dos Santos, J. G. R. Poco, M. Linardi, *Journal of Power Sources*, X Polish Conference on Systems with Fast Ionic Transport **2007**, *173*, 860–866 (cit. on p. 94).

[134] P. J. F. Harris †, *Philosophical Magazine* **2004**, *84*, 3159–3167 (cit. on p. 94).

[135] D. Nečas, P. Klapetek, *Central European Journal of Physics* **2012**, *10*, 181–188 (cit. on pp. 94, 128).

[136] D. K. Pattadar, F. P. Zamborini, **2019**, 11 (cit. on p. 94).

[137] K. Manthiram, Y. Surendranath, A. P. Alivisatos, *Journal of the American Chemical Society* **2014**, *136*, 7237–7240 (cit. on pp. 95, 96).

[138] J. E. Aviles Acosta, Unpublished results within PhD thesis, Stanford University, Palo Alto, **2020** (cit. on pp. 97, 103, 128).

[139] S. R. Kelemen, H. Freund, *Energy & Fuels* **1988**, *2*, 111–118 (cit. on p. 99).

[140] Y. Yi, G. Weinberg, M. Prenzel, M. Greiner, S. Heumann, S. Becker, R. Schlögl, *Catalysis Today* **2017**, *295*, 32–40 (cit. on pp. 99, 102).

[141] Y. Kudo, N. Yoshida, M. Fujimoto, K. Tanaka, I. Toyoshima, *Bulletin of the Chemical Society of Japan* **1986**, *59*, 1481–1486 (cit. on p. 99).

[142] F. J. López-Garzón, M. Domingo-García, M. Pérez-Mendoza, P. M. Alvarez, V. Gómez-Serrano, *Langmuir* **2003**, *19*, 2838–2844 (cit. on p. 102).

[143] J. Sanchez, T. R. Hellstern, L. A. King, T. F. Jaramillo, *Advanced Energy Materials* **2019**, *9*, 1901824 (cit. on pp. 102, 104, 111).

[144] Highly Oriented Pyrolytic Graphite (HOPG) - TipsNano, `https://tipsnano.com/catalog/hopg/` (visited on 01/18/2021) (cit. on p. 102).

[145] A. Tracz, G. Wegner, J. P. Rabe, *Langmuir* **1993**, *9*, 3033–3038 (cit. on p. 102).

[146] J. W Niemantsverdriet, *Spectroscopy in Catalysis: An Introduction*, **2010** (cit. on p. 104).

[147] A. I. Frenkel, S. Nemzer, I. Pister, L. Soussan, T. Harris, Y. Sun, M. H. Rafailovich, *The Journal of Chemical Physics* **2005**, *123*, 184701 (cit. on p. 105).

[148] B. Quan, S.-H. Yu, D. Y. Chung, A. Jin, J. H. Park, Y.-E. Sung, Y. Piao, *Scientific Reports* **2015**, *4*, 5639 (cit. on pp. 105, 106).

[149] Z. Yang, Z. Yao, G. Li, G. Fang, H. Nie, Z. Liu, X. Zhou, X. Chen, S. Huang, *ACS Nano* **2012**, *6*, 205–211 (cit. on pp. 105, 106).

[150] H. L. Poh, P. Šimek, Z. Sofer, M. Pumera, *ACS Nano* **2013**, *7*, 5262–5272 (cit. on pp. 105, 106).

[151] M. Collaud Coen, B. Keller, P. Groening, L. Schlapbach, *Journal of Applied Physics* **2002**, *92*, 5077–5083 (cit. on p. 105).

[152] C. Powell, X-Ray Photoelectron Spectroscopy Database XPS,Version 4.1, NIST Standard Reference Database 20, **1989** (cit. on p. 106).

Acknowledgments

First, I want to thank Friedrich Esch for supervising my PhD study and his excellent guidance at all times. His inspiring scientific curiosity and neverending enthusiasm for our projects are really impressive, as is his passion for teaching.

I want to thank Ueli Heiz for allowing me to pursue my PhD at his chair. He shows great kindness in leading the group and creates an environment in which everyone is able to develop their scientific capabilities.

I am very indebted to Astrid de Clercq for introducing me to the ECSTM setup and her immense contribution to this work. It was a great pleasure to work with her and I really enjoyed our discussions.

Additionally, many thanks to all coworkers, students, and workshop staff, who contributed to this work. I want to highlight Barbara Lechner for the introduction to the UHV-STM and Max Wiedemann for his outstanding electrotechnical skills. Their willingness to share their tricks helped me throughout this thesis.

I am very grateful to Christopher Hahn, Jaime Aviles Acosta, and Thomas Jaramillo from the University of Stanford for hosting me as a visiting researcher at their labs. They have taught me a great deal, especially regarding the applicability of catalysts.

I acknowledge the financial support by Deutsche Forschungsgemeinschaft (DFG) through the International Graduate School for Science and Engineering (IGSSE). I enjoyed the scientific collaboration within our IGSSE team with Carla Courtois, Johannes Küchle, Felix Haag, and Francesco Allegretti.

Finally, I thank the whole Heiz group with former and current members for creating a constantly enjoyable work environment.

A. Appendix

A.1. RDE Positioning System

The RDE is mounted on a linear positioning system, which can be moved with a step motor. For the control a Step Rocker *TMCM–1110* is used. The microcontroller is programmed to wait for an external TTL pulse to perform a step. Depending on the polarity and frequency the movement in a certain direction is performed. Figure A.1a shows the control unit consisting of the *TMCM-1110* board (right side) an additional frequency generator (left side). The *TCL555* LinCMOS timer is used to generate a certain frequency. Figure A.1b shows the circuit diagram of the *TCL555* board. It can be activated with an external push button and the polarity of the output signal can be inverted by the flip switch. The potentiometer is only internally accessible and allows a frequency change (current resistance 96 kOhm). Due to the current limitation of the *TCL555* board, the frequency and therefore the maximal velocity is also limited.

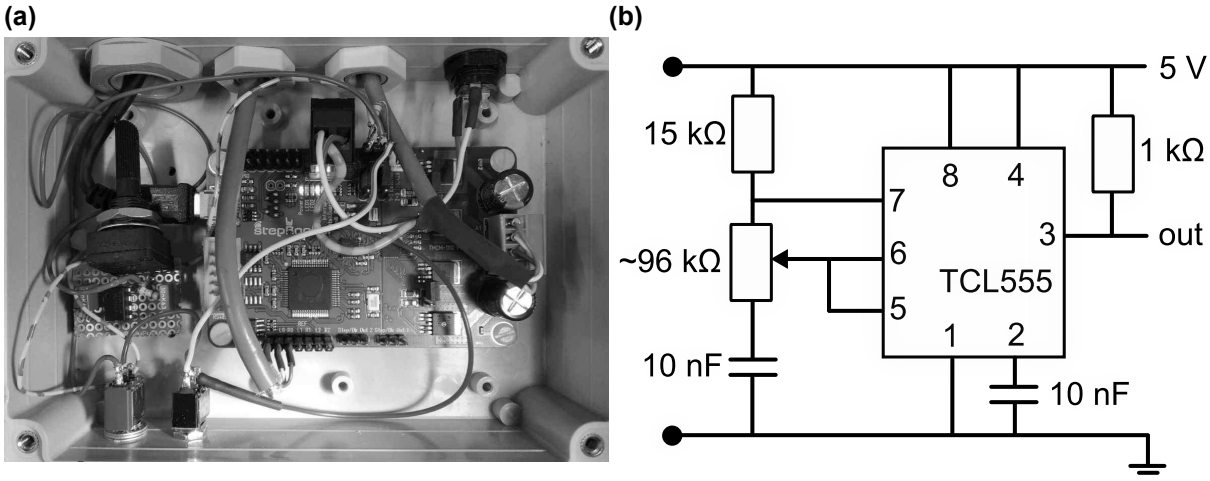

Figure A.1. **(a)** Image of the control unit to drive the linear positioning system. The right board is the Step Rocker *TMCM–1110*. The left board is equipped with a *TCL555* frequency generator which controls both the velocity and direction of the movement. The output of the *TCL555* is directed to the *TMCM–1110* board. **(b)** The circuit diagram of the *TCL555* board with adjustable potentiometer.

A.2. ECSTM Parameters

A.2.1. Piezo Calibration

The scanner piezo calibration is crucial for a reliable imaging. The parameters in Table A.1 are used in this work and were controlled by the analysis of the atomic lattice of HOPG and the step height of an Au(111) terrace.

Table A.1. ECSTM scanner piezo calibration values, which can be set in the *SPM100* software.

piezo segment	calibration factor
X motion	12.86 $\frac{nm}{V}$
Y motion	12.86 $\frac{nm}{V}$
Z motion	1.0 $\frac{nm}{V}$
X offset	12.86 $\frac{nm}{V}$
Y offset	12.86 $\frac{nm}{V}$
Z offset	2.0 $\frac{nm}{V}$

A.2.2. Tunneling Tip Movements with Beetle Type STM

In order to establish a tunneling junction between the STM tip and the conductive surface, the STM described in this work is using the beetle approach. The measurement computer creates a sawtooth wave on the PCI-DAC board, which is amplified by the *SPM100* and then applied to the base piezos. In the Table A.2 the parameters used in this work are listed. The *SPM100 XY Scan Driver*, *XY Offset Driver*, and *Z Driver Board* are responsible for the saw-tooth voltage profile generation. The maximal possible voltage range for all X and Y outputs is -215 V to 215 V. The tip movement has been optimized by Wieghold [62]. Figure A.2 shows the voltage profile for the Pin A and B, which are the opposing -X and +X piezo segments at the centered base piezo further described by Wilms et al. [61].

Table A.2. Approach Parameter of the ECSTM.

Approach type	Kinetic Waveform	Approach amplitude	1.54 nm
Approach mode	Tip retract	Retract amplitude	1.54 nm
Approach threshold	-50	Fast approach	2.0 nm
Feedback delay	2.0 s	Fast retract	2.0 nm
Signal threshold	0.8 nA	Period	50 ms
Test delay	11 ms	Filter period	0 s
Adjust steps	1	Asymmetry	0 %
Retract steps	20	Adjust amplitude	1.54 nm
Approach steps	1	Motion per D/A Volt	-100 pm
Polarity	Bipolar allowed	Cycle delay	20 ms
Output channel	DAC 1A		

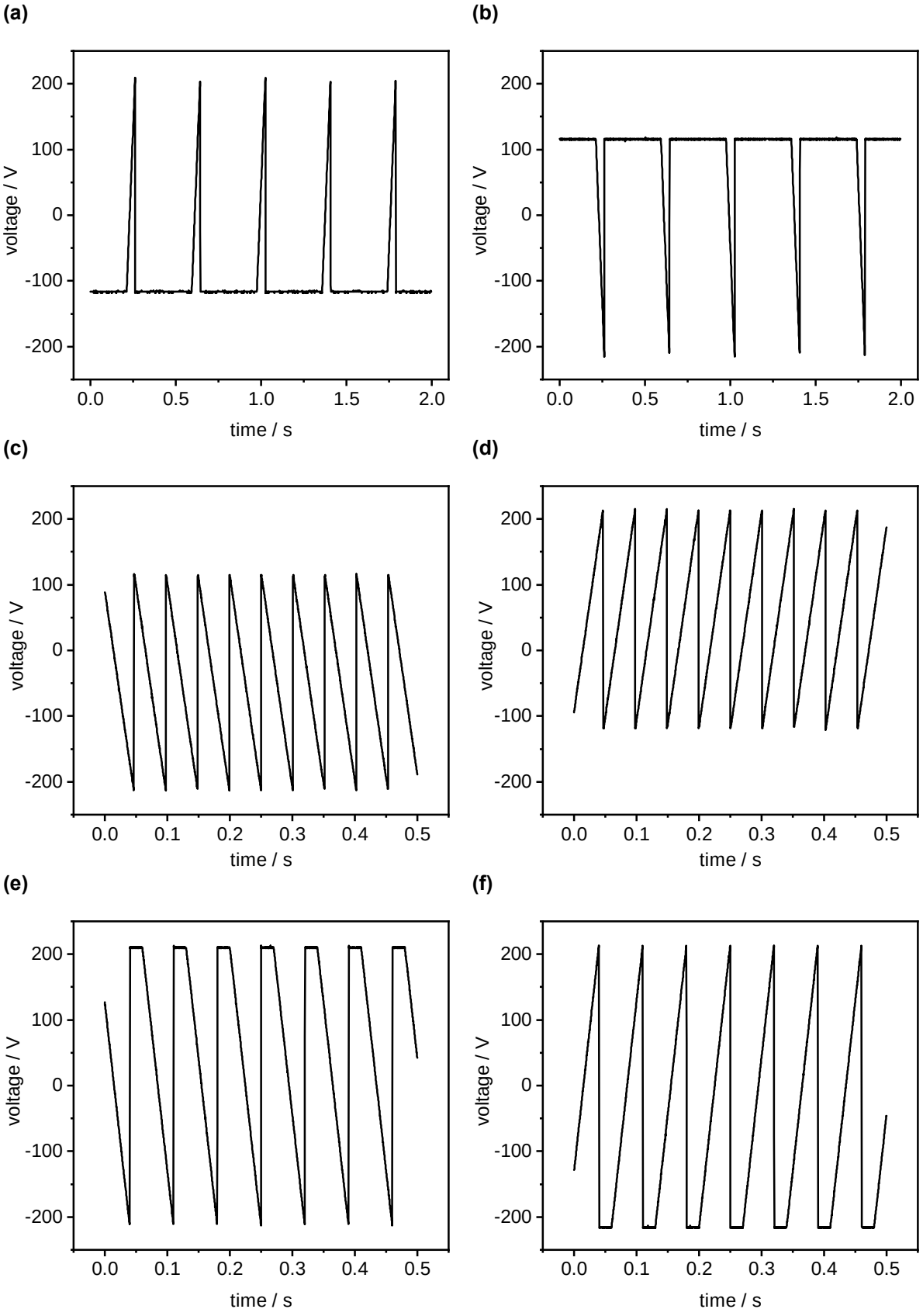

Figure A.2. Output voltage -X and +X signals of the centered base piezo for tip movement: **(a)** approach pin A, **(b)** approach pin B, **(c)** retract pin A, **(d)** retract pin B, **(e)** fast-out pin A, **(f)** fast-out pin B.

A.3. Implementation of Drift Correction

For the implementation of the drift correction, we made several adjustments to the existing electronics. Figure A.3a – b show the modified *SPM100 Log Board* with the added board for the signal addition to the y-axis. The board was manufactured by the electronic workshop of the Chemistry Faculty, TUM. Figure A.3c shows the circuit diagram of the added board.

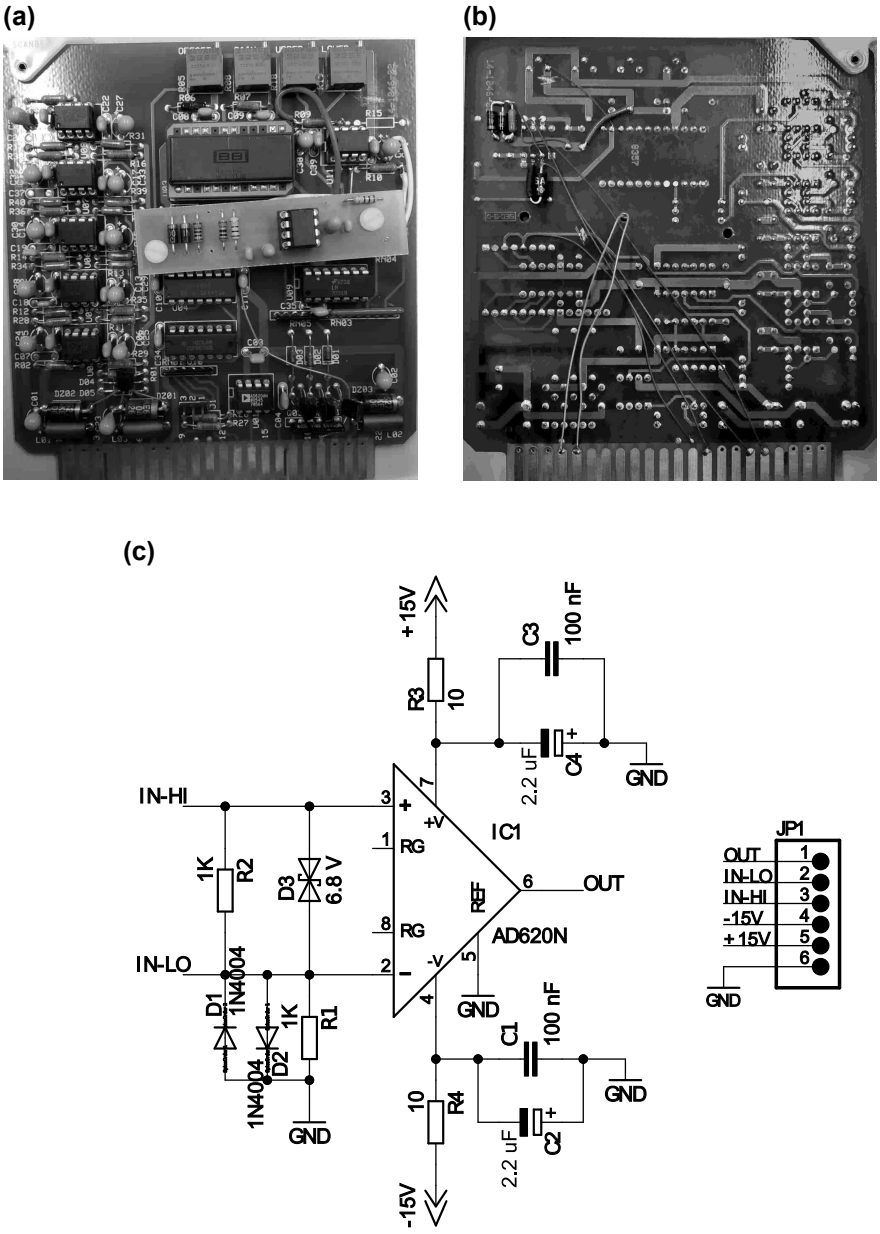

Figure A.3. Implementation of drift correction: **(a – b)** Modified log board of the *SPM100* electronics and **(c)** circuit diagram of the additional board, which can be seen on Figure **(a)**.

A.4. Particle Detection

The grain detection routine of the Gwyddion software, deveolped by Nečas and Klapetek [135] was used. The obtained particle selection is exemplary shown in Figure A.4.

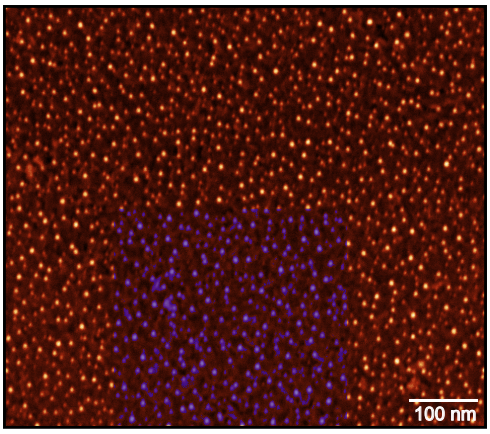

Figure A.4. **(a)** SEM image of Au nanoparticles on glassy carbon after deposition. In blue the selected particle are marked, which indicate the particle detection routine. Data provided by Aviles Acosta [138].